Site U1422[1]

R. Tada, R.W. Murray, C.A. Alvarez Zarikian, W.T. Anderson Jr., M.-A. Bassetti, B.J. Brace, S.C. Clemens, M.H. da Costa Gurgel, G.R. Dickens, A.G. Dunlea, S.J. Gallagher, L. Giosan, A.C.G. Henderson, A.E. Holbourn, K. Ikehara, T. Irino, T. Itaki, A. Karasuda, C.W. Kinsley, Y. Kubota, G.S. Lee, K.E. Lee, J. Lofi, C.I.C.D. Lopes, L.C. Peterson, M. Saavedra-Pellitero, T. Sagawa, R.K. Singh, S. Sugisaki, S. Toucanne, S. Wan, C. Xuan, H. Zheng, and M. Ziegler[2]

Chapter contents

[1]Tada, R., Murray, R.W., Alvarez Zarikian, C.A., Anderson, W.T., Jr., Bassetti, M.-A., Brace, B.J., Clemens, S.C., da Costa Gurgel, M.H., Dickens, G.R., Dunlea, A.G., Gallagher, S.J., Giosan, L., Henderson, A.C.G., Holbourn, A.E., Ikehara, K., Irino, T., Itaki, T., Karasuda, A., Kinsley, C.W., Kubota, Y., Lee, G.S., Lee, K.E., Lofi, J., Lopes, C.I.C.D., Peterson, L.C., Saavedra-Pellitero, M., Sagawa, T., Singh, R.K., Sugisaki, S., Toucanne, S., Wan, S., Xuan, C., Zheng, H., and Ziegler, M., 2015. Site U1422. *In* Tada, R., Murray, R.W., Alvarez Zarikian, C.A., and the Expedition 346 Scientists, *Proc. IODP,* 346: College Station, TX (Integrated Ocean Drilling Program). doi:10.2204/iodp.proc.346.103.2015
[2]**Expedition 346 Scientists' addresses.**

Background and objectives

Integrated Ocean Drilling Program (IODP) Site U1422 is located in the northeastern part of the marginal sea between the Eurasian continent and the Japanese Islands at 43°45.99′N, 138°49.99′E and 3429 meters below sea level. The site is ~40 km southwest of Ocean Drilling Program (ODP) Leg 127 Site 795 and near the northeastern edge of the topographic depression of the Japan Basin (Fig. **F1**). The site is mainly under the influence of the Liman (Cold) Current but may also be slightly influenced by the Tsushima Warm Current (TWC) (Yoon and Kim, 2009). Although more than one-half (1.4 Sv) of the TWC (~2.5 Sv) flows out of the marginal sea through the Tsugaru Strait, ~300 km south of Site U1422, the rest of the TWC (~1.1 Sv) flows further north and out through the Soya Strait at present (e.g., Talley et al., 2006). Because the sill depth of the Soya Strait (~300 km northeast of Site U1422) is only 55 m, the influence of the TWC should have been significantly affected by glacioeustatic sea level changes during the Quaternary. Results from previous drilling at Site 795 suggest continuous deposition of hemipelagic sediment since the middle Miocene, at an average linear sedimentation rate of ~55 m/m.y. for the upper 200 m (Tada, 1994). This sedimentation rate is slow enough to detect the contribution of eolian dust from the Asian continent. The Pliocene–Pleistocene sediment of Site 795 also contains occasional dropstones in the upper 300 m of the sequence, suggesting its appropriateness for ice-rafted debris (IRD) study.

Site U1422 is the northernmost site of the latitudinal transect targeted by IODP Expedition 346 and is also the deepest site of the depth transect. The location of Site U1422 was selected specifically to identify the timing of the onset of IRD events and to reconstruct temporal variations in its intensity and frequency. Because sea ice formation in the marginal sea, which occurs along the northwestern margin as a result of strong winter cooling (Talley et al., 2003), is closely related to the intensity of Siberian High (e.g., Tada, 2004), we expected the intensity of the IRD events to reflect the strength of the East Asian winter monsoon. Therefore, at Site U1422 we hoped to reconstruct the winter monsoon intensity through examination of IRD abundance and distribution along the northern latitudinal transect in the Japan Basin. At present, stronger winter monsoon wind produces deep water, called Japan Sea Proper Water (JSPW), through sea ice formation

doi:10.2204/iodp.proc.346.103.2015

in the northwestern part of the marginal sea (Talley et al., 2003). Consequently, sea ice formation and deepwater ventilation could also reflect winter monsoon intensity. Ikehara (2003) described millennial-scale IRD events in the northern part of the marginal sea during the last 160 k.y. Correlation of these IRD data with the lightness (L*) profile of piston Core MD01-2407 suggests that many of these IRD events coincide with intervals of high L* values, further suggesting intense deepwater ventilation that in turn coincides with Heinrich events.

Operations

Port call

Expedition 346 began with the first line ashore at the Valdez Container Terminal in Valdez, Alaska (USA), at 1120 h on 29 July 2013. The first week of Expedition 346 consisted almost entirely of port call activities. This was the first port call in Valdez, and operations proceeded very smoothly. In spite of the remote location and logistical challenges, the vessel was resupplied and departed 1 day earlier than scheduled.

The IODP-United States Implementing Organization crew and the expedition Co-Chief Scientists arrived at the ship in Valdez on 29 July after an 8 h bus ride from Anchorage. The ship's (Siem Offshore) crew arrived the following day. On day three of the port call, the Expedition 346 science party moved aboard, completing the sailing complement for the expedition.

Port call activities included routine resupply of consumables and offloading of the previous expedition's (IODP Southern Alaska Margin Expedition 341) freight. All Expedition 341 core samples were offloaded to refrigerated containers and dispatched to the IODP Core Repository at Texas A&M University (College Station, TX, USA). All microbiological samples were offloaded and dispatched to the Expedition 341 scientists' home institutions by courier. Three empty core liner boxes were also offloaded for disposal. In addition, 2441 sacks/122.1 short tons of barite, 3920 sacks/196.0 short tons of sea gel, and 1872 sacks/88.0 short tons of cement were loaded. Bunkering totals included loading 115,015 gal marine gas oil by trucks from a local Valdez refinery.

The ship's crew's activities included receipt and installation of a replacement standpipe valve, including the required X-ray certification of the high-pressure welds by a technician from Anchorage. In addition, a Schlumberger mechanic came to assist the logging engineer with repairs to the securing system holding the logging winch/transmission in place.

With port call activities completed, the R/V *JOIDES Resolution* departed for Site U1422 (proposed Site JB-3) with the last line away at 0718 h on 2 August. Departure was 28 h ahead of the scheduled departure time.

The 3556 nmi voyage to Site U1422 lasted 2 weeks at an average speed of ~10.2 kt. During the transit, we crossed two low-pressure cells with their associated strong winds and high seas, which impacted our cruising speed. Average speed over ground during those times was as slow as 7.5 kt. A total of eight time changes took place during the transit, with the clock being turned back 7 h and advanced 1 day to compensate for passage across the International Date Line. In effect, the day of 9 August was lost and the ship time jumped from 8 August directly to 10 August at 2400 h on 8 August. The last time change placed the ship at UTC + 9 h, which was the local time for all Expedition 346 sites as well as Japan and Busan, Korea.

The ship maintained good speed (11 kt) during the final days of the transit until entering the heavily trafficked Tsugaru Strait south of Hokkaido, Japan. A strong current on the bow reduced the vessel's speed over ground through the strait to 6.0 kt. This lost time was made up once exiting the strait and turning to a more northerly course, during which an average speed of 11.7 kt was achieved during the last day of the transit.

Site U1422

We arrived at Site U1422 at 1448 h on 17 August 2013. Control of the ship was shifted from bridge cruise mode to dynamic positioning mode at 1528 h. A strong gale was blowing as the ship arrived on location, which complicated the vessel's maneuvering over the location coordinates. However, the ship soon steadied over the site's coordinates, and the rig crew began picking up drill collars and making up the advanced piston corer (APC)/extended core barrel (XCB) bottom-hole assembly (BHA). All tubular joints were measured and drifted (internal diameter clearance checked) as they were made up into the drill string. By ~0300 h on 18 August, the drill string had been deployed to the seafloor.

Five holes were cored at Site U1422 using the APC and nonmagnetic core barrels (Table **T1;** see also Fig. **F2** in the "Expedition 346 summary" chapter [Tada et al., 2015a]). Two holes were cored to 9.5 m core depth below seafloor (CSF-A) (see the **"Methods"** chapter [Tada et al., 2015b]) (one core each), one

hole to 205.2 m CSF-A, one hole to 141.8 m CSF-A, and one hole to 111.6 m CSF-A. A total of 63 cores were required to obtain 502.6 m of sediment (105.2% recovery). The advanced piston corer temperature tool (APCT-3) was deployed four times.

Hole U1422A

Operations continued at Site U1422 as the drill string was tripped to 3425.0 meters below rig floor (mbrf). The top drive was picked up, and the pipe was spaced out for spudding Hole U1422A. A precision depth recorder reading for the site established a projected seafloor depth of 3450.4 mbrf. This was 4.4 m deeper than the predicted depth of 3446.0 mbrf for operations at this site. The bit was placed at 3446.4 mbrf, and Hole U1422A was started at 0340 h on the morning of 18 August. When recovered, the core barrel was full (9.96 m), preventing the possibility of determining an accurate seafloor depth. This ended Hole U1422A.

Hole U1422B

The vessel was offset 15 m north of Hole U1422A, and Hole U1422B was spudded at 0515 h with the bit placed at 3441.4 mbrf. Once again, the barrel was recovered full (9.67 m), necessitating a third attempt to establish mudline.

Hole U1422C

The vessel was offset 30 m south of Hole U1422B, and Hole U1422C was spudded at 0640 h with the bit placed at 3435.4 mbrf. When recovered, the barrel contained 4.64 m of core, establishing a seafloor depth of 3440.3 mbrf. Coring operations continued in this hole using full-length APC core barrels to 125.3 m CSF-A. Core 346-U1422C-14H required 90,000 lb of overpull, indicating that we would need to either drill over future core barrels or switch to the half APC system. Because of the success of the half APC system during the previous expedition (341), this was the tool of choice. Very successful half APC coring continued to a total depth of 205.2 m CSF-A. The top drive was set back, and the drill string was pulled clear of the seafloor at 1950 h on 19 August, ending Hole U1422C and beginning Hole U1422D. Total recovery for this hole was 215.78 m (105.2%). A total of 17 half APC cores were recovered. A total of 79.90 m of penetration was achieved with this system, recovering 86.2 m (107.9%). Four successful temperature measurements were taken using the APCT-3 temperature shoe on Cores 4H, 7H, 10H, and 13H at depths of 33.1, 61.6, 87.3, and 115.8 m CSF-A, respectively.

Hole U1422D

The vessel was offset 15 m west of Hole U1422A, and Hole U1422D was spudded at 2120 h on 19 August. The bit was placed 3 m lower (3438.4 mbrf) than it was for Hole U1422C. The mudline core contained 8.14 m of core, establishing a seafloor depth of 3439.8 mbrf. APC operations continued in this hole to 141.8 m CSF-A. At that time, the Co-Chief Scientists decided that spending further time on the hole would not be fruitful because of the increasing amount of turbidites recovered from the section. The top drive was set back, and the drill string was pulled clear of the seafloor at 1235 h on 20 August, ending Hole U1422D and beginning Hole U1422E. A total of 141.8 m of penetration was achieved, recovering 152.83 m (107.8%).

Hole U1422E

The vessel was offset 15 m east of Hole U1422A, and Hole U1422E was spudded at 1320 h on 20 August, establishing a seafloor depth of 3440.0 mbrf. Coring operations continued in this hole, recovering 14 APC cores to 111.6 m CSF-A. Two of these cores (346-U1422E-9H and 10H) were half APC cores in an attempt to recover a turbidite section of the formation where recovery had been problematic. Incomplete stroke on Cores 13H and 14H led to curtailment of coring operations for the site. Total recovery for this hole was 114.34 m (102.5%). The top drive was set back, and the drill string was pulled clear of the seafloor at 0420 h on 21 August. The drill string was recovered back aboard the vessel, the BHA was set back in the derrick, and the vessel was secured for transit. At 1142 h that same day, the vessel got under way for IODP Site U1423. This ended operations at Site U1422.

Lithostratigraphy

Drilling at Site U1422 penetrated to a maximum subbottom depth of 205 m in Hole U1422C, recovering a total of 215.78 m of sediment for a recovery rate of 105%. The shipboard lithostratigraphic program involved visual assessment of sediment composition, color, sedimentary structures, and bioturbation intensity, supplemented by petrographic analysis of smear slides and bulk mineralogic analysis by X-ray diffraction (XRD). These were used to describe and define the facies and facies associations from each hole. A total of 212 smear slides were examined from Hole U1422C to help determine lithologic names, whereas fewer were taken from Holes U1422D (49)

and U1422E (27). From Hole U1422C, 36 samples were selected for XRD analysis.

The sedimentary succession recovered at Site U1422 extends from the Pliocene to Holocene and closely follows the lithologic sequence previously identified at Site 795 (~40 km to the northeast), which is dominated by clay, silty clay, and diatomaceous clay with minor volcaniclastic material. The section is divided into two major lithologic units (I and II), distinguished on the basis of sediment composition. Unit I is further divided into two subunits based on the frequency of alternating dark and light color variations. The character of the sediment physical properties, including natural gamma radiation (NGR), magnetic susceptibility, color reflectance parameters, and density, records the distribution of the various sediment components and lithologies (see **"Physical properties"**). The major characteristics of the sedimentary sequence at Site U1422, together with some of these additional properties, are summarized in Figures **F2, F3,** and **F4.** Hole-to-hole stratigraphic correlation is shown in Figure **F5.**

Unit I

Intervals: 346-U1422C-1H-1, 0 cm, to 11H-3, 46 cm; 346-U1422D-1H-1, 0 cm, to 11H-4, 39 cm; 346-U1422E-1H-1, 0 cm, to 11H-4, 40 cm

Depths: Hole U1422C = 0–90.52 m CSF-A; Hole U1422D = 0–89.71 m CSF-A; Hole U1422E = 0–90.30 m CSF-A

Age: Holocene to early Pleistocene (2.1 Ma)

Lithology and structures

Unit I consists of Holocene to early Pleistocene silty clay and clay with lesser amounts of diatom-bearing and diatom-rich silty clay. Minor calcareous layers containing foraminifers and carbonate nodules are rare but present. Pebble-sized clasts are also found at various depths, whereas discrete tephra (volcanic ash) layers ranging in thickness from a few millimeters to >10 cm are numerous (Table **T2**). Pyrite is found as a minor component in most lithologies, whereas fine-grained tephra occurs as a dispersed component throughout much of the section based on smear slide analysis. Unit I is characterized primarily as representing fine-grained material derived from terrigenous sources. A few black spherules, likely microtektites (Fig. **F6**), were found in Sample 346-U1422C-4H-CC near the horizon of the Brunhes/Matuyama paleomagnetic boundary (~0.78 Ma: Sample 346-U1422C-5H-1, 50 cm; 37.5 m CSF-A) during foraminiferal analysis.

One of the most striking features of Unit I sediment is the alternating, decimeter-scale color-banded bedding that characterizes much of the sequence. Previous work (e.g., Föllmi et al., 1992; Tada et al., 1992) suggested that the color variations are primarily due to the organic carbon content of the dominant silty clay and clay, with dark, organic-rich intervals (dark gray to dark olive-gray) interspersed between lighter colored, organic-poor intervals (light green to light greenish gray). In addition, dark green centimeter-scale banding is common throughout the unit. The relative frequency of these color alternations is the basis for recognizing and distinguishing between Subunits IA and IB.

Bulk mineralogy

The results of XRD analysis are listed in Table **T3.** In general, Pliocene–Pleistocene sediment at this site is composed mainly of quartz, plagioclase, and clay minerals (including smectite, illite, and kaolinite and/or chlorite), as well as biogenic opal-A and minor amounts of halite and pyrite. Calcite was not detected in XRD analyses from Unit I. There may be other minor minerals that were not identified by the XRD analysis of bulk samples.

Figure **F7** shows the downcore variations in peak intensity of the identified minerals at Site U1422. In general, quartz, plagioclase, illite, kaolinite and/or chlorite, and pyrite contents show a long-term trend toward increasing counts uphole. In general, the peak heights of these minerals are higher in Unit I and typically lower in Unit II. In contrast, K-feldspar drops sharply downhole across the Unit I/II boundary and is largely absent in the upper part of Unit II but increases again below ~130 m CSF-A before largely disappearing near the base of the site. Peaks of opal-A are generally lower in Unit I and higher in Unit II. The peak intensity of pyrite at 6.98 m CSF-A in Hole U1422C is very strong. Halite is always present in samples, reaching a maximum content at 9.98 m CSF-A in Hole U1422C.

Subunit IA

Intervals: 346-U1422C-1H-1, 0 cm, to 7H-5, 148 cm; 346-U1422D-1H-1, 0 cm, to 8H-1, 27 cm; 346-U1422E-1H-1, 0 cm, to 7H-2, 100 cm

Depths: Hole U1422C = 0–59.58 m CSF-A; Hole U1422D = 0–59.87 m CSF-A; Hole U1422E = 0–59.50 m CSF-A

Age: Holocene to late early Pleistocene (1.4 Ma)

Lithology and structures

Subunit IA is composed mainly of silty clay and clay with subordinate amounts of diatomaceous clay. Tephra layers are a minor but common component in Subunit IA and intercalate in the silty clay sequence. Subunit IA is primarily recognized by having

a much higher frequency of dark layer occurrence than Subunit IB (Fig. F8). In general, low L*, a*, and b* values in color and high NGR values with significant fluctuations are characteristic of Subunit IA.

Bioturbation is slight to absent throughout this subunit and is another criterion for separating Subunit IA from IB. Where evident, bioturbation is more common in lighter colored intervals, whereas dark colored layers often show evidence of fine parallel lamination. Rare beds contain fining-upward size grading. Other features observed in Subunit IA include scattered pebble- to cobble-sized clasts and rare small normal microfaults.

Composition

The principal components of lithologies in Subunit IA are terrigenous, volcanic, and biogenic. The biogenic fraction is dominated by diatoms and sponge spicules and includes rare foraminifers. Terrigenous components are dominated by clay and fine silty clay fractions. Clay minerals are the dominant siliciclastic component of the clay and silt, usually in contents of between 10% and 50%. Lithic and quartz grain contents are also relatively high, ranging from abundant to dominant (up to 75%). Volcanic glass shards and pumice combine to nearly 100% in tephra layers but are sometimes mixed with minor siliciclastic and biogenic materials as well as opaque minerals.

Pyrite, or more likely a precursor black iron sulfide, is present as submillimeter-scale disseminated framboids (or irregular masses) coexisting with other opaque minerals. Diagenetic calcite in small size needle-like crystals is observed at multiple depths and is typically associated with layers of more indurated sediment (see **"Lithology and structures"** and **"Bulk mineralogy"**).

In Section 346-U1422C-5H-1A, 63.5 cm (33.735 m CSF-A), a thin (<0.5 cm thick) volcaniclastic layer containing large biotite flakes is found interbedded in greenish silty clay. This particular composition is quite unique at Site U1422 (monospecific and in phenocrystal texture), as the tephra layers commonly found in the section most typically consist of volcanic glass and crystals.

The vitric components of the tephra layers have a wide range of forms, sizes, and shapes. Glass shards and fragments have sharp angles (so-called "bubble-wall" type), and vesicular glass fragments that include bubbles (so-called "pumice" type) are frequent. Some of the glass grains are rectangular fragments presenting a fibrous structure that clearly reflects the presence of subparallel pipe vesicles (Fig. F9). Alteration may occasionally affect the vitric grains, but most of the volcanic material appears pristine. In Section 346-U1422D-6H-6A, 23 cm, a thin level of authigenic zeolite, possibly resulting from the alteration of tephra, is observed yielding cruciform crystals of phillipsite (Fig. F10).

The biogenic components found in Subunit IA deposits are rarely dominant. However, where found, biosiliceous fossils (diatoms, sponge spicules, radiolarians, and rare silicoflagellates) can reach up to 75% in contents in the bulk sediment. Calcareous nannofossils and foraminifers are nearly absent except in the uppermost part of the unit (Cores 346-U1422C-1H and 2H).

Subunit IB

Intervals: 346-U1422C-7H-5, 148 cm, to 11H-3, 46 cm; 346-U1422D-8H-1, 27 cm, to 11H-4, 39 cm; 346-U1422E-7H-2, 100 cm, to 11H-4, 40 cm

Depths: Hole U1422C = 59.58–90.52 m CSF-A; Hole U1422D = 59.87–89.71 m CSF-A; Hole U1422E = 59.50–90.30 m CSF-A

Age: early Pleistocene (1.4–2.1 Ma)

Lithology and structures

Subunit IB is transitional downhole from Subunit IA and is identified by a decrease in the frequency of the dark and light color alternation (Fig. F11). Silty clay and clay are again major lithologies in this subunit with subordinate laminated diatom-rich silty clay that is typically brown in color. Bioturbation increases gradually with depth, and sediment mottling and disruption of laminae and color banding is more prevalent. Discrete tephra layers with a thickness of 1–2 cm commonly occur in the subunit. Fining-upward turbidite beds with sharp and erosional basal contacts occur at the lowermost part of Subunit IB. Each turbidite bed is a few to several centimeters in thickness. Sediments comprising the light colored layers in Subunit IB are generally lighter (with higher L* value) than those in Subunit IA. A subtle decrease in NGR values of Subunit IB sediment suggests decreasing amounts of organic matter and/or clay mineral content relative to Subunit IA.

Composition

The results of smear slide analyses show that the most common lithology consists of terrigenous components dominated by clay and fine silty clay fractions. As in Subunit IA, tephra layers occur interspersed in the section, but these are more frequent in Subunit IB than in Subunit IA (see **"Lithology and structures"**) and are mainly composed of well-preserved volcanic glass and crystals (see **"Subunit IA"**).

Clay and silty clay sediment contains abundant clay minerals, rock fragments, and other siliciclastic minerals (mainly quartz). Scattered sand layers are observed in Subunit IB, containing ~60% siliciclastic material (lithics) and ~35%–40% volcanic glass and crystals. Occasionally, small amounts of calcareous debris (fragmented foraminifers) are found in the sediment (usually <5%).

In general, calcareous biogenic components are poorly preserved in Subunit IB (<5% or absent). Biogenic silica is common at various depths, and smear slide analyses reveal that diatom-rich sediment mainly corresponds to brown laminated intervals (see **"Lithology and structures"**). In these intervals, the siliceous biogenic component can reach up to 70% of the bulk composition (Fig. **F12**).

Unit II

Intervals: 346-U1422C-11H-3, 46 cm, to 31H-CC, 30 cm; 346-U1422D-11H-4, 39 cm, to 16H-CC, 26 cm; 346-U1422E-11H-4, 40 cm, to 14H-5, 86 cm

Depths: Hole U1422C = 90.52–205.55 m CSF-A; Hole U1422D = 89.71–142.51 m CSF-A; Hole U1422E = 90.30–111.67 m CSF-A

Age: early Pleistocene to Pliocene (>2.1 Ma)

Lithology and structures

Unit II is dominantly composed of moderate to heavily bioturbated diatom ooze and diatomaceous silty clay and clay with numerous turbidite beds (Fig. **F13**). Minor hard micritized layers and calcareous nodules occasionally occur. Unit II is primarily distinguished from Unit I based on a significant increase in diatom content relative to terrigenous sediment downhole. A remarkable decrease in NGR values coincides with the increasing diatom content of Unit II sediment, whereas a* and b* color reflectance values show a slight overall increase in Unit II. Unit II sediment is also more heavily bioturbated than that of Unit I, with the degree of bioturbation changing vertically. Tephra beds are frequently found in the upper part of Unit II, but their number and bed thickness decrease significantly below ~130 m CSF-A. The thickest tephra layer (maximum thickness = 27 cm) occurs in the upper part of Unit II (107.36–107.72 m CSF-A in Hole U1422C). The lower 9 cm of the tephra is darker (dark gray) and coarser (very fine sand size) than the upper 18 cm (light gray and coarse silt size).

Intercalation of numerous turbidite layers within the diatomaceous silty clay is another characteristic of Unit II. Each turbidite bed is a few centimeters thick. The frequency of turbidites changes remarkably from only a few to >10 in a section. Turbidite beds show fining-upward grading with sharp erosional basal contacts (Fig. **F14**) and can be divided into what are termed here turbidite mud and turbidite sand. Turbidite mud is relatively thick (several centimeters in thickness) and has a mixture of grain sizes compared with thinner, coarser turbidite sand (normally <1 cm in thickness). Parallel and/or cross lamination can be recognized in many turbidite sands above their base. Turbidite mud is characterized by brown color in the upper part and olive-gray in the lower part. The upper contact of turbidite mud is usually gradual and sometimes bioturbated. The grain composition of turbidite sand gradually changes from more volcanic origin (volcanic glass shards with quartz and rock fragments) in the upper part of Unit II to more siliciclastic grain dominated (volcanic glass shards, quartz, and rock fragments with volcanic glass shards) in the lower part. Both tephra layer occurrence and turbidite sand composition suggest a greater volcanic influence on sedimentation in the upper part of Unit II compared to the lower part.

Composition

As in Subunits IA and IB, the major lithologies in Unit II are dominated by fine-grained terrigenous material, except in turbidite layers where the grain size is generally sand or silty sand. On average, sediment in turbidite beds consists of ~70% siliclastic grains, <10% biogenic silica (mostly diatoms and diatomaceous sponge spicules), and between 10% and 20% tephra. Fragmented and poorly preserved foraminifers occur occasionally.

The composition of sandy beds is observed to be slightly different from the bottom to the top of Unit II. The sand layers of the lower part of Unit II are mostly siliciclastic in bulk composition (up to 80%) with a tephra fraction of ~5%. In the upper part of Unit II, the tephra fraction was estimated to reach as high as 10%. These estimates are semiquantitative, based on shipboard comparison to composition charts, and should not be taken as absolute. The composition and grain size typically change vertically in a turbidite bed (Fig. **F15**) indicating grain sorting during its deposition.

Sandy beds are often associated with brown silty clay and greenish white silty clay. In smear slides, the brown silty clay contains a mixture of siliciclastic and biosiliceous grains (mainly diatoms, up to 20%). The greenish white silty clay typically contains fewer siliciclastic silt grains and a larger biosiliceous component, though diatom preservation can be poor.

Bulk mineralogy

The results of XRD analyses conducted on Hole U1422C sediment are listed in Table **T3.** In general, the bulk mineral composition of Unit II sediment is similar to that of Unit I. Figure **F7** indicates a slight downhole decrease in quartz, plagioclase, illite, kaolinite and/or chlorite, and pyrite contents, countered by a long-term increase in opal-A. However, the differences are subtle and may be biased by the relatively low resolution of the shipboard sampling interval. The most significant occurrence of calcite in Unit II was observed in the form of a yellow-brown concretion and cemented layer found at 105.55 m CSF-A in Hole U1422C.

Discussion

Overall, the sedimentary succession at Site U1422 records a history of largely terrigenous deposition since the Pliocene (<3.9 Ma). Over this interval, sediment is predominantly silty clay and clay with less abundant diatomaceous sediment. Nonetheless, the downhole distribution of biosiliceous components provides a useful means of dividing the section into units, following the convention previously used at nearby Site 795, with Unit II defined by a significant increase in diatom-rich strata as compared to Unit I (Tada and Iijima, 1992; Tada, 1994). Unit II sediment was probably deposited during a period of elevated biological productivity and good overall circulation in the basin. Well-oxygenated conditions and a steady food supply for the benthos in the deep basin are indicated by the moderate to heavy bioturbation of Unit II sediment.

A significant difference between the Unit II sequence recovered at Sites 795 and U1422 is the prevalence of turbidites in the latter, which suggests either a more proximal source of terrigenous materials or a location more susceptible to downslope movements. The turbidites continue up to the lower Subunit IB. Site U1422 is located in a basin west of the Okushiri Ridge, which is thought to be a young and immature plate boundary. Initiation of subduction along the boundary has been inferred to be 1.8 Ma (Tamaki et al., 1992). Turbidite deposition is possibly related to tectonic movements along the Okushiri Ridge. Further shore-based research may test this hypothesis.

In contrast, Unit I sediment at both sites is very similar and lithologic variations appear to be highly correlative. The Pleistocene–Holocene sediment that makes up Unit I is characterized by lower siliceous content and rhythmic alternation in colors marked by light colored (gray to light greenish gray) silty clay to clay intervals interbedded with darker colored (dark olive-gray to black) layers. Although smear slides are only semiquantitative, their content suggests that the dark layers are often richer in some combination of organic debris, pyrite, or biogenic skeletal material (usually diatoms). The pronounced lack of bioturbation through much of Unit I and the gray to greenish hue of much of the sediment are consistent with lower deepwater oxygen levels to, at times, anoxic seafloor conditions.

Within Unit I, an increase in the frequency of dark colored sediment intervals is used to distinguish between two subunits, with Subunit IA marked by decimeter-scale dark layers that are more frequent, more distinct, and typically better laminated than in Subunit IB. This pattern parallels previous observations from Site 795.

Tephra layers are present but are a relatively minor constituent of Subunit IA sediment, increasing in frequency in Subunit IB and the upper part of the Unit II sequence. Discrete tephra layers decrease downsection in Unit II, a trend apparent at Site 795 as well. In contrast, turbidite deposition in Unit II is much more prevalent at Site U1422 than at Site 795. Turbidite composition varies within Unit II, with a larger fraction of reworked tephra grains incorporated in turbidite deposits in the upper part of Unit II and a greater proportion of siliciclastic grains in turbidites from deeper in the Unit II sequence. This is consistent with observations of in situ tephra distribution that suggest greater regional volcanism during the time period represented by upper Unit II/Subunit IB sediment.

Biostratigraphy

At Site U1422, a ~205 m thick succession of Pliocene to Holocene sediment was recovered. Calcareous nannofossils are rare and sporadically distributed in the upper 40 m of the sequence. Planktonic foraminifers are rare to absent, with moderate to poor preservation throughout most of the succession but are abundant in thin calcareous layers observed at 24–46 m CSF-A. No in situ planktonic foraminifer zones were documented because of assemblage reworking. The radiolarian assemblages show moderate to good preservation except in the interval between 52 and 78 m CSF-A. The radiolarian biostratigraphic zonation ranges from the *Cycladophora sakaii* Zone (Pliocene) to the *Botryostrobus aquilonaris* Zone (Late Pleistocene). The diatom assemblage is generally moderate to well preserved; however, there are several intervals in which valve preservation becomes poor to moderate. The diatom stratigraphy spans the interval from Zone NPD 12 (Pliocene) to NPD 7 (Late Pleistocene). The nannofossil, radiolarian, and diatom datums and zonal schemes generally agree with only some minor inconsistencies. The integrated cal-

careous and siliceous microfossil biozonation is shown in Figure F16, with microfossil datums shown in Table T4. An age-depth plot including biostratigraphic datums is shown in Figure F17. See "Stratigraphic correlation and sedimentation rates" for a discussion of sedimentation rates at Site U1422. Benthic foraminifers occur intermittently throughout the succession and show generally poor preservation. The overall assemblage composition indicates lower bathyal to abyssal paleodepths. The rare occurrence of calcareous microfossils reflects dissolution at the seafloor. The rare occurrence of agglutinated benthic foraminifers is probably due to unfavorable dysoxic conditions at the sediment/water interface.

Calcareous nannofossils

Calcareous nannofossil biostratigraphy is based on analysis of core catcher and split-core section samples from Hole U1422C and split-core section samples from Hole U1422D. Depth positions and age estimates of biostratigraphic marker events are shown in Table T5. Most of the samples studied at Site U1422 lack nannofossils (Figs. F16, F18). Nannofossils are abundant in short and sporadic Pleistocene intervals (Samples 346-U1422C-3H-4, 126 cm [19.87 m CSF-A], 3H-5, 15 cm [20.26 m CSF-A], 5H-4, 66 cm [38.17 m CSF-A], and 346-U1422D-3H-7, 26 cm [21.37 m CSF-A]). With the exception of those samples, nannofossils are generally rare and etched when present. Nannofossils are absent below Sample 346-U1422C-7H-CC (62.17 m CSF-A) through significant portions of the Pliocene to early Pleistocene, with the exception of rare occurrences in Core 346-U1422C-19H (148.17–149.24 m CSF-A; Table T5).

In some samples, calcareous nannofossils co-occur with foraminifers (e.g., Samples 346-U1422C-4H-1, 59 cm [24.20 m CSF-A], 4H-5, 95 cm [30.54 m CSF-A], and 5H-4, 66 cm [38.17 m CSF-A]); however, the majority of samples with foraminifers lacked calcareous nannofossils (Fig. F18). Low-diversity nannofossil assemblages include *Braarudosphaera bigelowii, Coccolithus pelagicus, Emiliania huxleyi, Gephyrocapsa caribbeanica, Gephyrocapsa muellerae, Gephyrocapsa oceanica*, small *Gephyrocapsa* (<4 µm), *Pontosphaera* spp., and *Reticulofenestra minutula*. Nannofossil Zones CN15/NN21 are recognized using the base of *E. huxleyi* (Samples 346-U1422C-3H-5, 15 cm [20.26 m CSF-A], and 346-U1422D-3H-6, 115 cm [20.76 m CSF-A]). Nannofossil Zones CN14b/NN20 are also recognized based on the presence of *G. oceanica* and the absence of *Pseudoemiliania lacunosa* (24.19–38.17 m CSF-A in Hole U1422C and 21.36–28.5 m CSF-A in Hole U1422D). The downhole extension of Zones CN14b/NN20 is not constrained because of the absence of nannofossils below 38.17 and 28.5 m CSF-A in Holes U1422C and U1422D, respectively.

Radiolarians

A total of 31 core catcher samples from Hole U1422C were prepared for radiolarian analyses. Radiolarians are generally common to abundant in the sequence (Fig. F18), although they are rare or absent between 52.3 and 77.8 m CSF-A (Samples 346-U1422C-6H-CC through 9H-CC).

In Hole U1422C, key species that define the base or top of the *Stylatractus universus* and *Eucyrtidium matuyamai* radiolarian zones were not observed. Six secondary datums, however, were found (Table T4). The last occurrence (LO) of Late Pleistocene datums *Amphimelissa setosa* (0.08 Ma) and *Spongodiscus* sp. (0.29 Ma) are observed in Samples 346-U1422C-2H-CC (14.3 m CSF-A) and 3H-CC (24.0 m CSF-A), respectively. The LO of *Axoprunum acquilonium* is in Sample 10H-CC (87.8 m CSF-A) just below the poor preservation interval between 52.3 and 77.8 m CSF-A (Samples 6H-CC through 9H-CC). The Pleistocene/Pliocene boundary is close to the first occurrence (FO) of *Cycladophora davisiana* (2.7 Ma) in Sample 16H-CC (135.1 CSF-A) and the LO of *Hexacontium parviakitaensis* (2.7 Ma) in Sample 18H-CC (144.4 m CSF-A). At the bottom of Hole U1422C (205.6 m CSF-A, Sample 31H-CC), the estimated age is younger than 3.9–4.3 Ma, based on the occurrence of *H. parviakitaensis* and the absence of *Dictyophimus bullatus*.

Radiolarian faunal assemblages are closely related to surface and deepwater oceanographic conditions (e.g., Casey, 1977). For example, *Dictyocoryne truncatum* and the *Octopyle/Tetrapyle* group are typical warm-water radiolarians related to the TWC (Itaki et al., 2007). Sporadic occurrences of these species in Hole U1422C (Table T6) suggest minor TWC influence since 4 Ma. *Ceratospyris borealis*, a subarctic Pacific species (Motoyama and Nishimura, 2005), is one of the most common species in the sequence, especially shallower than Sample 346-U1422C-20H-CC (153.8 m CSF-A).

Diatoms

Diatom biostratigraphy is based on smear slides from core catcher samples. A total of 31 core catcher samples were examined, and five datums were identified (Table T4). Although diatoms were identified and counted across at least an entire coverslip transect, the number of transects was increased as needed because identification was not always possible because of the high clay content, too high diatom content,

and/or high level of fragmentation. Diatom species counts are shown in Table T7. Diatoms are absent or rare in the upper 100 m CSF-A, becoming dominant, abundant, or common between 100 and 210 m CSF-A (Fig. F18). This shift coincides with the Pliocene–Pleistocene transition. Overall, five diatom zones (Fig. F16) were found: NPD 12 (Samples 346-U1422C-1H-CC through 5H-CC), NPD 11/10 (Samples 6H-CC through 12H-CC), NPD 9 (Samples 13H-CC through 20H-CC), NPD 8 (Samples 21H-CC through 25H-CC), and the top of NPD 7 (Sample 26H-CC). The poor preservation of diatoms in the upper 100 m prevents the identification of Zones NPD 11 and NPD 10, and the LO of *Actinocylus oculatus* datum was not found. The base of Hole U1422C is younger than 5.56 Ma (because of the occurrence of *Shionodiscus oestrupii*), with the oldest age estimate obtained from Sample 346-U1422C-25H-CC, which is younger than 3.4–3.0 Ma (FO of *Neodenticula koizumii*).

Reworked *Neodenticula kamtschatica* valves were found in Samples 346-U1422C-5H-CC, 7H-CC, and 11H-CC. This reworking was also noted by Koizumi (1992) at Site 795, the closest location to Site U1422 for which reference information is available. Therefore, the presence of this species in the poorly preserved samples (346-U1422C-1H-CC, 2H-CC, 4H-CC, and 6H-CC to 10H-CC) and in Zone NPD 8 samples (21H-CC to 25H-CC) was not considered for biostratigraphic purposes.

Freshwater species (Table T7) were found in Samples 346-U1422C-1H-CC, 2H-CC, 11H-CC, 17H-CC, 25H-CC, 29H-CC, and 30H-CC. Opal phytoliths (land plant silica concretions) were found in Cores 346-U1422C-10H, 14H, and 16H. The presence of these two indicators might be related to either freshwater input and/or wind transportation. *Chaetoceros* spores, which are upwelling indicators, were found in Samples 346-U1422C-2H-CC, 3H-CC, 5H-CC, 11H-CC to 17H-CC, 19H-CC, 21H-CC, and 23H-CC to 31H-CC.

Highly fragmented large centric diatoms (>50 µm) were found from 110 to 210 m CSF-A. These fragments are very well preserved, and their fragmentation could be the result of bottom transport rather than dissolution. However, significant numbers of >150 µm centric diatoms belonging to the *Coscinodiscus* and *Arachnodiscus* genera (Fig. F19) were found in the >150 µm residue from the foraminifer samples (346-U1422C-5H-CC, 6H-CC, and 12H-CC to 31H-CC). The fact that such large diatoms were not found in the smear slides may imply breakage of the specimens when making these. However, this fragmentation causes a biased number of counts, as the diatom species can often be identified but cannot be counted as a whole valve as it does not contain >50% of the valve area. Therefore, the counts are biased toward the smaller pennate diatoms that can be easily found at 1000× magnification. In order to assess this fragmentation, a simple fragmentation index was calculated to qualitatively assess its impact. The index is calculated by dividing the number of centrics by the number of pennate diatoms counted. The closer the index is to zero, the higher the fragmentation, assuming that no intact centrics are found. The fragmentation index always needs to be complemented with information either from the foraminifer sample or from microscopic observation at 630× magnification in order to verify the presence of large centrics.

The presence of specimens with a diameter >150 µm belonging to the genera *Arachnodiscus* and *Coscinodiscus* are only found in the foraminifer sample residue (>150 µm), as these are not observable on the microscopic slides because they break when the slides are prepared. Some *Coscinodiscus marginatus* >50 and >100 µm were found in the smear slides from Samples 346-U1422C-3H-CC, 9H-CC, 13H-CC, 16H-CC, 20H-CC, 24H-CC, 25H-CC, and 28H-CC to 30H-CC. Nevertheless, in order to identify the species found in the foraminifer sample residue >150 µm, some specimens were observed with the scanning electron microscope (Fig. F19). These large diatoms were also found in the mudline sample from Core 346-U1422D-1H.

Planktonic foraminifers

Planktonic foraminifers were examined in core catcher samples from Holes U1422A (1 sample), U1422B (1 sample), U1442C (30 samples), and U1422D (2 samples) and were supplemented by toothpick samples from Hole U1422C (13 samples) after the core sections were split. Additionally, mudline samples recovered in Holes U1422C and U1422D were investigated. Planktonic foraminifers are confined to the upper part of the succession recovered at Site U1422 (Fig. F18; Cores 346-U1422C-1H to 8H and Hole U1422D). Within this interval, the assemblages are impoverished and generally poorly preserved with evidence of intense dissolution and/or pyritization. In the 35 (~30 cm^3) samples examined from the core catchers, only 2 samples contain >35 specimens and 5 samples contain 5 or fewer specimens (Table T8). All other core catcher samples are barren. Of the 13 toothpick samples examined from thin carbonate-rich layers, 4 samples contained >70 specimens, 1 sample contained 44 specimens, and 1 had only 2 specimens. All other toothpick samples were barren. The abundance of planktonic foraminifers per standardized volume is,

thus, generally much higher in the thin carbonate-rich layers in the upper part of the succession (to 58.66 m CSF-A; Sample 346-U1422C-7H-5, 55–56 cm) than in core catcher samples. However, most of the thin carbonate-rich horizons are interpreted to be turbiditic layers (see **"Lithostratigraphy"**), which mainly contain reworked and size-sorted planktonic foraminiferal tests.

The Site U1422 planktonic foraminiferal assemblages are characteristic of cold, midlatitude, restricted environments, consisting mainly of *Globigerina bulloides* and *Neogloboquadrina pachyderma* (sinistral) with rare occurrences of *Globigerina umbilicata, Globigerina quinqueloba, N. pachyderma* (dextral), *Neogloboquadrina dutertrei* (= *Neogloboquadrina himiensis*), *Neogloboquadrina incompta*, and *Neogloboquadrina kagaensis* group (*Neogloboquadrina kagaensis* and *Neogloboquadrina inglei*; Fig. **F20**). A biostratigraphy based on planktonic foraminifers was not generated at this site, as index markers were mainly reworked. Furthermore, the assemblage zones defined by Maiya (1978) for onshore sections in northern Japan are not applicable at this site because of the lack of diagnostic species in core catcher samples. Taxon relative abundance and estimates of assemblage preservation are presented in Table **T8.**

Benthic foraminifers

Benthic foraminifers were examined in core catcher samples from Holes U1422A (1 sample), U1422B (1 sample), U1442C (30 samples), and U1422D (2 samples) and were supplemented by samples from Hole U1422C after cores were split. Mudline samples recovered in Holes U1422C and U1422D were also investigated. Samples with an average volume of ~30 cm^3 were processed from all core catchers to obtain quantitative estimates of benthic foraminiferal distribution patterns downhole. To assess assemblage composition and variability downhole, all specimens from the >150 µm fraction were picked and transferred to slides prior to identification and counting. The presence and distribution of benthic foraminifers were additionally checked in the 63–150 µm fraction to ensure that assemblages in the >150 µm fraction were representative and that small species such as phytodetritus feeders or small infaunal taxa were not overlooked. Benthic foraminifers occur intermittently through the ~200 m thick, biosiliceous-rich succession of Pliocene to Pleistocene age (Fig. **F18;** Table **T9**). Abundance is generally low, and preservation varies significantly. The assemblages predominantly consist of rare calcareous and agglutinated taxa, and their overall composition indicates lower bathyal to abyssal paleodepths throughout the Pleistocene and Pliocene. Prominent variations in the downcore distribution of benthic foraminifers appear to reflect intense dissolution and highly dysoxic conditions at the seafloor (Fig. **F21**).

A total of 14 benthic foraminiferal taxa were identified. Census counts from core catcher and split-core section samples are presented in Table **T9.** Figure **F18** summarizes the downcore distribution of the more common benthic foraminiferal taxa in core catcher samples from Hole U1422C. Species recorded include *Cibicidoides robertsonianus, Eggerella bradyi, Fursenkoina bradyi, Globobulimina pacifica, Globobulimina pupoides, Melonis pompilioides*, and *Miliammina echigoensis* (Fig. **F21**). The presence of *F. bradyi* and *Globobulimina* spp., taxa that are sensitive to changes in organic flux and tolerant of low oxygen conditions, suggests that changes in surface productivity and bottom water oxygenation occurred throughout the Pleistocene to Pliocene, possibly associated with glacial–interglacial and millennial-scale climate fluctuations. However, the low resolution of our shipboard data set prevents detection of variability that may occur on orbital to suborbital timescales. Well-preserved diatoms and radiolarians are common to abundant in sediment residues >150 and >63 µm throughout the succession and become dominant in most samples deeper than 78 m CSF-A. Pyritized burrows are common in most of the >150 and >63 µm residues examined.

The agglutinated species *M. echigoensis* is intermittently present from Samples 346-U1422C-15H-CC (132 m CSF-A) to 29H-CC (196 m CSF-A). This taxon is typically found in Pliocene onshore successions of Japan (Kato, 1992; Brunner, 1992). At ODP Sites 794, 795, and 796, the last occurrence of this species was recorded near the Pliocene/Pleistocene boundary.

Ostracods

No ostracods were found in the core catcher samples examined at this site.

Mudline samples

Mudline core top samples from Holes U1422C and U1422D were gently washed to preserve fragile agglutinated specimens with extremely low fossilization potential. The mudline sample from Hole U1422C is barren of benthic and planktonic foraminifers and mainly contains abundant and well-preserved diatoms, radiolarians, and sponge spicules. The mudline sample from Hole U1422D, which had a substantially larger volume than in Hole U1422C, contains only rare benthic foraminifers, including one specimen of *Reophax*, one specimen of *Saccammina*, and one specimen of *Rhizammina*, as well as a few fragile soft-bodied komokiacean-like foramin-

ifers (Fig. F22) and tubular organically cemented agglutinated foraminifers, which were all stained with rose bengal. The mudline sample from Hole U1422D also contains a few fish teeth and abundant diatoms, radiolarians, and sponge spicules.

Geochemistry

Site U1422 is located ~40 km from Site 795 (Shipboard Scientific Party, 1990). As such, the sedimentary record and geochemical profiles were expected to be similar. Several processes impact the pore water and solid-phase geochemistry at Site 795. Over the upper 200 meters below seafloor (mbsf), the modest degradation of organic carbon drives a series of microbially mediated reactions. Leg 127 found these reactions lead to a sulfate–methane transition (SMT) at ~80 mbsf, as well as precipitation of authigenic minerals such as sulfides and carbonates. At Site 795, the opal-A–opal-CT transition occurs between 290 and 325 mbsf, where diatoms and radiolarians recrystallize (Shipboard Scientific Party, 1990; Nobes et al., 1992). Also, basalt was encountered at 684 mbsf (Shipboard Scientific Party, 1990). Although the latter processes occur below the 200 m target depth of Site U1422, they affect overlying pore water chemistry through diffusion gradients (Murray et al., 1992).

The initial and main focus of the geochemistry program at Site U1422 was to better delineate the diagenetic environment in the upper 200 m of sediment. In particular, we desired to refine sediment and interstitial water profiles that reflect inputs and outputs from organic matter degradation. This approach included determination of the dissolved species examined at Site 795 at lower depth resolution and dissolved species not examined at Site 795 (Mn and Ba).

As became clear from rapid alkalinity and methane analyses of squeezed interstitial water (IW-Sq) and headspace (HS) samples, the diagenetic environment at Site U1422 is somewhat similar to that at Site 795, but several key reactions occur much shallower in the sedimentary column. For example, the SMT occurs at ~30 m CSF-A and gas voids become common below ~50 m CSF-A. This difference prompted modification of the basic plan for Site U1422 (see **"Geochemistry"** in the "Methods" chapter [Tada et al., 2015b]). Effectively, two experiments were added to the program. The first was a study to determine if the color of interstitial water changed downhole at a site with modest methane concentrations; the second was a study to examine alkalinity in samples acquired by Rhizons across the SMT.

Sample summary and analytical issues

During operations at Site U1422, the geochemistry team collected and analyzed a range of samples. These included the following (Tables **T10, T11, T12, T13, T14**):

- 1 mudline (ML) water sample from the inside of the core liner above the sediment of Core 346-U1422C-1H. We collected 50 mL.
- 47 interstitial water samples from whole-round squeezing (IW-Sq) from Holes U1422A (2 samples) and U1422C (45 samples) at nominal 4.5 m spacing. For most samples, we collected between 35 and 45 mL of interstitial water.
- 33 interstitial water samples from Rhizons (IW-Rh) from the bottom sections of Core 346-U1422E-3H and the top sections of Core 4H. This interval was chosen during drilling because it should span the SMT, based on alkalinity and methane data generated for Hole U1422C, basic geochemical theory, and rapid cross-hole stratigraphic correlation. We collected between 4 and 10 mL from each Rhizon. With these volumes, a limited number of analyses were conducted (Table **T11**).
- 47 sediment samples from the interstitial water squeeze cakes of Holes U1422A (2 samples) and U1422C (45 samples).
- 50 HS gas samples. Most of these (43) were paired with IW-Sq samples, and 7 were placed at section breaks in Cores 346-U1422E-3H and 4H where Rhizons were taken.
- 7 Vacutainer (VAC) samples recovered from gas expansion voids with air-tight syringes from Holes U1422C and U1422D.

Beyond the rapid pace of drilling at Site U1422, which meant a large fraction of time devoted to squeezing and weighing, two issues affected our geochemistry program at this location. First, the chloride titrator, the ion chromatograph, and the spectrophotometer each needed repairs in the middle of analysis. As noted below, there also appears to have been problems with our inductively coupled plasma–atomic emission spectroscopy (ICP-AES) analyses of Ba and Sr. Additionally, as discussed below, several whole rounds taken for squeezing seem to have been contaminated on recovery.

Carbonate and organic carbon

Sediment recovered from Site U1422 had only minor amounts of $CaCO_3$ (Fig. F23). Some samples that may have represented thin carbonate turbidite layers

(as observed by the micropaleontologist group) had $CaCO_3$ contents as high as 20 wt% at 164 m CSF-A. However, most samples had $CaCO_3$ values <1 wt%. Total organic carbon (TOC) content varied between 1 and 3 wt% in the upper 50 m CSF-A (Table T10). Below 50 m CSF-A, TOC contents are consistently <1.5 wt%. Across all samples, TOC contributes the vast majority (94%) of the total carbon. Total nitrogen content is <0.40 wt% in samples from Site U1422.

Over the uppermost 50 m CSF-A, the carbonate and TOC data at Site U1422 appear similar to those at Site 795 (Shipboard Scientific Party, 1990). Between 50 and 160 m CSF-A, TOC is generally lower at Site U1422. The variance in TOC values should be considered when selecting and processing samples for certain organic geochemistry analyses (e.g., compound specific isotopes of biomarkers). Further analysis of discrete samples may yield short depth intervals with higher TOC contents, as might be indicated by darker core material.

Dissolved iron and manganese

The Fe profile (Fig. F24) displays a series of peaks with depth. Such Fe profiles have been documented at sites where organic carbon degradation leads to generation of methane and hydrogen sulfide (e.g., ODP Site 1230 at the Peru margin [Shipboard Scientific Party, 2003a] and ODP Site 1244 at the Hydrate Ridge [Shipboard Scientific Party, 2003b]).

The Mn profile (Fig. F24) is more straightforward. Dissolved Mn concentration is close to the detection limit (0.3 µM) in the mudline sample. Below, concentrations rise to a peak of 111 µM centered at ~4 m CSF-A and decrease to ~11 µM at 35 m CSF-A. From ~35 to 70 m CSF-A, dissolved Mn concentrations remain low with values between 6 and 10 µM. Values then increase to 30 µM at 103 m CSF-A. Concentrations range between 20 and 40 µM from 80 m CSF-A to the maximum depth drilled, 202 m CSF-A.

At locations with even modest organic matter input, dissolved Fe and Mn concentrations typically rise in shallow sediment because of Fe and Mn oxide dissolution (e.g., Froelich et al., 1979). For Mn and at sites with high alkalinity, a common phase is rhodochrosite ($MnCO_3$). Rhodochrosite has been documented between 50 and 700 mbsf at ODP Site 799 (Matsumoto, 1992). Another possibility is Mn-rich calcite, as perhaps indicated by the low dissolved Ca concentrations at this depth (Fig. F23). In any case, our results suggest precipitation of an Mn-bearing carbonate phase between 35 and 80 m CSF-A at Site U1422.

Dissolved Fe exhibits a more complicated profile with depth. In some cases, this may occur because Fe can form a series of authigenic minerals, including oxides (magnetite), sulfides (greigite and pyrite), carbonates (ankerite and ferroan dolomite), and Fe-rich clay (glauconite). Horizons of pyrite, ferroan dolomite, and glauconite have been documented in the upper few hundred meters of sediment at several sites in the marginal sea (Föllmi and von Breymann, 1992; Matsumoto, 1992). The complex Fe profile at Site U1422 may indicate that various Fe-rich minerals are precipitating and dissolving across multiple depth intervals in the sediment column. The Fe profile may also be influenced by dissolved iron reacting with HS^- during the anaerobic oxidation of methane (AOM), as discussed below.

Fe and Mn minerals are important to the paleoceanographic objectives of the expedition because they impart color and magnetism to the sediment. In principle, with very detailed pore water analyses, precise depths of Fe and Mn mineral dissolution and precipitation could be identified. Rhizon sampling at Site U1422 suggests that such Fe and Mn profiles can be generated (Fig. F24).

Alkalinity, ammonium, and phosphate

Alkalinity, NH_4^+, and PO_4^{3-} exhibit similar profiles at numerous locations with significant amounts of organic matter degradation. This is the case at Site U1422 (Fig. F25).

Alkalinity increases from 2.5 mM in the mudline sample to 26 mM at 35 m CSF-A. The value for the seafloor is close to that measured for bottom water in the region (2.4 mM; Tishchenko et al., 2012). Below this rapid rise, alkalinity steadily decreases to 18 mM at 202 m CSF-A. The prominent kink in the alkalinity profile is the key to understanding much of the geochemistry at Site U1422. Notably, interstitial water samples from squeezers and Rhizons at similar depths had similar alkalinity (Fig. F25).

Ammonium increases gradually from below detection limit in the mudline sample to >3000 µM at 202 m CSF-A. The profile is slightly concave downward. Importantly, there is no inflection in the NH_4^+ concentration profile at ~30 m CSF-A, and the molar ratio of alkalinity to NH_4^+ is ~6:1 at ~200 m CSF-A.

Phosphate increases rapidly from 1.52 µM in the mudline sample to ~75 µM at 16 m CSF-A. The rise is greatest over the uppermost 5 m below the seafloor. Below a prominent peak at 16 m CSF-A, the PO_4^{3-} profile decreases gradually, with values <20 µM at 202 m CSF-A.

These profiles reflect a combination of several processes. As occurs at many locations, solid organic carbon with a generic Redfield composition of

$[(CH_2O)_{106}(NH_3)_{16}(H_3PO_4)]$ decomposes to release HCO_3^-, NH_4^+, and PO_4^{3-} (Froelich et al., 1979; Berner, 1980; Murray et al., 1992). Alkalinity often approximates HCO_3^- concentrations in the marine environment. Therefore, there are downhole increases in the three profiles that are somewhat similar to the Redfield ratio. However, both HCO_3^- and PO_4^{3-} can precipitate into (or onto) authigenic minerals, so their concentrations decrease with depth. Beyond the formation of authigenic carbonate phases (Matsumoto, 1992), previous work on deep-sea sediment sequences from the marginal sea has documented significant formation of francolite, a phosphate mineral (Föllmi et al., 1992). Manganese oxides and hydroxides in the upper 1 m below the seafloor may also concentrate P, which could be released to interstitial water as they dissolve with burial (Cha et al., 2005).

The classic explanation for the C-N-P profiles, however, neglects some basic observations. The alkalinity kink at ~35 m CSF-A indicates significant net generation of HCO_3^-, HS^-, or both across a thin horizon at this depth (it is important to note here that HS^- contributes to alkalinity [Gieskes and Rogers, 1973]). The lack of a prominent NH_4^+ inflection at ~35 m CSF-A further indicates that degradation of solid organic carbon does not produce the anomalous input of alkalinity at this depth. However, AOM is an obvious source for generating alkalinity in shallow-marine sediment (Borowski et al., 1996). This reaction can be expressed as (Reeburgh, 1976)

$$CH_{4(aq)} + SO_4^{2-}{}_{(aq)} \rightarrow HCO_3^-{}_{(aq)} + HS^-{}_{(aq)} + H_2O. \quad (1)$$

The significance of AOM to the geochemistry at Site U1422 becomes clearer below.

Volatile hydrocarbons

Two qualitative observations concerning gas are worth noting. We began to detect the odor of hydrogen sulfide with Core 346-U1422C-3H, and the odor disappeared deeper than Core 6H (as well as at corresponding depths in Holes U1422D and U1422E). Gas expansion cracks began forming between 50 and 60 m CSF-A, and major gas voids appeared in Core 346-U1422C-11H and several following cores.

Methane is, by far, the dominant hydrocarbon gas (>99.9%) in all HS samples from Site U1422 (Table T12). The same is true for the VAC gas samples taken (Table T13).

Methane concentrations in HS samples are nearly at the detection limit over the upper 30 m CSF-A. At approximately this depth, CH_4 values increase rapidly, reaching 3600 ppmv at 34.6 m CSF-A. Crucially, the rise in CH_4 occurs at the depth where the aforementioned inflection in pore water alkalinity occurs (Fig. F25). Deeper than 44.1 m CSF-A, CH_4 concentrations fluctuate between 16,600 and 40,300 ppmv to the bottom of the hole at 202 m CSF-A. Ethane concentrations range between 0 and 15.2 ppmv across all samples. The methane to ethane ratio generally exceeds 1200. No heavy hydrocarbons were detected. The near absence of higher molecular weight hydrocarbon gases strongly suggests that CH_4 at Site U1422 derives from microbially mediated methanogenesis, as opposed to thermogenesis, despite the very high geothermal gradient (see **"Downhole measurements"**).

As noted in **"Geochemistry"** in the "Methods" chapter (Tada et al., 2015b), HS sampling proceeded with a specific goal of quantifying CH_4 concentrations in interstitial water. A measured 3–5 cm^3 volume of wet sediment was placed into a saturated NaCl solution for HS analyses. When concentrations are normalized to wet sediment volumes, the CH_4 profile changes somewhat, but the main features remain (Fig. F26).

Modest amounts of CH_4 are generated via microbial activity at Site U1422. At depth and with hydrostatic pressure, CH_4 at in situ conditions is dissolved in pore water. However, during core recovery and handling, CH_4 escapes solution, resulting in gas cracks and voids in the sediment cores (Paull et al., 2000). Methane concentrations in HS gas samples deeper than ~50 m CSF-A are not meaningful because of degassing.

Within the sediment column, high CH_4 concentrations at depth lead to a concentration gradient and upward flux of CH_4. The upper segment of this gradient is observed between ~30 and 50 m CSF-A. At 30 m CSF-A, CH_4 rising from depth reacts with SO_4^{2-} diffusing down from the seafloor as a result of AOM (Equation 1), which results in a relatively thin SMT (Fig. F26).

One consequence of AOM is the generation of HS^- (Equation 1). The H_2S odor in Cores 346-U1422C-3H through 6H represents degassing of this AOM product. The smell occurs over a broad but well-defined depth horizon because HS^- diffuses both upward and downward from the SMT. The ends of these diffusion paths are where HS^- reacts with dissolved Fe.

Microbial methanogenesis of organic matter generates HCO_3^- and NH_4^+. As a consequence, alkalinity and NH_4^+ concentrations can become very high at sites with significant methanogenesis. Although NH_4^+ concentrations are fairly high at depth, alkalinity concentrations are not exceptional, giving rise to a low C:N ratio in pore water. This low ratio suggests

removal of HCO_3^- relative to NH_4^+ and may indicate authigenic carbonate precipitation at depth.

Yellowness

All interstitial water appeared visually clear, unlike waters at sites with significant methanogenesis in the upper few hundred meters below the seafloor (e.g., ODP Site 808 at the Nankai Trough [You et al., 1993], Site 1230 at the Peru margin [Shipboard Scientific Party, 2003a], and Site 1244 at the Hydrate Ridge [Shipboard Scientific Party, 2003b]). Thus, we thought Site U1422 might provide a good reference location to generate a background depth profile of color to compare to sites where interstitial water becomes yellow.

In contrast to expectations, interstitial water at Site U1422 exhibits an obvious color profile when examined for absorbance at 325 nm (Table T14). In a general sense, color tracks alkalinity (Fig. F27). However, the details are more complicated. First, the color increase with depth is slightly steeper and shallower than the rise in alkalinity. Second, absorbance scans of multiple interstitial water samples across a range of wavelengths shows that interstitial water "color" actually corresponds to a broad absorbance maximum with a center that can vary between ~270 and 290 nm.

Pore water at Site U1422 likely contains low but significant amounts of colored dissolved organic matter (CDOM), which is generated through the microbial decomposition of solid organic carbon. The composition and amount of this CDOM seems to change with depth.

Bromide

Although not typically examined during drilling expeditions, pore water Br^- concentration was measured at Site U1422 (Table T11). However, all values were between 0.85 and 0.98 mM, a range only slightly greater than the precision of Br^- analyses using the shipboard ion chromatograph (see "Geochemistry" in the "Methods" chapter [Tada et al., 2015b]). In any case, these values are slightly greater than the Br^- concentration of theoretical JSPW (0.84 mM) (see "Geochemistry" in the "Methods" chapter [Tada et al., 2015b]).

At sites with major methanogenesis, Br^- concentrations can exceed 2 mM (Martin et al., 1993; Egeberg and Dickens, 1999). This is because organic carbon landing on the seafloor incorporates Br^- from seawater and releases it to interstitial water upon degradation. The relatively low Br^- concentrations at Site U1422 are consistent with other indicators for only modest organic diagenesis.

Sulfate and barium

Sulfate is 29.3 mM in the mudline sample (Table T11), which is the value of reference seawater but greater than expected for theoretical JSPW (28.5 mM) (see "Geochemistry" in the "Methods" chapter [Tada et al., 2015b]). From the seafloor, SO_4^{2-} decreases to below detection at ~35 m CSF-A (Fig. F28A). The decrease is slightly concave downward but close to linear. Moreover, the depth where SO_4^{2-} drops below the detection limit is the same as that for the inflections in alkalinity and dissolved CH_4 (Fig. F26).

The Ba profile contrasts starkly with the SO_4^{2-} profile (Fig. F28). Interstitial water Ba concentrations are very low (<30 µM) from the seafloor to 20 m CSF-A. From this depth and for the next ~10 m downhole, Ba concentrations increase almost exponentially, surpassing 1200 µM by 35 m CSF-A. Values then increase with a concave-downward profile, such that Ba concentrations reach as high as 6000 µM near the bottom of the site.

The near-linearity of the SO_4^{2-} profile strongly suggests that, within the upper 35 m of sediment, net SO_4^{2-} removal dominantly occurs at the SMT. This suggestion is consistent with AOM being an important reaction at Site U1422. Beyond the aforementioned effects of AOM, the removal of SO_4^{2-} impacts the sedimentary Ba cycle (Dickens, 2001). Small grains of barite ($BaSO_4$) are a ubiquitous component of surface sediment deposited at intermediate to deepwater depths in the ocean (Dehairs et al., 1980). In sediment sections with even moderately depleted pore water SO_4^{2-}, solid barite is preserved because the barite equilibrium constant is extremely low. However, when pore water SO_4^{2-} concentrations approach zero, barite begins to dissolve (von Breymann et al., 1992):

$$BaSO_{4(s)} \rightarrow Ba^{2+}{}_{(aq)} + SO_4^{2-}{}_{(aq)}. \quad (2)$$

Consequently, at sites with significant amounts of CH_4 and AOM, sedimentary barite begins dissolving as it is buried through the SMT. This liberates Ba^{2+} to interstitial water at concentrations related to the equilibrium constant (Fig. F28B). Upward diffusion of dissolved Ba^{2+} can lead to a solid barite front, which has been found just above the SMT at multiple locations (von Breymann et al., 1992; Dickens, 2001) and might be expected at Site U1422.

The SO_4^{2-} and Ba profiles (Fig. F28A) further indicate a problem in sample collection. Below the SMT, SO_4^{2-} concentration should be zero. However, several samples between 120 and 170 m CSF-A have detectable SO_4^{2-} and anomalously low Ba concentrations, at

least compared to surrounding samples. The depth interval containing these samples has abundant gas voids. Such voids are drilled on the catwalk to release gas and are subsequently compressed to make a continuous sediment core. We think that some interstitial water samples were taken across intervals that were pressed together, so they have been contaminated with small amounts of drilling fluid (seawater) that induce barite precipitation.

Calcium, magnesium, and strontium

The Ca, Mg, and Sr profiles (Fig. F29) are somewhat similar to those at Site 795 (Shipboard Scientific Party, 1990) and at many locations where basalt lies within several hundred meters of the seafloor (Gieskes and Lawrence, 1981).

Calcium concentration is 10.1 mM in the mudline sample (Table T11), which is slightly lower than the value expected for theoretical JSPW (10.4 mM) (see "Geochemistry" in the "Methods" chapter [Tada et al., 2015b]). From the seafloor, values decrease to 6 mM at 35 m CSF-A. Calcium concentrations then increase steadily with depth, reaching 9.1 mM at 202 m CSF-A.

Magnesium concentration is 52.5 mM in the mudline sample, which is close to the value expected for theoretical JSPW (52.7 mM) (see "Geochemistry" in the "Methods" chapter [Tada et al., 2015b]). From the seafloor, values decrease to 41 mM at 10 m CSF-A. Magnesium concentrations then decrease steadily with depth, reaching 19 mM at 200 m CSF-A.

The Sr profile is somewhat erratic at Site U1422. Because other trace metal profiles are smooth, we suspect an issue measuring Sr on the ICP-AES. Nonetheless, Sr concentration is 93 µM in the mudline sample, which is close to the value expected for theoretical JSPW (see "Geochemistry" in the "Methods" chapter [Tada et al., 2015b]). The uppermost sample below the seafloor at 1.45 m CSF-A contains 82 µM Sr. From this depth, Sr values increase to 100 µM at 34 m CSF-A. Deeper than 34 m CSF-A, the Sr profile varies between 100 and 120 µM.

The Ca, Mg, and Sr profiles likely result from several processes. Almost certainly, the low in Ca across the SMT reflects the precipitation of carbonate:

$$HCO_3^- + Ca^{2+} \rightarrow CaCO_{3(s)} + H^+, \quad (3)$$

or

$$2HCO_3^- + Ca^{2+} + Mg^{2+} \rightarrow CaMg(CO_3)_{2(s)} + 2H^+. \quad (4)$$

Basically, HCO_3^- produced by AOM (Equation 1) reacts with Ca^{2+} diffusing from the seafloor and from deeper in the sedimentary column. At some locations, including those within the body of water between the Eurasian continent and the Japanese Islands, the loss of pore water Ca at the SMT coincides with the precipitation of calcite (Snyder et al., 2007); at other locations, the loss coincides with the occurrence of dolomite (Moore et al., 2004). Without detailed examination of the sediment and flux-based calculations, it is difficult to argue for a particular carbonate mineral, especially because the inflections in Ca and Mg do not align with respect to depth.

Although not obvious from operations at Site U1422 but clear from the geochemistry at Site 795, alteration of ash and basalt (at nominally 500 mbsf) drive the overall rise in Ca and drop in Mg with depth. Essentially, the Ca and Mg trends at 200 m CSF-A extend for another 300 m.

Salinity, chlorinity, sodium, and pH

Salinity decreases from 35 in the mudline sample to a minimum of 30 at 202 m CSF-A. The decrease in salinity is manifest in the Cl^- and Na concentration profiles, although the Cl^- values (Table T11) may be compromised at Site U1422 because of a faulty electrode during titration that was discovered after moving to Site U1423. Chloride and Na concentrations are 539 and 470 mM, respectively, in the mudline sample, which compare to 545 mM and 468 mM, respectively, in theoretical JSPW (see "Geochemistry" in the "Methods" chapter [Tada et al., 2015b]). Interstitial water concentrations of both elements drop rapidly over the upper 15 m below the seafloor and more slowly over the next 185 m.

pH varies between 7.5 and 8.0, with a mean of 7.7. This is consistent with interstitial water at many drill sites. There are no clear trends in pH, as values fluctuate over a relatively short distance. This lack of trend is true in Rhizon samples as well.

Interstitial water with relatively low salinity and dissolved Cl^- concentration was documented at Site 795. The initial drop in salinity beneath the seafloor was ascribed to loss of SO_4^{2-} (Shipboard Scientific Party, 1990). However, this is unlikely, as discussed more fully in "Geochemistry" in the "Site U1423" chapter (Tada et al., 2015c).

Potassium

Potassium concentration is ~10 mM in the mudline sample (Table T11). After an increase to 13 mM in the upper 10 m, K concentrations decrease steadily, reaching 8 mM at 202 m CSF-A. The rise in K immediately below the seafloor is intriguing and may reflect exchange during authigenic mineral formation. The decrease in K with depth perhaps results from further reactions with ash and basalt (Murray et al., 1992), although formation of glauconite would also

remove K^+ from interstitial water (Föllmi and von Breymann, 1992).

Lithium and boron

Lithium concentration (Fig. F30) is 28 µM in the mudline sample. Li values decrease to 20 µM at 11 m CSF-A (Table T11). Below this depth, Li concentrations increase to 108 µM at the bottom of Hole U1422C. Lithium concentrations in Rhizon samples are similar to those obtained by squeezing over the same interval.

Previous work at Site 795 suggests that the Li profile is dominated by biogenic silica recrystallization (Murray et al., 1992), although this was a speculative interpretation. Alteration of ash may also be an important process.

Boron concentration (Fig. F30) is 451 µM at the mudline and increases to 2637 µM at the bottom of Hole U1422C. Deeper than 25 m CSF-A, B concentrations increase more rapidly compared to shallower depths, suggesting that the SMT may affect B concentrations in interstitial water. We observed oscillations in concentrations from sample to sample. The samples were run on the ICP-AES in random order, and precision was calculated to be 0.4%, eliminating the idea that the oscillating trend below 25 m CSF-A is an artifact of instrumental analysis. We hypothesize that the oscillations are caused by variations in sample acquisition, such as squeezing or core flow.

Silica

Silica concentration in interstitial water at Site U1422 (Fig. F31) increases from an initial value of 84 µM in the bottom water (0 m CSF-A) to a maximum value of 1166 µM at 188 m CSF-A (Table T11). The opal-A/opal-CT boundary was not drilled at Site U1422, so the expected decrease in dissolved H_4SiO_4 at depth (Shipboard Scientific Party, 1990) was not observed. Notably, dissolved silica concentrations vary significantly over short distances, unlike the profiles for most other elements.

The profile of Si measured using the ICP-AES and the profile of H_4SiO_4 measured using the spectrophotometer match fairly well (Fig. F31). As the two sets of analyses were analyzed from independent aliquots, each of which involved further processing, any variability observed in the silica profiles is unlikely to have been caused by sample preparation or instrumental imprecision. The high degree of variability in the Si profile may reflect changing lithology, including diatomaceous sediment and turbidites in Unit II.

Summary

Geochemical profiles at Site U1422 are somewhat similar to those at nearby Site 795 (Shipboard Scientific Party, 1990). The major difference is that Site U1422 has much higher CH_4 concentrations. The high CH_4 concentrations at depth lead to an upward flux of CH_4 through the sediment column and AOM across a relatively shallow and thin SMT (~35 m CSF-A). In turn, this shallow zone of AOM impacts other species. The generation of HS^- leads to reactions with dissolved Fe, the generation of HCO_3^- leads to reactions with dissolved Ca, and the loss of SO_4^{2-} dissolves barite.

These detailed interstitial water profiles are amenable to numerical modeling during future shore-based studies. However, because the organic carbon input is highly variable, a full understanding of the system may require a nonsteady-state approach.

Furthermore, there is also an issue regarding alkalinity. As noted above, alkalinity approximates the sum of HCO_3^- and HS^-. In retrospect, had we predicted that a shallow SMT would be found at Site U1422, we could have measured dissolved inorganic carbon, HS^-, and total sulfur. This would enable the direct determination of the proportion of alkalinity caused by HCO_3^- and HS^-.

Paleomagnetism

Paleomagnetic samples and measurements

Paleomagnetic investigation for cores collected at Site U1422 included the measurement of magnetic susceptibility of whole-round and archive-half split-core sections and of natural remanent magnetization (NRM) of archive-half sections. NRM of all cores from Holes U1422A–U1422C and Cores 346-U1422D-1H through 3H was measured before and after alternating field (AF) demagnetization with a 20 mT peak field at every 5 cm interval. Because of increased core flow through the paleomagnetism station, NRM of Cores 346-U1422D-4H through 16H and of all cores from Hole U1422E was measured only after 20 mT AF demagnetization. The FlexIT core orientation tool (see **"Paleomagnetism"** in the "Methods" chapter [Tada et al., 2015b]) was successfully deployed to orient 13 APC-collected cores in Hole U1422C, starting from Core 346-U1422C-2H. Core orientation data collected in Hole U1422C are reported in Table T15.

We collected one paleomagnetic discrete cube sample (see **"Paleomagnetism"** in the "Methods" chap-

ter [Tada et al., 2015b]) from the first section of each core in Hole U1422C and occasionally from deep sections when the first section was not suitable for taking a discrete sample. Depth levels where discrete samples were taken are marked by triangles along the left side of the paleomagnetic inclination data column in Figure **F32C.** Stepwise AF demagnetization of 12 discrete samples from Hole U1422C was performed at successive peak fields of 0, 5, 10, 15, 20, 25, 30, 35, 40, 45, 50, 55, 60, 70, and 80 mT to verify the reliability of the split-core measurements and to determine the demagnetization behavior of the recovered sediment. Depth levels where the measured discrete samples were collected are marked as orange triangles along the inclination data column in Figure **F32C.** Following each demagnetization step, NRM of the discrete samples was usually measured with the sample placed in three different orientations on the discrete sample tray (i.e., "away-up," "top-right," and "top-toward"; see **"Paleomagnetism"** in the "Methods" chapter [Tada et al., 2015b]) and then averaged to acquire statistically more reliable results. Because of increased core flow, we sometimes only performed stepwise AF demagnetization up to 60 mT peak field and measured the samples in only one orientation (top-toward).

We processed data extracted from the shipboard Laboratory Information Management System (LIMS) database by removing all measurements collected from disturbed and void intervals and all measurements that were taken within 10 cm of the section ends, which are slightly biased by measurement edge effects. A modified version of the UPmag software (Xuan and Channell, 2009) was used to analyze the NRM data of both the split-core section and the discrete cube samples. The disturbed and void intervals used in this process are reported in Table **T16.** The processed NRM inclination, declination, and intensity data after 20 mT AF demagnetization are reported in Table **T17** and shown in Figure **F32.**

Natural remanent magnetization and magnetic susceptibility

NRM intensity after 20 mT AF demagnetization in all five holes is similar in magnitude for overlapping intervals, mostly ranging between ~10^{-5} and 10^{-2} A/m. For core sections from the uppermost ~7 m, NRM intensity is on the order of 10^{-2} A/m. NRM intensity gradually decreases downcore to the order of 10^{-4} to 10^{-3} A/m between ~7 and ~35 m CSF-A. NRM intensity appears to highly fluctuate between 10^{-5} and 10^{-3} A/m from ~40 to ~80 m CSF-A and is mostly on the order of 10^{-4} A/m from ~80 to ~140 m CSF-A. Between ~140 and ~205 m CSF-A in Hole U1422C, NRM intensity is on the order of 10^{-4} to 10^{-3} A/m.

The AF demagnetization behavior of eight discrete samples from normal and reversed polarity intervals at varying depths is illustrated in Figure **F33.** All samples exhibit a steep, normal overprint that was generally removed after AF demagnetization at peak fields of ~15–20 mT, demonstrating that the 20 mT AF demagnetization is, in general, sufficient to eliminate the overprint. For measured discrete samples from below ~20 m CSF-A, NRM intensities before and after stepwise demagnetizations are generally one or two magnitudes lower than those from above this level. NRM measurement of discrete samples from deep depths (deeper than ~30 m CSF-A) often appears to be significantly affected by an anhysteretic remanent magnetization, possibly acquired because of bias caused by ambient magnetic field during AF demagnetization.

Magnetic susceptibility measurements were taken on whole cores from all five holes as part of the Whole-Round Multisensor Logger (WRMSL) analysis and on archive-half sections using the Section Half Multisensor Logger (SHMSL) (see **"Physical properties"**). WRMSL-acquired susceptibility was stored in the database in raw meter units. These were multiplied by a factor of 0.68×10^{-5} to convert to the dimensionless volume SI unit (Blum, 1997). A factor of $(67/80) \times 10^{-5}$ was multiplied by the SHMSL-acquired susceptibility stored in the database. Magnetic susceptibility measurement is consistent between the two instruments and, in general, mimics NRM intensity, suggesting that the magnetic minerals that carry NRM are the same or at least coexist with those that dominate magnetic susceptibility. Magnetic susceptibility varies between 10×10^{-5} and 50×10^{-5} SI for sediment from the uppermost ~7–10 m of the holes and is generally $<10 \times 10^{-5}$ SI for sediment from below 7–10 m CSF-A (Fig. **F32,** fourth panel).

Magnetostratigraphy

In spite of the drill string overprint and generally low NRM intensity, paleomagnetic inclination and declination data of the holes appear to show patterns that allow for determination of magnetic polarity for at least the uppermost ~80 m of recovered sediment. Both magnetic declination and inclination after 20 mT AF demagnetization were used when possible for magnetostratigraphic interpretation at this site. The geomagnetic field at the latitude of Site U1422 (43.77°N) has an expected inclination of 62.44°, assuming a geocentric axial dipole field model, which is sufficiently steep to determine magnetic polarity

in APC cores that lack horizontal orientation. We identified the Brunhes/Matuyama boundary (0.781 Ma) and the Jaramillo (0.988–1.072 Ma) and Olduvai (1.778–1.945 Ma) Subchrons at Site U1422 (Table T18).

Inclinations of the two APC cores (~10 m long) recovered in Holes U1422A and U1422B vary closely around the expected positive inclination at the site location (Fig. F32A, F32B), suggesting the uppermost ~10 m of sediment from the two holes was deposited during the Brunhes Chron. The Brunhes/Matuyama boundary was identified at ~33.5 m CSF-A in Hole U1422C, ~32.3 m CSF-A in Hole U1422D, and ~32.5 m CSF-A in Hole U1422E. Inclination values above the identified boundary vary around the expected dipole inclination value of ~62.44°. In Hole U1422C, the FlexIT-corrected declination shows values mostly around 0°, which is expected for a normal polarity at the site for the uppermost ~33.5 m. This interpretation is consistent with the FO of calcareous nannofossil *E. huxleyi* (0.29 Ma) at 19.87–24.19 m CSF-A in Hole U1422C (see "Biostratigraphy").

The second significant inclination pattern change was observed at ~77.5 m CSF-A in Hole U1422C, ~82.5 m CSF-A in Hole U1422D, and ~76.8 m CSF-A in Hole U1422E. In Hole U1422C, this inclination pattern change is accompanied by FlexIT-corrected declination values changing from an average of ~180° to ~0°. We interpret this horizon as the top of the Olduvai Chron (C2n, 1.778 Ma). In Hole U1422C, where FlexIT tool orientation data are available, the corrected declination appears to change from an average of ~0° back to an average of ~180° at ~84.6 m CSF-A. As declination is less affected by the generally vertical drilling overprints, this could be interpreted as the bottom of the Olduvai Subchron (C2n, 1.945 Ma) recorded in Hole U1422C. These interpretations are consistent with the lithologic Unit I/II boundary (with an age of ~2.5 Ma; Tada, 1994) (see "Lithostratigraphy") recognized at 90.52 m CSF-A in Hole U1422C, 89.71 m CSF-A in Hole U1422D, and 90.30 m CSF-A in Hole U1422E.

Between the Brunhes/Matuyama boundary and the top of the Olduvai Chron, a short interval with relatively stable positive inclinations around the expected dipole inclination value are identified between ~41.5 and 45.2 m CSF-A in Hole U1422C, ~41 and 45.6 m CSF-A in Hole U1422D, and ~41.8 and 45.7 m CSF-A in Hole U1422E. In Hole U1422C, FlexIT-corrected declinations also appear to vary mostly around 0°. We interpret this interval as the Jaramillo Subchron (0.988–1.072 Ma). Postcruise studies are needed to further refine the depth levels of these identified boundaries.

Below the interpreted bottom of the Olduvai Chron in Hole U1422C and top of the Olduvai Chron in Holes U1422D and U1422E, inclinations show mostly positive values that are apparently steeper than the expected dipole inclination, indicating drill string overprinting that may not have been efficiently removed. Strong overprint and the lack of orientation for the bottom cores, as well as the large scatter in declination makes it difficult for any reliable magnetostratigraphic interpretations.

Physical properties

Physical properties at Site U1422 were expected to be highly variable based on previous results at Site 795 (Shipboard Scientific Party, 1990), reflecting variable lithologies (with organic-rich to various types of hemipelagic sediment, including dust and ice-rafted material) and accompanying diagenetic processes. To this expected variability, Site U1422 added another layer of complexity: the presence of turbidites with variable composition in the lower part of the drilled sequence. Physical properties at Site U1422 were measured on whole- and split-core sections and discrete samples to describe this complexity, as per the strategy outlined in "Physical properties" in the "Methods" chapter (Tada et al., 2015b). Modifications to that plan are addressed herein.

The Special Task Multisensor Logger (STMSL), which measures gamma ray attenuation (GRA) bulk density and magnetic susceptibility, was used for stratigraphic correlation purposes immediately after core recovery at a scanning interval of 5 cm. The WRMSL, which measures GRA bulk density, magnetic susceptibility, and compressional wave velocity, was used at high resolution (2.5 cm) after the cores reached room temperature. Thermal conductivity (one per core) and NGR measurements (eight per full section) completed the suite of whole-core measurements. Compressional wave velocity measurements on split cores were attempted in Hole U1422A (one per core) and subsequently abandoned because of poor results. Shear stress measurements (one per core) were taken in Hole U1422A with more success. Spectral diffuse reflectance (mostly 1 cm intervals) and point magnetic susceptibility (mostly 2 cm intervals) were measured on the SHMSL. Moisture and density (MAD) analyses were undertaken on discrete core samples (2–3 per core) in Hole U1422A. Physical properties measurements are presented in Figures F34, F35, and F36; because a majority of the physical

properties are driven by lithology, there was no need to define units independent of the lithologic units.

Thermal conductivity

Thermal conductivity was measured once per core using the full-space probe, usually near the middle of Section 4. Thermal conductivity in fine-grained sediment is, as a first approximation, a linear combination of the conductivities of the sedimentary grains and the interstitial water and therefore depends upon porosity, water content, and lithology (Hyndman et al., 1974). Overall, thermal conductivity values range from 0.7 to 1.0 W/(m·K) without a clear increase with depth.

Moisture and density

GRA bulk sediment density at Site U1422 displays no clear trend with depth but strong high-frequency variability (i.e., decimeter- to multimeter-scale) within a general range between 1.2 and 1.8 g/cm^3 (Fig. **F34**). Discrete wet bulk density agrees well with the primary trends in GRA bulk density and has similar values (Fig. **F35**). In lithologic Unit I, variability in GRA bulk density appears to come from the occurrence of massive very dark layers (characterized by low L* values) exhibiting lower bulk density than the rest of the sediment (Fig. **F36**). This relationship was confirmed at Site U1425 (see Fig. **F57** in the "Site U1425" chapter [Tada et al. 2015d]). The cyclical variability seen in GRA bulk density breaks down in Unit II, although the strong variability is still present but with a higher scatter. The region of high scatter located deeper than ~125 m CSF-A (see the **"Methods"** chapter [Tada et al., 2015b]) coincides with degraded core quality (e.g., microfractures) responsible for low-density readings, whereas the turbidite-rich sequence in Unit II may explain high-density values. Density readings in this sequence reach nearly 1.8 g/cm^3 more often than in the sediment above it, probably because of increased terrigenous clastics in certain intervals. With the exception of grain density, most other MAD-derived parameters (i.e., porosity and water content) show no trends downhole. The increase in grain density downhole may be explained by the occurrence of terrigenous-rich turbidites.

Magnetic susceptibility

Whole-core magnetic susceptibility measured on the STMSL immediately after recovery closely tracks WRMSL susceptibility measured on cores that were equilibrated to room temperature (Fig. **F34**), confirming that sediment temperature does not affect this bulk parameter at this site. Similarly, point magnetic susceptibility (SHMSL) tracks whole-core trends well (Fig. **F34**), but values are significantly higher than the whole-core equivalents because of the inherent smoothing imposed by the magnetic susceptibility loop, which lowers whole-core intensities. Although mean values stay between 10×10^{-5} and 20×10^{-5} SI for the site, the highest magnetic susceptibility readings occur above ~20 m CSF-A but below the oxic zone at the mudline (i.e., the red–dark brown zone containing iron oxyhydroxides at ~0–50 cm CSF-A) (e.g., Lyle, 1983). A magnetic susceptibility maximum occurs between 2 and 6 m CSF-A where values up to 200×10^{-5} SI were measured. Because no apparent primary lithology corresponds to this region, it is likely that the strong intensities are due to highly magnetic authigenic mineral formation. As no visible signs of monosulfides are evident in freshly split cores, ferrimagnetic greigite is probably not the likely cause, but formation and survival of authigenic magnetite grains beyond the oxic zone may be an alternative explanation. Furthermore, there is no evident correlation between magnetic susceptibility and decimeter-scale lithology, which also suggests diagenetic influence in lowering of the signal between ~6 and 20 m CSF-A near the SMT zone with the signal severely muted after that. However, there is an increase in mean and upper range values in the turbidite-rich sequence below ~140 m CSF-A.

Natural gamma radiation

Total NGR counts show strong cyclicity in Unit I that imparts a decreasing trend in counts with depth (Fig. **F34**). NGR counts range from 20 to 80 cps in Unit I and fall to between 20 and 40 cps in Unit II. Inspection of the NGR spectra shows that U-series radionuclides are likely to be the largest contributors to the total NGR counts, as has been observed elsewhere with this same instrument (Vasiliev et al., 2011). Therefore, the variability in NGR may be explained by increased U associated to massive organic-rich layers in Unit I (Fig. **F36**). The multimeter-scale NGR cyclicity observed in Unit I closely follows the cycles in GRA bulk density. This correlation between NGR and GRA bulk density adds some confidence in interpreting the NGR data, which is collected at an interval greater than the thickness of the dark layers. With the disappearance of dark layers in Unit II, NGR counts decrease to background levels typical for clay or even lower because of the abundance of the biosiliceous component.

Compressional wave velocity

The WRMSL was used to measure compressional wave velocity and an attempt was made to collect

equivalent *P*-wave velocities on split cores (Fig. F34). Because of poor sediment to liner coupling, results from the WRMSL could only be obtained for the upper ~60 m CSF-A (Subunit IA). Even here some velocities are 100 m/s lower than the average, also suggesting the influence of small cracks in the relatively brittle sediment. Good data in this interval of *P*-wave velocity fluctuate at ~1500 m/s. A clear maximum occurs only in the soft, wet sediment of the uppermost ~2 m. Few good measurements could be collected with the gantry. The formation of small cracks at the numerous and sharp lithologic changes and within lithologic packets themselves might have negatively affected signal propagation through the sediment. Where collected, minor but clear differences between whole-core and split-core measurements possibly reflect the presence of water in the space between the core liner and sediment in the whole cores and the slight compaction of the sediment in the contact probe technique.

Vane shear stress

Undrained shear strength generally increases with depth through all lithologic units, reaching a maximum value of 88.6 kPa (Fig. F35). Measured values, however, are erratic due to small cracks in sediment throughout.

Diffuse reflectance spectroscopy

Color reflectance data measured on the split archive-half sections show high variability, especially in Unit I, reflecting the variegated colors of the decimeter- to centimeter-scale lithologic packages (Fig. F37). Unit I is generally characterized by high variability in lightness (L*), red-green ratio (a*), and yellow-blue ratio (b*), as very dark brown to black organic-rich bands occur here often and alternate with lighter olive and green hemipelagic sediment. Subunit IA can be clearly distinguished from Subunit IB by b* variability expressing a change in frequency of occurrence of the dark layers. As the dark bands disappear altogether in Unit II, L* and a* vary less to the bottom of the hole. However, the variability in color between different types of turbidites as well as hemipelagic packages in the lower part of Unit II keeps b* highly variable. The presence of dark green bands throughout the site suggests that Fe^{2+} is present in the mineral phase (clay?) accumulating in green fronts (Giosan, 2001). Shore-based analyses will further examine this hypothesis.

Summary

Physical properties at Site U1422 are highly variable, reflecting various lithologies and accompanying diagenetic processes. In Unit I, cyclical variability in density and NGR appears to be driven by the occurrence of thick, massive organic-rich dark layers, whereas in Unit II the more subdued variability is largely due to terrigenous clastics from turbidites and biogenic silica from diatoms. Magnetic susceptibility is strongly influenced by redox processes with severe muting of the signal below the SMT zone (see **"Geochemistry"**). *P*-wave and shear stress data collection was strongly affected by degassing, leading to microfractures in the core. Reflectance data quantify the variegated colors of the diverse lithologic packages at this site and provide the opportunity for the decimeter- to centimeter-scale correlation for Unit I between this and future sites.

Downhole measurements

In situ temperature and heat flow

APCT-3 downhole temperature measurements were performed in Hole U1422C at five depths, including the mudline. In situ temperatures range from 4.80°C at 33.1 m CSF-A to 15.86°C at 115.8 m CSF-A (Table T19), with a linear downhole increase indicating that the gradient is uniform with depth (Fig. F38). A linear fit of temperature versus depth gives a geothermal gradient of 134°C/km, slightly higher than the one measured during Leg 127 at Site 795 (132°C/km) (Langseth and Tamaki, 1992). The bottom water temperature at this site is estimated to be 0.35°C, based on the average mudline temperature in the four APCT-3 measurements. This low value is in good agreement with the expected temperature as most of the water column in the marginal sea is filled with cold water (<1°C).

Thermal conductivity under in situ conditions was estimated from laboratory-determined thermal conductivity using the method of Hyndman et al. (1974) (see **"Physical properties"** in the "Methods" chapter [Tada et al., 2015b]). The calculated in situ values are as much as 2.6% below the measured laboratory values. Thermal resistance was then calculated by cumulatively adding the inverse of the in situ thermal conductivity values over depth intervals downhole (Fig. F38). A heat flow of 120 mW/m² was obtained from the slope of the linear fit between in situ temperature and in situ thermal resistance (Pribnow et al., 2000). This value is 6% higher than the one cal-

culated at Site 795 (113 mW/m^2) (Langseth and Tamaki, 1992).

Stratigraphic correlation and sedimentation rates

A composite section and splice (as defined in **"Stratigraphic correlation and sedimentation rates"** in the "Methods" chapter [Tada et al., 2015b]) were constructed for Site U1422 in an effort to establish a continuous sediment sequence. Only one core each was recovered from Holes U1422A and U1422B. Hole U1422C was cored to APC refusal, which occurred at 205.2 m CSF-A at the base of Core 346-U1422C-31H. Cores 346-U1422C-15H through 31H were cored using the half APC coring system, which uses a 4.7 m long core barrel. Holes U1422D and U1422E were cored using the standard APC system to refusal at 141.8 (base of Core 346-U1422D-16H) and 111.6 m CSF-A (base of Core 346-U1422E-14H), respectively. Splicing among these holes enabled us to construct a continuous stratigraphic sequence from the seafloor to the bottom of Core 346-U1422C-18H (144.1 m CSF-A), with the exception of two gaps. Deeper than 144.4 m CSF-A, only sediment from Hole U1422C was recovered.

Construction of CCSF-A scale

Definition of top (0 m CCSF-A)

Holes U1422C and U1422D both recovered the mudline. We selected the longer Core 346-U1422D-1H as the anchor core and defined the top as 0 m CCSF-A (as defined in **"Stratigraphic correlation and sedimentation rates"** in the "Methods" chapter [Tada et al., 2015b]).

Compositing of cores

The CCSF-A scale for Site U1422 is based on the correlation of magnetic susceptibility and GRA data from the WRMSL, as well as RGB blue (B) data extracted from images acquired by the Section Half Imaging Logger (see **"Physical properties"** in the "Methods" chapter [Tada et al., 2015b]). Magnetic susceptibility and GRA bulk density were measured at 2.5 cm intervals, whereas B was calculated at 0.5 cm intervals.

Correlative horizons are most easily identified in the magnetic susceptibility and B data (Fig. **F39**). Extremely fine scale correlations are best achieved using the 0.5 cm B data at this site. The depth offsets used to create the CCSF-A scale are given in the affine table (Table **T20**).

An ~5 m section within Hole U1422D was replicated as the result of raising the bit between APC strokes at Cores 346-U1422D-1H and 2H, likely resulting in recovery of the borehole sidewall. As a result, interval 346-U1422D-1H-3, 44 cm (3.44 m CSF-A), to 1H-6, 45 cm (7.95 m CSF-A), is equivalent to interval 346-U1422D-2H-1, 0 cm (8.1 m CSF-A), to 2H-4, 40 cm (13 m CSF-A).

Core gaps

Partial strokes of the standard APC occurred at 77.8 and 78.3 m CSF-A during coring of Cores 346-U1422C-9H and 346-U1422D-9H, respectively, which prevented full recovery at these depths. The third attempt, using the half APC in Hole U1422E, recovered only disturbed sediment in Core 346-U1422E-9H, which includes flow-in structure below 1.8 m. Because the top 0.95 m of Core 346-U1422D-10H and the bottom 3 m of Core 346-U1422E-9H were disturbed with fall-in and flow-in, respectively, at least 0.95 m of sediment below ~84 m CCSF-A was not recovered (Table **T20;** Fig. **F40B**).

Drilling disturbance (flow-in) in Core 346-U1422D-13H at 113.3 m CSF-A and APC refusal of Core 346-U1422E-14H at 111.6 m CSF-A, as well as its poor recovery, prevents us from estimating the size of the core gap between Cores 346-U1422C-12H and 13H at 106.3 m CSF-A (Table **T20;** Fig. **F40C**).

Hole U1422C was the only hole at this site drilled deeper than 144.1 m CSF-A (bottom of Core 346-U1422C-18H). Because this site was not logged, no composite depth could be established for the interval from Cores 346-U1422C-19H through 31H (Fig. **F40C, F40D**).

Summary

Based on two core gaps and single hole coring of the interval from Cores 346-U1422C-19H through 31H, the CCSF-A scale given to Site U1422 cores is divided into four segments (Table **T20;** Fig. **F40**):

- Segment 1 consists of Cores 346-U1422A-1H, 346-U1422B-1H, 346-U1422C-1H through 9H, 346-U1422D-1H through 9H, and 346-U1422E-1H through 9H and extends from 0 to ~84 m CCSF-A.
- Segment 2 consists of Cores 346-U1422C-10H through 12H, 346-U1422D-10H through 12H, and 346-U1422E-10H through 13H and extends from ~84 to ~116 m CCSF-A.
- Segment 3 consists of Cores 346-U1422C-13H through 18H, 346-U1422D-13H through 16H, and 346-U1422E-14H and extends from ~115 to ~156 m CCSF-A.

- Segment 4 consists of Cores 346-U1422C-19H through 31H and extends from ~156 to 217 m CCSF-A.

Construction of CCSF-D scale

As for Segments 1 and 2, either a combination of Holes U1422C and U1422D or of Holes U1422D and U1422E covered all the stratigraphic intervals of each segment independently. In order to avoid whole-round sampling intervals and minimize inclusion of disturbed intervals, we selected Holes U1422D and U1422E to construct the primary splice for Segments 1 and 2. However, a flow-in disturbance in Core 346-U1422D-7H was aligned to the core gaps between Cores 346-U1422E-6H and 346-U1422E-7H, which forces us to use Core 346-U1422C-7H for this interval (Table **T21**). The splice for Segment 3 is constructed from Holes U1422C and U1422D, and the spice intervals are listed in Table **T22.** A splice for Segment 4 cannot be constructed and the depth scale is only provided as CCSF-A, assuming the same offset to all the cores from Cores 346-U1422C-19H through 31H (Table **T20**).

Sedimentation rates

Sedimentation rates at Site U1422 were estimated based on datums provided in biostratigraphy and paleomagnetism (see **"Biostratigraphy"** and **"Paleomagnetism"**). In order to integrate the data taken from Holes U1422C–U1422E, the composite depth scale (CCSF-A) was used here. Datums used in the estimation of sedimentation rates are plotted on Figure **F41A** and listed in Table **T22.**

Paleomagnetic datums constrained the sediment ages well for the lower part of Subunit IA and Subunit IB. Between 19.9 and 23.7 m CCSF-A, the lower and upper limits defined by the LO of *Spongodiscus* sp. and the FO of *E. huxleyi* narrow a possible range of depth-age relationships, which was selected as an inflection point (Table **T22**). Between 158.3 and 163.0 m CCSF-A, the lower and upper limits defined by the LO of *N. kamtschatica* and the FO of *C. davisiana* narrow a possible range of depth-age relationships, which was selected as a tie point of depth-age lines in Unit II. Thus, the most likely depth-age relation was determined, which also gave the ages of lithologic unit boundaries such as 1.4 and 2.1 Ma for the Subunit IA/IB and Subunit IB/Unit II boundaries, respectively.

Assuming constant sedimentation rates between selected tie points of depth-age lines, the calculated sedimentation rate of Site U1422 ranges from 32.0 to 95.7 m/m.y. (lower to moderate in Unit I and higher in Unit II) (Fig. **F41B**). The higher sedimentation rate in Unit II may result from the frequent turbidite layers. A slightly lower GRA density in Unit II also suggests relatively higher diatom content during these periods. Higher diatom flux may also contribute to the higher sedimentation rate in Unit II (see **"Lithostratigraphy"** and **"Biostratigraphy"**).

References

Berner, R.A., 1980. *Early Diagenesis: A Theoretical Approach:* Princeton, NJ (Princeton Univ. Press).

Blum, P., 1997. Physical properties handbook: a guide to the shipboard measurement of physical properties of deep-sea cores. *ODP Tech. Note,* 26. **doi:10.2973/odp.tn.26.1997**

Borowski, W.S., Paull, C.K., and Ussler, W., III, 1996. Marine pore-water sulfate profiles indicate in situ methane flux from underlying gas hydrate. *Geology,* 24(7):655–658. **doi:10.1130/0091-7613(1996)024<0655:MPWSPI>2.3.CO;2**

Brunner, C.A., 1992. Paleoenvironment and biostratigraphy of foraminifers at Sites 794, 795, 796, and 797 in the Japan Sea. *In* Pisciotto, K.A., Ingle, J.C., Jr., von Breymann, M.T., Barron, J., et al., *Proc. ODP, Sci. Results,* 127/128 (Pt. 1): College Station, TX (Ocean Drilling Program), 187–224. **doi:10.2973/odp.proc.sr.127128-1.124.1992**

Casey, R.E., 1977. The ecology and distribution of recent Radiolaria. *In* Ramsay, A.T.S. (Ed.), *Oceanic Micropaleontology* (Vol. 2): London (Academic Press), 806–845.

Cha, H.J., Lee, C.B., Kim, B.S., Choi, M.S., and Ruttenberg, K.C., 2005. Early diagenetic redistribution and burial of phosphorus in the sediments of the southwestern East Sea (Japan Sea). *Mar. Geol.,* 216(3):127–143. **doi:10.1016/j.margeo.2005.02.001**

Dehairs, F., Chesselet, R., and Jedwab, J., 1980. Discrete suspended particles of barite and the barium cycle in the open ocean. *Earth Planet. Sci. Lett.,* 49(2):528–550. **doi:10.1016/0012-821X(80)90094-1**

Dickens, G.R., 2001. Sulfate profiles and barium fronts in sediment on the Blake Ridge: present and past methane fluxes through a large gas hydrate reservoir. *Geochim. Cosmochim. Acta,* 65(4):529–543. **doi:10.1016/S0016-7037(00)00556-1**

Egeberg, P.K., and Dickens, G.R., 1999. Thermodynamic and pore water halogen constraints on gas hydrate distribution at ODP Site 997 (Blake Ridge). *Chem. Geol.,* 153(1–4):53–79. **doi:10.1016/S0009-2541(98)00152-1**

Föllmi, K.B., Cramp, A., Föllmi, K.E., Alexandrovich, J.M., Brunner, C., Burckle, L.H., Casey, M., deMenocal, P., Dunbar, R.B., Grimm, K.A., Holler, P., Ingle, J.C., Jr., Kheradyar, T., McEvoy, J., Nobes, D.C., Stein, R., Tada, R., von Breymann, M.T., and White, L.D., 1992. Dark–light rhythms in the sediments of the Japan Sea: preliminary results from Site 798, with some additional results from Sites 797 and 799. *In* Pisciotto, K.A., Ingle, J.C., Jr., von Breymann, M.T., Barron, J., et al., *Proc. ODP, Sci. Results,* 127/128 (Pt. 1): College Station, TX (Ocean

Drilling Program), 559–576. doi:10.2973/odp.proc.sr.127128-1.159.1992

Föllmi, K.B., and von Breymann, M., 1992. Phosphates and glauconites of Sites 798 and 799. *In* Pisciotto, K.A., Ingle, J.C., Jr., von Breymann, M.T., Barron, J., et al., *Proc. ODP, Sci. Results,* 127/128 (Pt. 1): College Station, TX (Ocean Drilling Program), 63–74. doi:10.2973/odp.proc.sr.127128-1.116.1992

Froelich, P.N., Klinkhammer, G.P., Bender, M.L., Luedtke, N.A., Heath, G.R., Cullen, D., Dauphin, P., Hammond, D., Hartman, B., and Maynard, V., 1979. Early oxidation of organic matter in pelagic sediments of the eastern equatorial Atlantic: suboxic diagenesis. *Geochim. Cosmochim. Acta,* 43(7):1075–1090. doi:10.1016/0016-7037(79)90095-4

Gieskes, J.M., and Lawrence, J.R., 1981. Alteration of volcanic matter in deep-sea sediments: evidence from the chemical composition of interstitial waters from deep sea drilling cores. *Geochim. Cosmochim. Acta,* 45(10):1687–1703. doi:10.1016/0016-7037(81)90004-1

Gieskes, J.M., and Rogers, W.C., 1973. Alkalinity determination in interstitial waters of marine sediments. *J. Sediment. Petrol.,* 43(1):272–277. doi:10.1306/74D72743-2B21-11D7-8648000102C1865D

Giosan, L., 2001. The use of sediment color in paleoceanography: Pliocene–Pleistocene sedimentation in the western North Atlantic [Ph.D. dissert.]. State Univ. of New York, Stony Brook, NY.

Hyndman, R.D., Erickson, A.J., and Von Herzen, R.P., 1974. Geothermal measurements on DSDP Leg 26. *In* Davies, T.A., Luyendyk, B.P., et al., *Init. Repts. DSDP,* 26: Washington, DC (U.S. Govt. Printing Office), 451–463. doi:10.2973/dsdp.proc.26.113.1974

Ikehara, K., 2003. Late Quaternary seasonal sea-ice history of the northeastern Japan Sea. *J. Oceanogr.,* 59(5):585–593. doi:10.1023/B:JOCE.0000009588.49944.3d

Itaki, T., Komatsu, N., and Motoyama, I., 2007. Orbital- and millennial-scale changes of radiolarian assemblages during the last 220 kyrs in the Japan Sea. *Palaeogeogr., Palaeoclimatol., Palaeoecol.,* 247(1–2):115–130. doi:10.1016/j.palaeo.2006.11.025

Kato, M., 1992. Benthic foraminifers from the Japan Sea: Leg 128. *In* Pisciotto, K.A., Ingle, J.C., Jr., von Breymann, M.T., Barron, J., et al., *Proc. ODP, Sci. Results,* 127/128 (Pt. 1): College Station, TX (Ocean Drilling Program), 365–392. doi:10.2973/odp.proc.sr.127128-1.142.1992

Koizumi, I., 1992. Diatom biostratigraphy of the Japan Sea: Leg 127. *In* Pisciotto, K.A., Ingle, J.C., Jr., von Breymann, M.T., Barron, J., et al., *Proc. ODP, Sci. Results,* 127/128 (Pt. 1): College Station, TX (Ocean Drilling Program), 249–289. doi:10.2973/odp.proc.sr.127128-1.127.1992

Langseth, M.G., and Tamaki, K., 1992. Geothermal measurements: thermal evolution of the Japan Sea basins and sediments. *In* Tamaki, K., Suyehiro, K., Allan, J., McWilliams, M., et al., *Proc. ODP, Sci. Results,* 127/128 (Pt. 2): College Station, TX (Ocean Drilling Program), 1297–1309. doi:10.2973/odp.proc.sr.127128-2.227.1992

Lyle, M., 1983. The brown-green color transition in marine sediments: a marker of the Fe(III)-Fe(II) redox boundary. *Limnol. Oceanogr.,* 28(5):1026–1033. doi:10.4319/lo.1983.28.5.1026

Maiya, S., 1978. Late Cenozoic planktonic foraminiferal biostratigraphy of the oil-field region of northeast Japan. In *Cenozoic Geology of Japan,* Osaka, 35–60. (in Japanese, with abstract in English)

Martin, J.B., Gieskes, J.M., Torres, M., and Kastner, M., 1993. Bromide and iodine in Peru margin sediments and pore fluids: implication for fluid origins. *Geochim. Cosmochim. Acta,* 57(18):4377–4389. doi:10.1016/0016-7037(93)90489-J

Matsumoto, R., 1992. Diagenetic dolomite, calcite, rhodochrosite, magnesite, and lansfordite from Site 799, Japan Sea—implications for depositional environments and the diagenesis of organic-rich sediments. *In* Pisciotto, K.A., Ingle, J.C., Jr., von Breymann, M.T., Barron, J., et al., *Proc. ODP, Sci. Results,* 127/128 (Pt. 1): College Station, TX (Ocean Drilling Program), 75–98. doi:10.2973/odp.proc.sr.127128-1.119.1992

Moore, T.S., Murray, R.W., Kurtz, A.C., and Schrag, D.P., 2004. Anaerobic methane oxidation and the formation of dolomite. *Earth Planet. Sci. Lett.,* 229(1–2):141–154. doi:10.1016/j.epsl.2004.10.015

Motoyama, I., and Nishimura, A., 2005. Distribution of radiolarians in North Pacific surface sediments along the 175°E meridian. *Paleontol. Res.,* 9(2):95–117. doi:10.2517/prpsj.9.95

Murray, R.W., Brumsack, H.J., von Breymann, M.T., Sturz, A.A., Dunbar, R.B., and Gieskes, J.M., 1992. Diagenetic reactions in deeply buried sediments of the Japan Sea: a synthesis of interstitial water chemistry results from Legs 127 and 128. *In* Tamaki, K., Suyehiro, K., Allan, J., McWilliams, M., et al., *Proc. ODP, Sci. Results,* 127/128 (Pt. 2): College Station, TX (Ocean Drilling Program), 1261–1274. doi:10.2973/odp.proc.sr.127128-2.177.1992

Nobes, D.C., Murray, R.W., Kuramoto, S., Pisciotto, K.A., and Holler, P., 1992. Impact of silica diagenesis on physical property variations. *In* Pisciotto, K.A., Ingle, J.C., Jr., von Breymann, M.T., Barron, J., et al., *Proc. ODP, Sci. Results,* 127/128 (Pt. 1): College Station, TX (Ocean Drilling Program), 3–31. doi:10.2973/odp.proc.sr.127128-1.111.1992

Paull, C.K., Lorenson, T.D., Dickens, G., Borowski, W.S., Ussler, W., III, and Kvenvolden, K., 2000. Comparisons of in situ and core gas measurements in ODP Leg 164 bore holes. *Ann. New York Acad. Sci.,* 912:23–31. doi:10.1111/j.1749-6632.2000.tb06756.x

Pribnow, D., Kinoshita, M., and Stein, C., 2000. *Thermal Data Collection and Heat Flow Recalculations for Ocean Drilling Program Legs 101–180:* Hanover, Germany (Inst. Joint Geosci. Res., Inst. Geowiss. Gemeinschaftsauf. [GGA]). http://www-odp.tamu.edu/publications/heatflow/ODPReprt.pdf

Reeburgh, W.S., 1976. Methane consumption in Cariaco Trench waters and sediments. *Earth Planet. Sci. Lett.,* 28(3):337–344. **doi:10.1016/0012-821X(76)90195-3**

Shipboard Scientific Party, 1990. Site 795. *In* Tamaki, K., Pisciotto, K., Allan, J., et al., *Proc. ODP, Init. Repts.,* 127: College Station, TX (Ocean Drilling Program), 169–245. **doi:10.2973/odp.proc.ir.127.105.1990**

Shipboard Scientific Party, 2003a. Site 1230. *In* D'Hondt, S.L., Jørgensen, B.B., Miller, D.J., et al., *Proc. ODP, Init. Repts.,* 201: College Station, TX (Ocean Drilling Program), 1–107. **doi:10.2973/odp.proc.ir.201.111.2003**

Shipboard Scientific Party, 2003b. Site 1244. *In* Tréhu, A.M, Bohrmann, G., Rack, F.R., Torres, M.E., et al., *Proc. ODP, Init. Repts.,* 204: College Station, TX (Ocean Drilling Program), 1–132. **doi:10.2973/odp.proc.ir.204.103.2003**

Snyder, G.T, Hiruta, A., Matsumoto, R., Dickens, G.R., Tomaru, H., Takeuchi, R., Komatsubara, J., Ishida, Y., and Yu, H., 2007. Pore water profiles and authigenic mineralization in shallow marine sediments above the methane-charged system on Umitaka Spur, Japan Sea. *Deep-Sea Res., Part II,* 54(11–13):1216–1239. **doi:10.1016/j.dsr2.2007.04.001**

Tada, R., 1994. Paleoceanographic evolution of the Japan Sea. *Palaeogeogr., Palaeoclimatol., Palaeoecol.,* 108(3–4):487–508. **doi:10.1016/0031-0182(94)90248-8**

Tada, R., 2004. Onset and evolution of millennial-scale variability in the Asian monsoon and its impact on paleoceanography of the Japan Sea. *In* Clift, P., Kuhnt, W., Wang, P., and Hayes, D. (Eds.), *Continent-Ocean Interactions within East Asian Marginal Seas*. Geophys. Monogr., 149:283–298. **doi:10.1029/149GM15**

Tada, R., and Iijima, A., 1992. Lithostratigraphy and compositional variation of Neogene hemipelagic sediments in the Japan Sea. *In* Tamaki, K., Suyehiro, K., Allan, J., McWilliams, M., et al., *Proc. ODP, Sci. Results,* 127/128 (Pt. 2): College Station, TX (Ocean Drilling Program), 1229–1260. **doi:10.2973/odp.proc.sr.127128-2.188.1992**

Tada, R., Koizumi, I., Cramp, A., and Rahman, A., 1992. Correlation of dark and light layers, and the origin of their cyclicity in the Quaternary sediments from the Japan Sea. *In* Pisciotto, K.A., Ingle, J.C., Jr., von Breymann, M.T., Barron, J., et al., *Proc. ODP, Sci. Results,* 127/128 (Pt. 1): College Station, TX (Ocean Drilling Program), 577–601. **doi:10.2973/odp.proc.sr.127128-1.160.1992**

Tada, R., Murray, R.W., Alvarez Zarikian, C.A., Anderson, W.T., Jr., Bassetti, M.-A., Brace, B.J., Clemens, S.C., da Costa Gurgel, M.H., Dickens, G.R., Dunlea, A.G., Gallagher, S.J., Giosan, L., Henderson, A.C.G., Holbourn, A.E., Ikehara, K., Irino, T., Itaki, T., Karasuda, A., Kinsley, C.W., Kubota, Y., Lee, G.S., Lee, K.E., Lofi, J., Lopes, C.I.C.D., Peterson, L.C., Saavedra-Pellitero, M., Sagawa, T., Singh, R.K., Sugisaki, S., Toucanne, S., Wan, S., Xuan, C., Zheng, H., and Ziegler, M., 2015a. Expedition 346 summary. *In* Tada, R., Murray, R.W., Alvarez Zarikian, C.A., and the Expedition 346 Scientists, *Proc. IODP,* 346: College Station, TX (Integrated Ocean Drilling Program). **doi:10.2204/iodp.proc.346.101.2015**

Tada, R., Murray, R.W., Alvarez Zarikian, C.A., Anderson, W.T., Jr., Bassetti, M.-A., Brace, B.J., Clemens, S.C., da Costa Gurgel, M.H., Dickens, G.R., Dunlea, A.G., Gallagher, S.J., Giosan, L., Henderson, A.C.G., Holbourn, A.E., Ikehara, K., Irino, T., Itaki, T., Karasuda, A., Kinsley, C.W., Kubota, Y., Lee, G.S., Lee, K.E., Lofi, J., Lopes, C.I.C.D., Peterson, L.C., Saavedra-Pellitero, M., Sagawa, T., Singh, R.K., Sugisaki, S., Toucanne, S., Wan, S., Xuan, C., Zheng, H., and Ziegler, M., 2015b. Methods. *In* Tada, R., Murray, R.W., Alvarez Zarikian, C.A., and the Expedition 346 Scientists, *Proc. IODP,* 346: College Station, TX (Integrated Ocean Drilling Program). **doi:10.2204/iodp.proc.346.102.2015**

Tada, R., Murray, R.W., Alvarez Zarikian, C.A., Anderson, W.T., Jr., Bassetti, M.-A., Brace, B.J., Clemens, S.C., da Costa Gurgel, M.H., Dickens, G.R., Dunlea, A.G., Gallagher, S.J., Giosan, L., Henderson, A.C.G., Holbourn, A.E., Ikehara, K., Irino, T., Itaki, T., Karasuda, A., Kinsley, C.W., Kubota, Y., Lee, G.S., Lee, K.E., Lofi, J., Lopes, C.I.C.D., Peterson, L.C., Saavedra-Pellitero, M., Sagawa, T., Singh, R.K., Sugisaki, S., Toucanne, S., Wan, S., Xuan, C., Zheng, H., and Ziegler, M., 2015c. Site U1423. *In* Tada, R., Murray, R.W., Alvarez Zarikian, C.A., and the Expedition 346 Scientists, *Proc. IODP,* 346: College Station, TX (Integrated Ocean Drilling Program). **doi:10.2204/iodp.proc.346.104.2015**

Tada, R., Murray, R.W., Alvarez Zarikian, C.A., Anderson, W.T., Jr, Bassetti, M.-A., Brace, B.J., Clemens, S.C., Dickens, G.R., Dunlea, A.G., Gallagher, S.J., Giosan, L., da Costa Gurgel, M.H., Henderson, A.C.G., Holbourn, A.E., Ikehara, K., Irino, T., Itaki, T., Karasuda, A., Kinsley, C.W., Kubota, Y., Lee, G.S., Lee, K.E., Lofi, J., Lopes, C.I.C.D., Peterson, L.C., Saavedra-Pellitero, M., Sagawa, T., Singh, R.K., Sugisaki, S., Toucanne, S., Wan, S., Xuan, C., Zheng, H., and Ziegler, M., 2015d. Site U1425. *In* Tada, R., Murray, R.W., Alvarez Zarikian, C.A., and the Expedition 346 Scientists, *Proc. IODP,* 346: College Station, TX (Integrated Ocean Drilling Program). **doi:10.2204/iodp.proc.346.106.2015**

Talley, L.D., Lobanov, V., Ponomarev, V., Salyuk, A., Tishchenko, P., Zhabin, I., and Riser, S., 2003. Deep convection and brine rejection in the Japan Sea. *Geophys. Res. Lett.,* 30(4):1159. **doi:10.1029/2002GL016451**

Talley, L.D., Min, D.-H., Lobanov, V.B., Luchin, V.A., Ponomarev, V.I., Salyuk, A.N., Shcherbina, A.Y., Tishchenko, P.Y., and Zhabin, I., 2006. Japan/East Sea water masses and their relation to the sea's circulation. *Oceanography,* 19(3):32–49. **doi:10.5670/oceanog.2006.42**

Tamaki, K., Suyehiro, K., Allan, J., Ingle, J.C., Jr., and Pisciotto, K.A., 1992. Tectonic synthesis and implications of Japan Sea ODP drilling. *In* Tamaki, K., Suyehiro, K., Allan, J., McWilliams, M., et al., *Proc. ODP, Sci. Results,* 127/128 (Pt. 2): College Station, TX (Ocean Drilling Program), 1333–1348. **doi:10.2973/odp.proc.sr.127128-2.240.1992**

Tishchenko, P.Y., Pavlova, G.Y., and Shkirnikova, E.M., 2012. A new look at the alkalinity of the Sea of Japan. *Oceanology,* 52(1):21–33. **doi:10.1134/S0001437011060191**

Vasiliev, M.A., Blum, P., Chubarian, G., Olsen, R., Bennight, C., Cobine, T., Fackler, D., Hastedt, M., Houpt, D., Mateo, Z., and Vasilieva, Y.B., 2011. A new natural gamma radiation measurement system for marine sediment and rock analysis. *J. Appl. Geophys.,* 75:455–463. **doi:10.1016/j.jappgeo.2011.08.008**

von Breymann, M.T., Brumsack, H., and Emeis, K.C., 1992. Depositional and diagenetic behavior of barium in the Japan Sea. *In* Pisciotto, K.A., Ingle, J.C., Jr., von Breymann, M.T., Barron, J., et al., *Proc. ODP, Sci. Results,* 127/128 (Pt. 1): College Station, TX (Ocean Drilling Program), 651–665. **doi:10.2973/odp.proc.sr.127128-1.168.1992**

Xuan, C., and Channell, J.E.T., 2009. UPmag: MATLAB software for viewing and processing U channel or other pass-through paleomagnetic data. *Geochem., Geophys., Geosyst.,* 10(10):Q10Y07. **doi:10.1029/2009GC002584**

Yoon, J.-H., and Kim, Y.-J., 2009. Review on the seasonal variation of the surface circulation in the Japan/East Sea. *J. Mar. Syst.,* 78(2):226–236. **doi:10.1016/j.jmarsys.2009.03.003**

You, C.-F., Gieskes, J.M., Chen, R.F., Spivack, A., and Gamo, T., 1993. Iodide, bromide, manganese, boron, and dissolved organic carbon in interstitial waters of the organic carbon–rich marine sediments: observations in the Nankai accretionary prism. *In* Hill, I.A., Taira, A., Firth, J.V., et al., *Proc. ODP, Sci. Results,* 131: College Station, TX (Ocean Drilling Program), 165–174. **doi:10.2973/odp.proc.sr.131.116.1993**

Publication: 28 March 2015
MS 346-103

Figure F1. Bathymetric map of Expedition 346 sites (red circles) in the body of water between the Eurasian continent, the Korean Peninsula, and the Japanese Islands and the East China Sea. Sites previously drilled by the Deep Sea Drilling Project (DSDP) and Ocean Drilling Program (ODP) (white circles) are also shown. Also illustrated are the region's surface current systems.

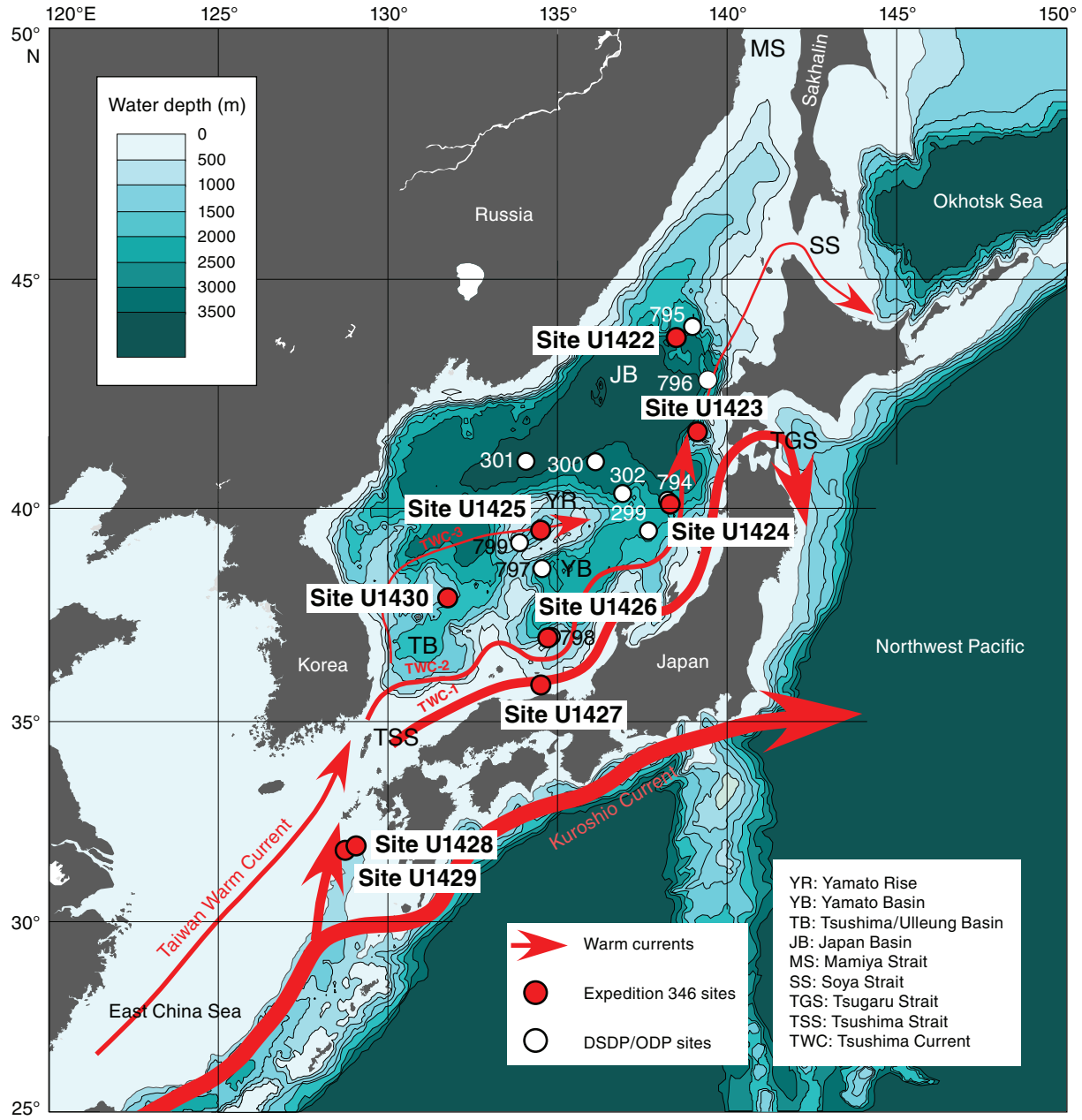

Figure F2. Lithologic summary, Hole U1422C. GRA = gamma ray attenuation.

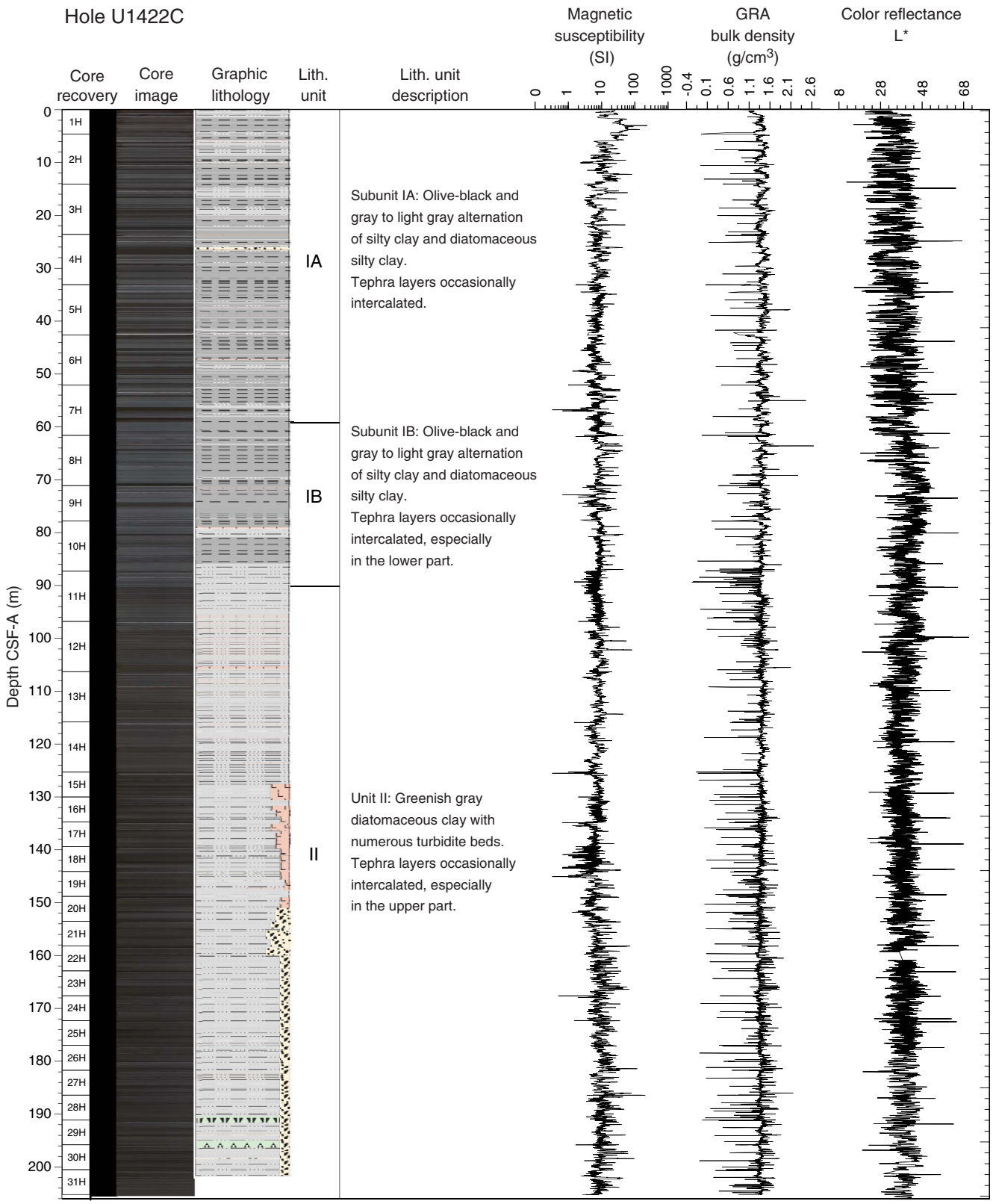

Figure F3. Lithologic summary, Hole U1422D. GRA = gamma ray attenuation.

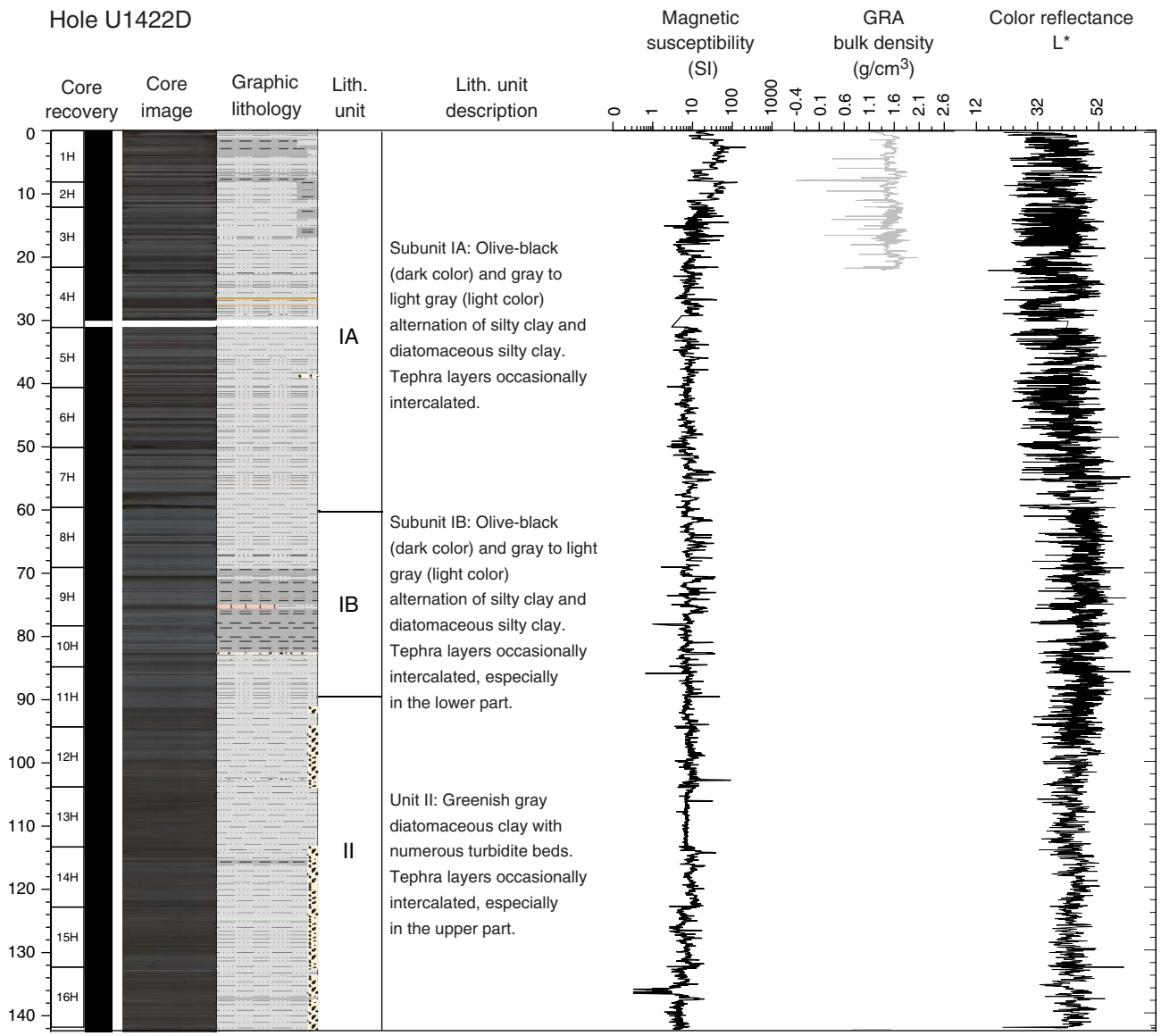

Figure F4. Lithologic summary, Hole U1422E. GRA = gamma ray attenuation.

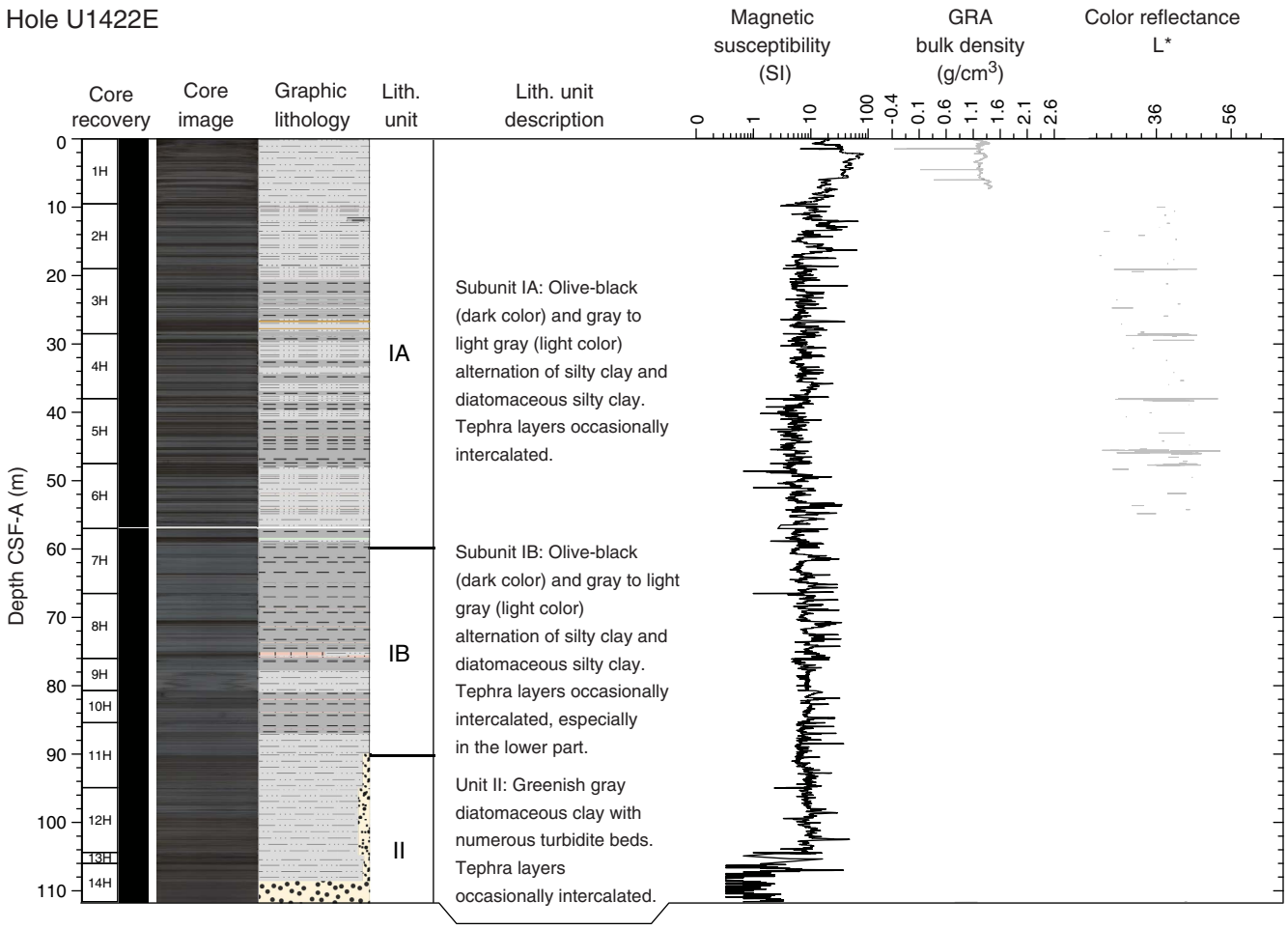

Figure F5. Hole-to-hole stratigraphic correlation, Site U1422.

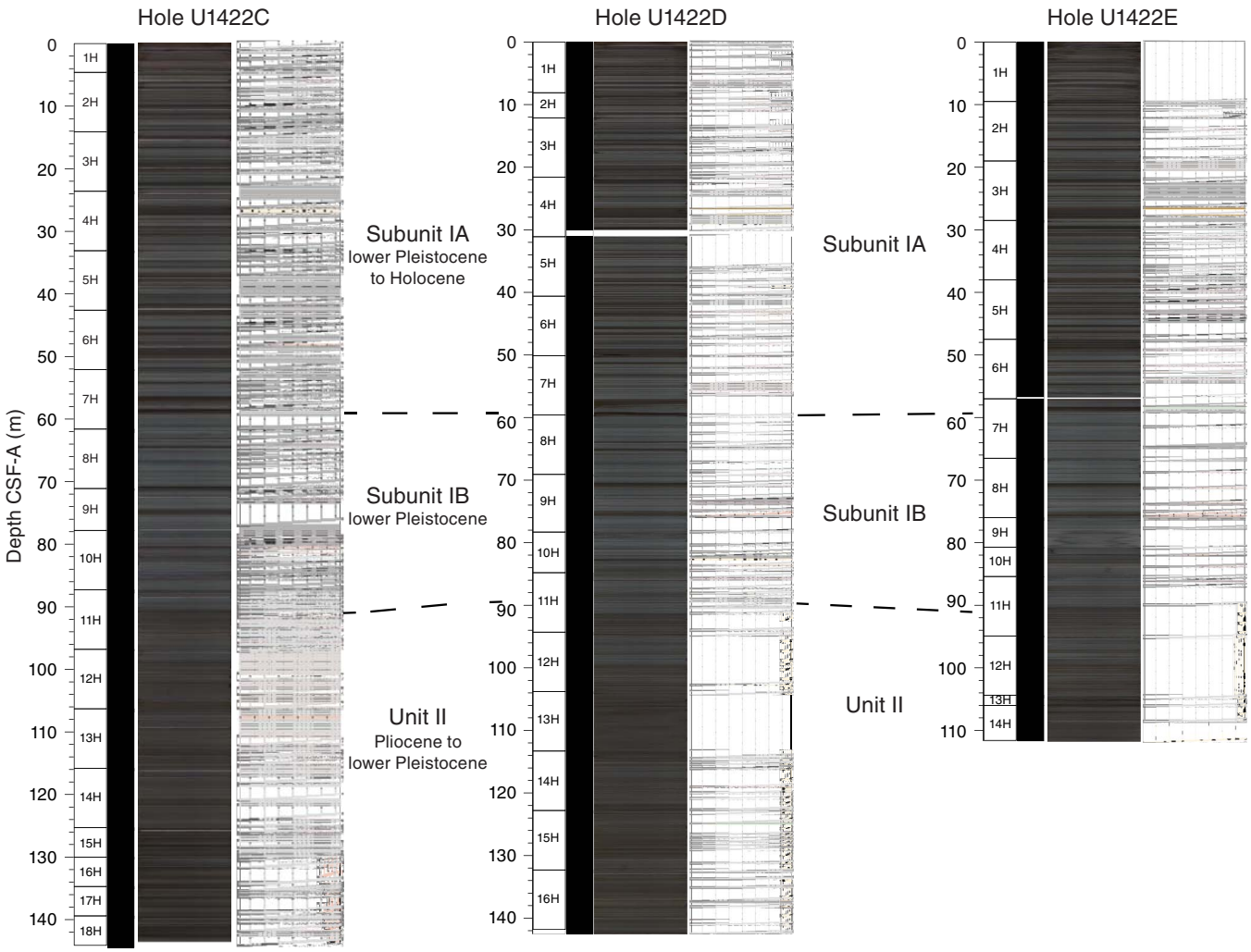

Figure F6. Scanning electron microscope image of a black spherule (Sample 346-U1422C-4H-CC).

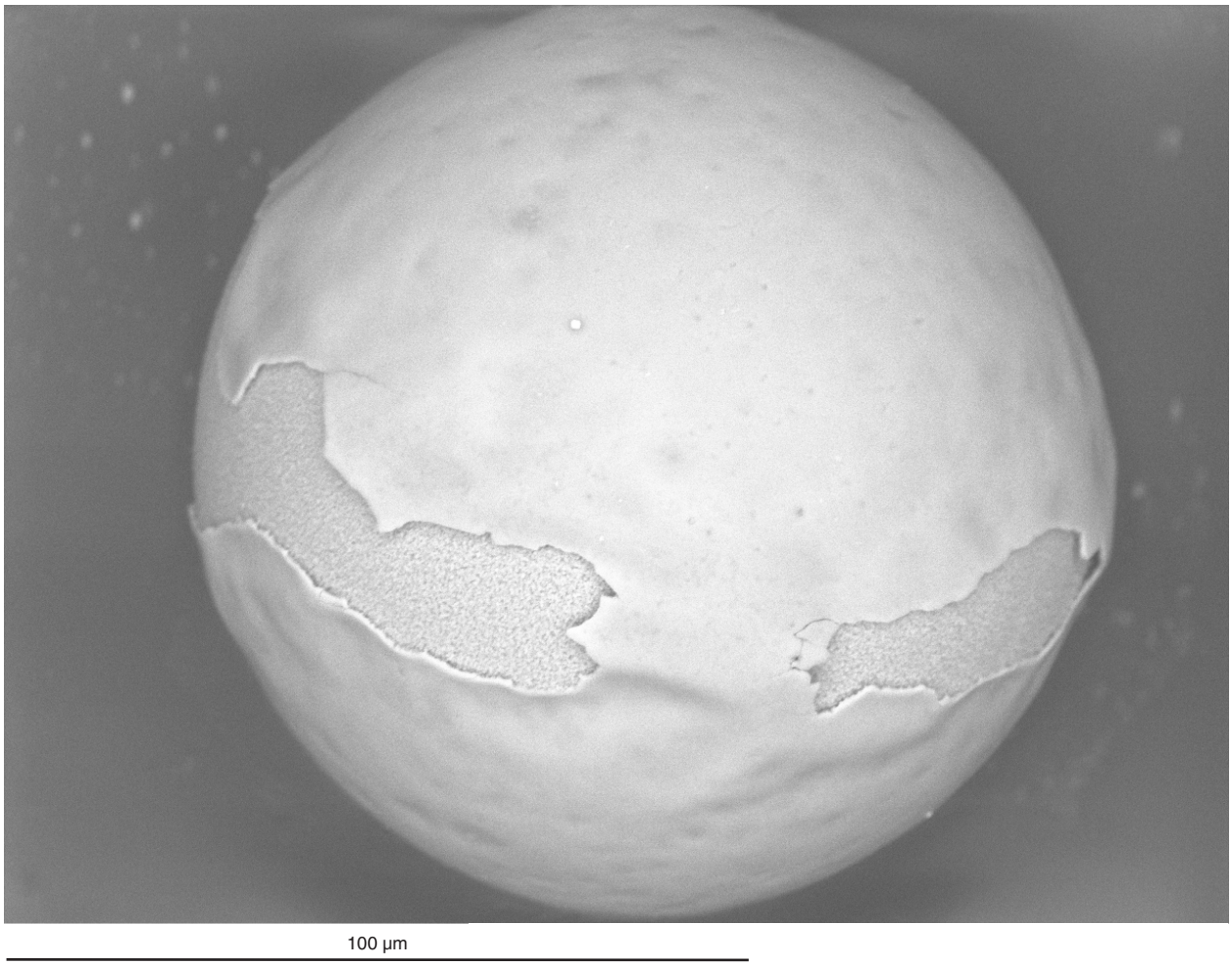

Figure F7. Variation of XRD peak intensity of identified minerals with depth, Hole U1422C.

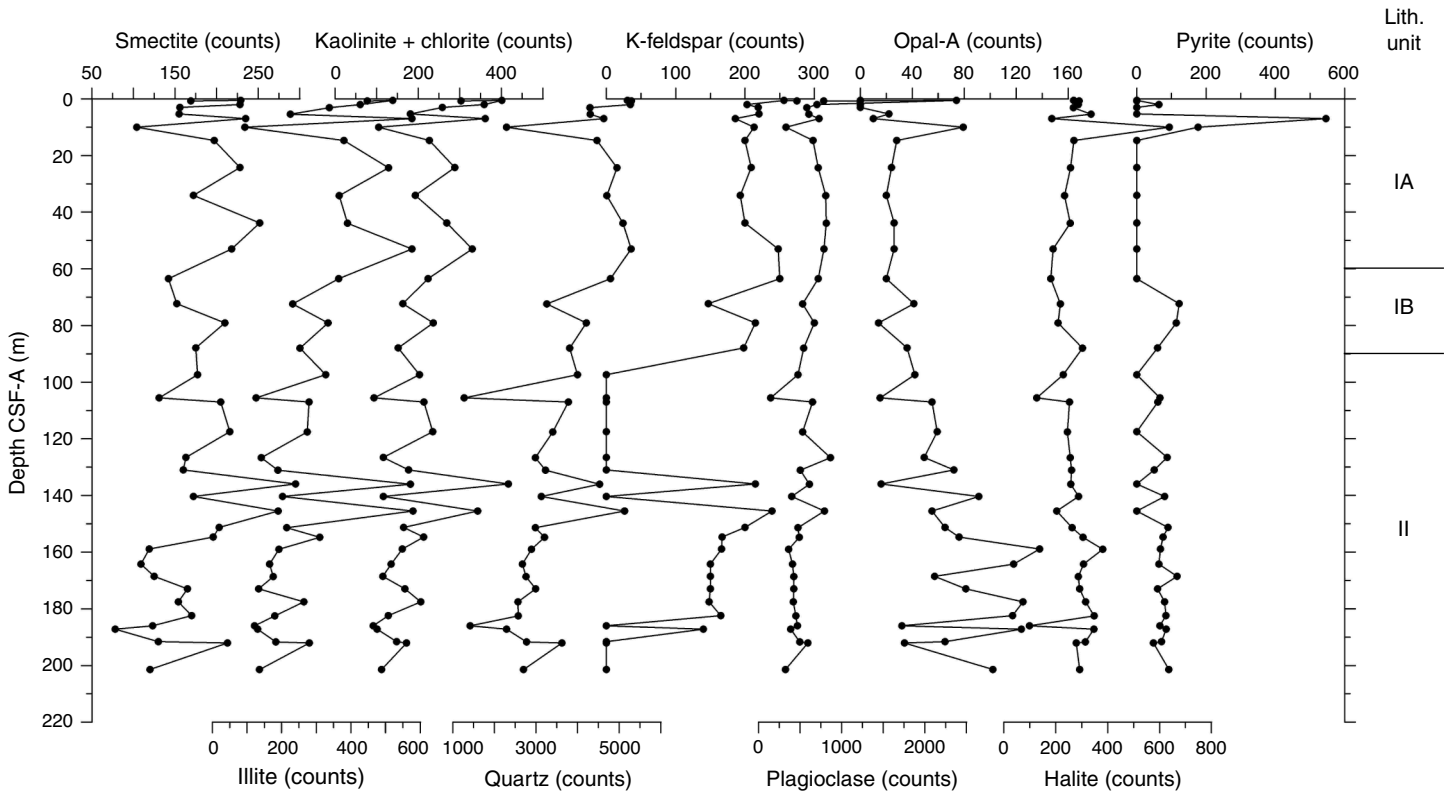

Figure F8. Photographs representative of Subunit IA in Holes U1422C and U1422D. Note enhanced color contrast to highlight sedimentary structures.

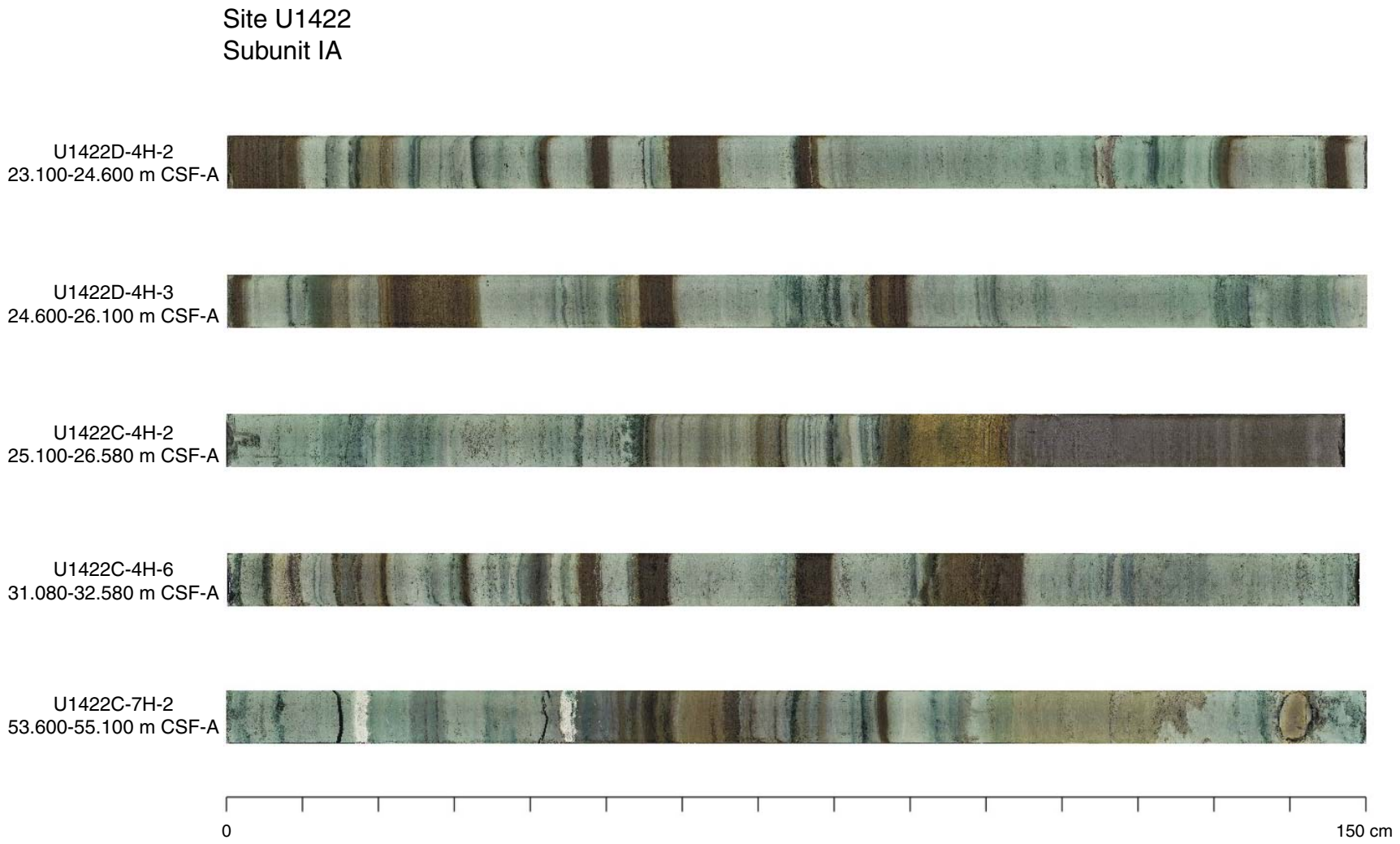

Figure F9. Volcanic glass shards with vesicular glass fragments (A) and opaque minerals (black) (Section 346-U1422E-5H-3A, 48 cm).

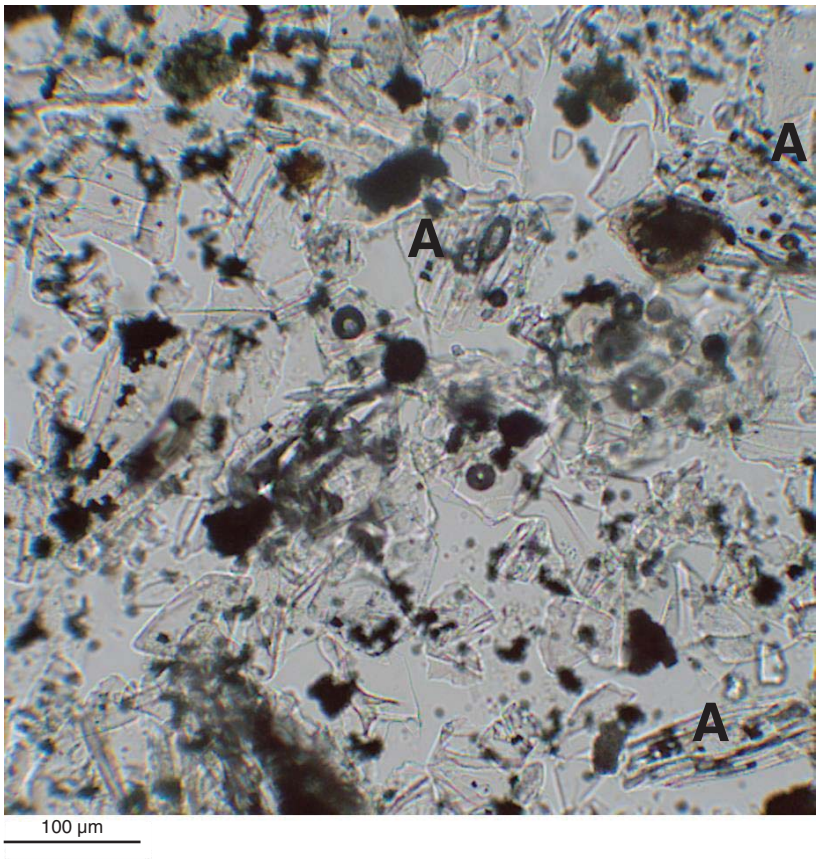

Figure F10. Phillipsite crystals (P) under polarized light. A cruciform phillipsite twin is visible (Section 346-U1422D-6H-6A, 26 cm).

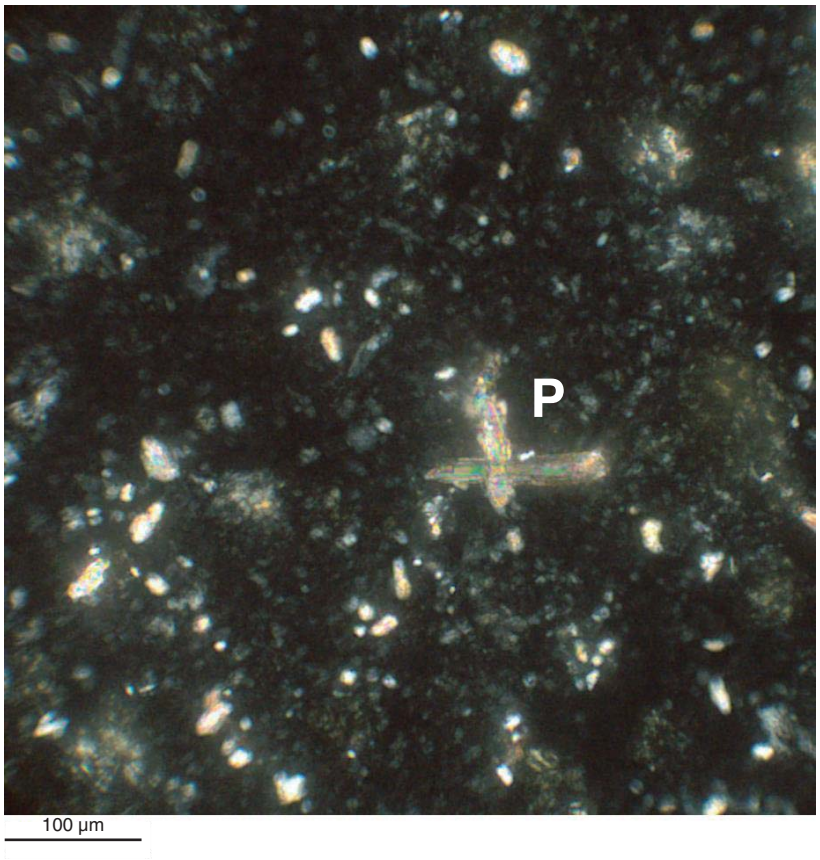

Figure F11. Photographs representative of Subunit IB in Holes U1422C, U1422D, and U1422E. Note enhanced color contrast to highlight sedimentary structures.

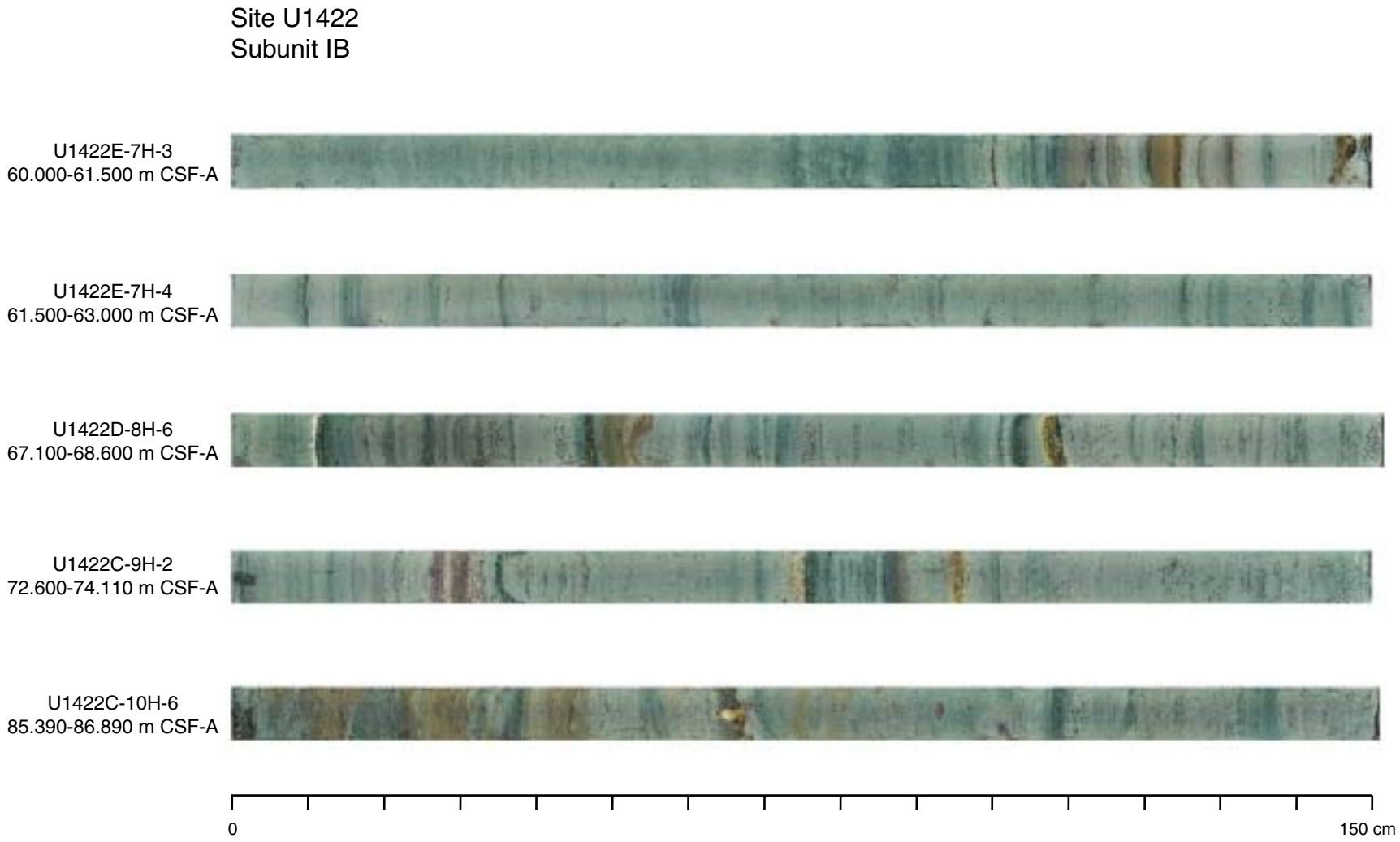

Figure F12. Diatom ooze in dark brown deposits (Section 346-U1422E-7H-1A, 140 cm).

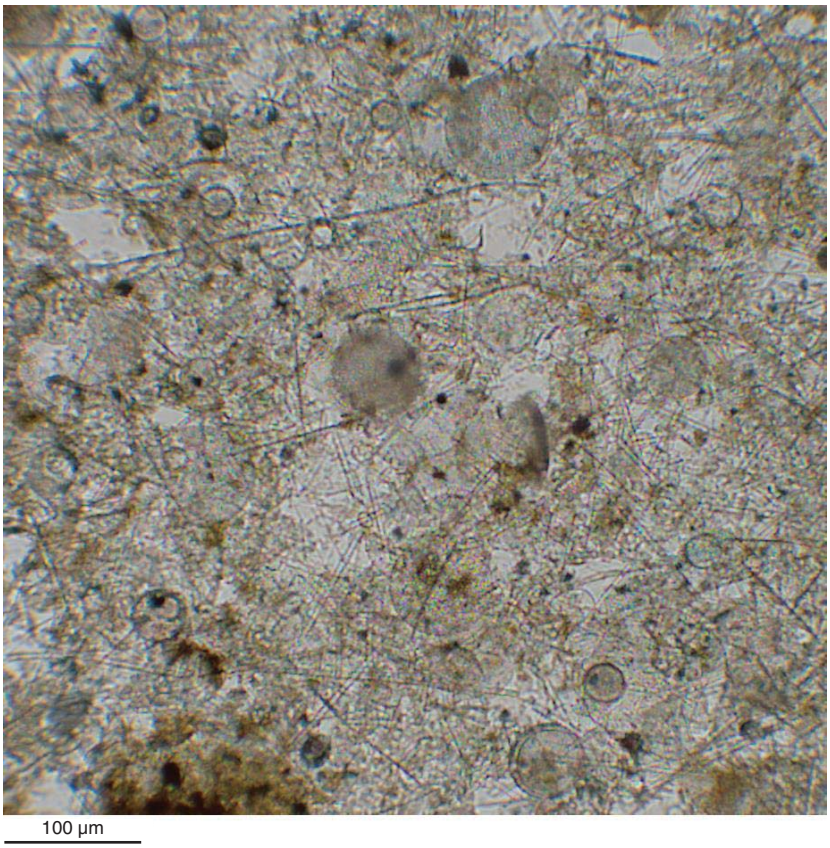

Figure F13. Photographs representative of Unit II in Holes U1422C and U1422D. Note enhanced color contrast to highlight sedimentary structures.

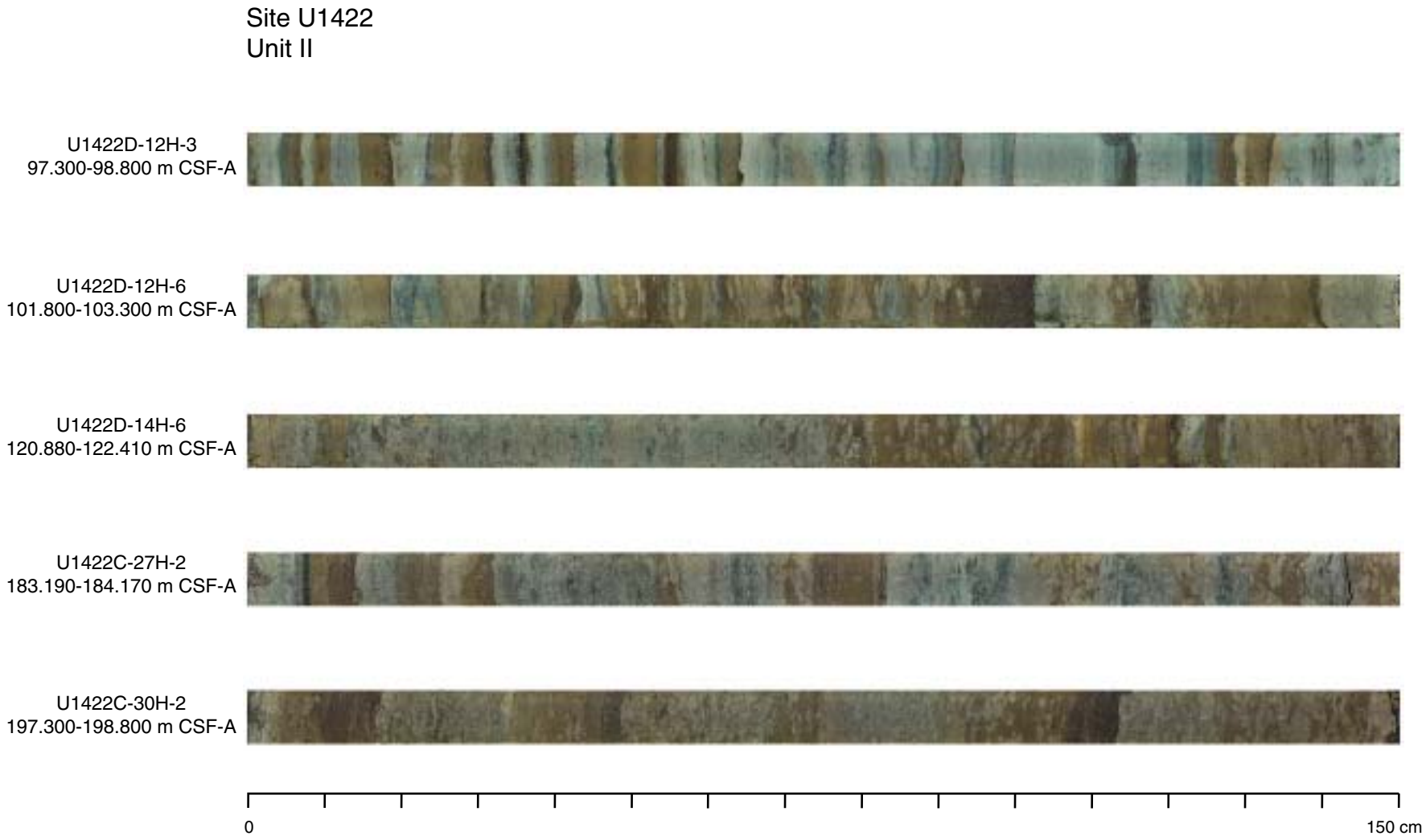

Figure F14. Example of turbidite beds in Unit II (interval 346-U1422C-23H-4, 23–51 cm). HM = hemipelagic mud, TM = turbidite mud, TS = turbidite sand.

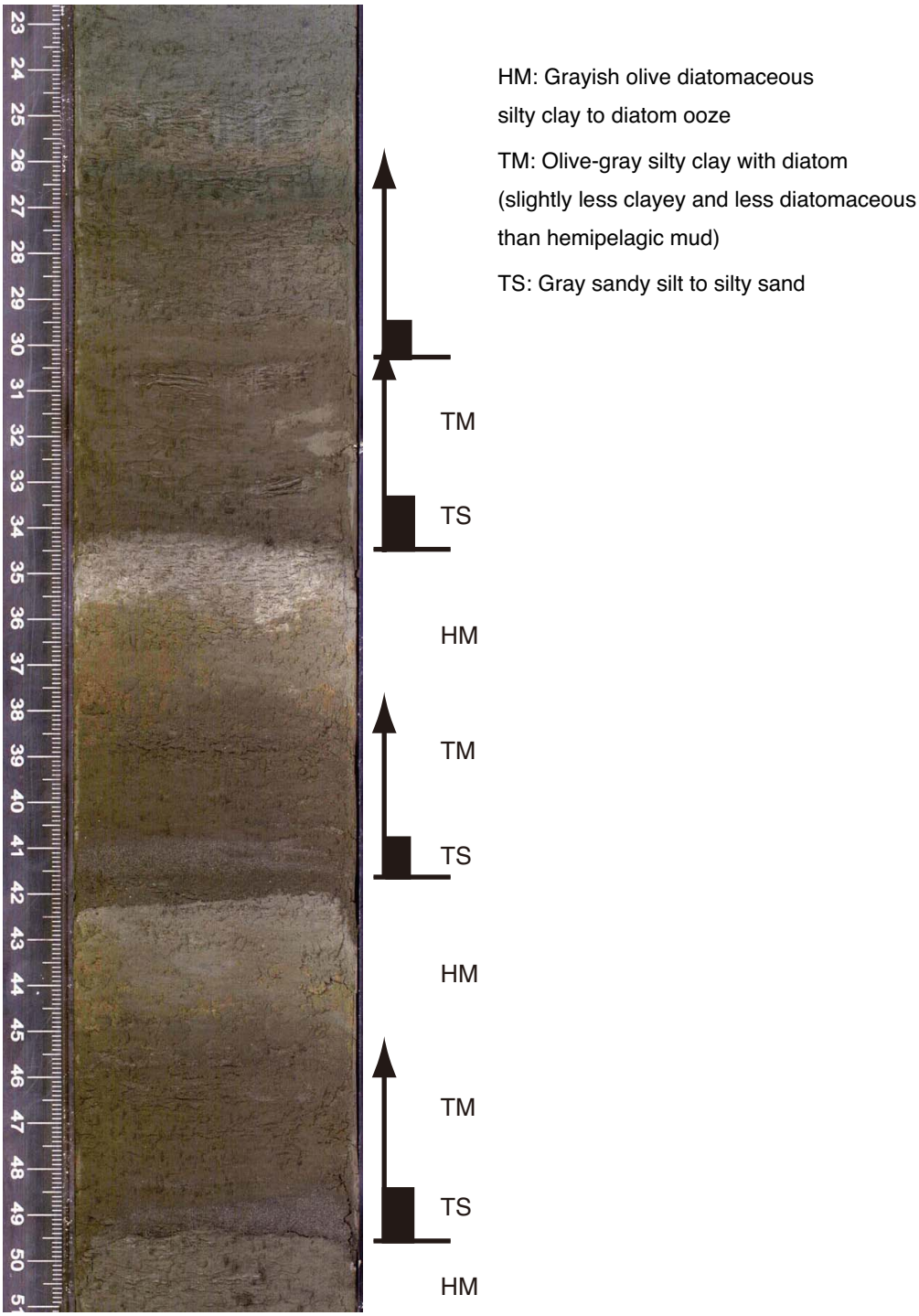

Figure F15. Change of grain size and composition with depth in a turbidite bed (interval 346-U1422C-21H-2, 45–62 cm). **A.** Hemipelagic mud (diatomaceous silty clay). **B.** Clayey silt with minor amount of diatoms. **C.** Silty sand with siliciclastic grains.

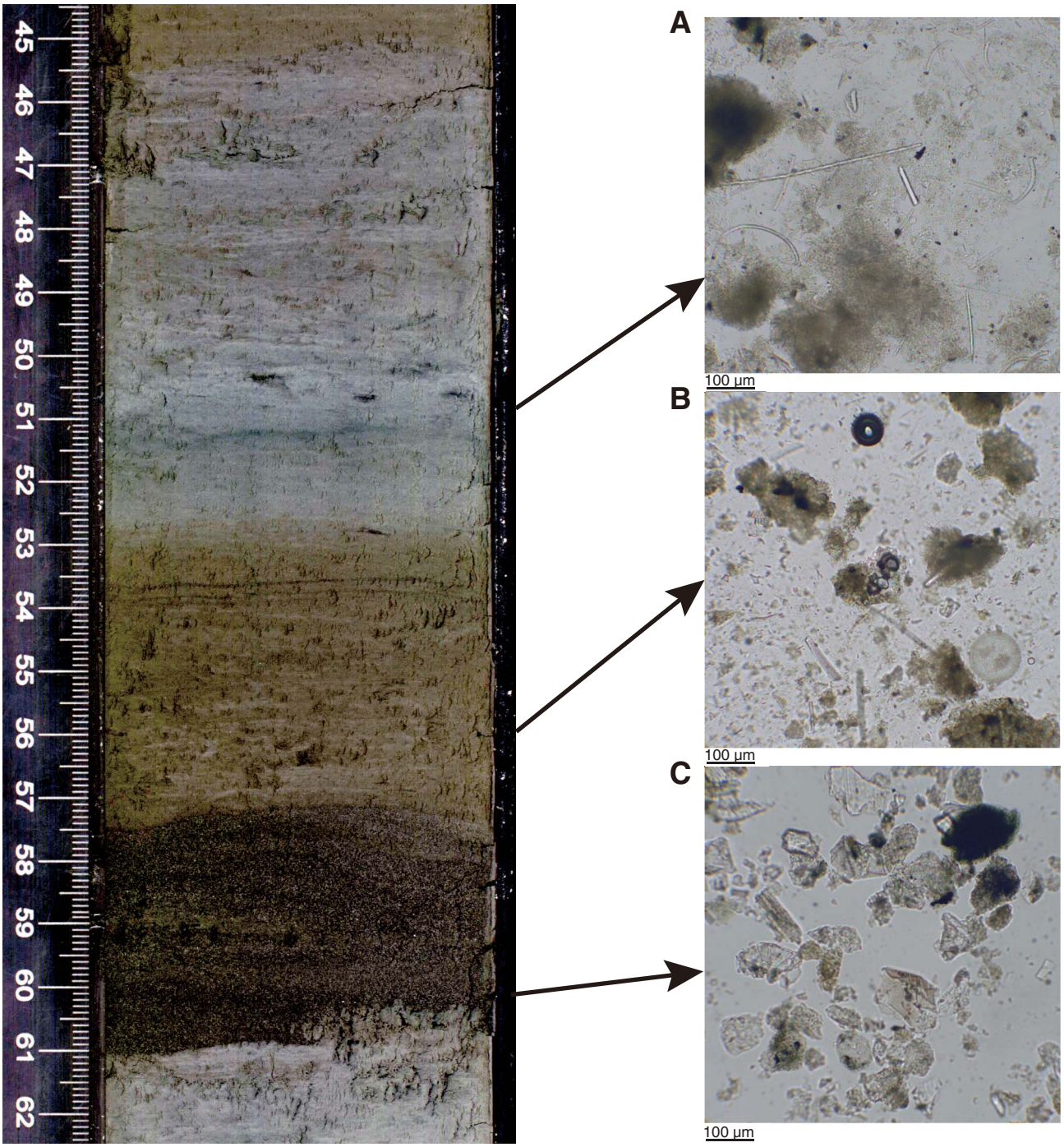

Figure F16. Integrated calcareous and siliceous microfossil biozonation, Site U1422.

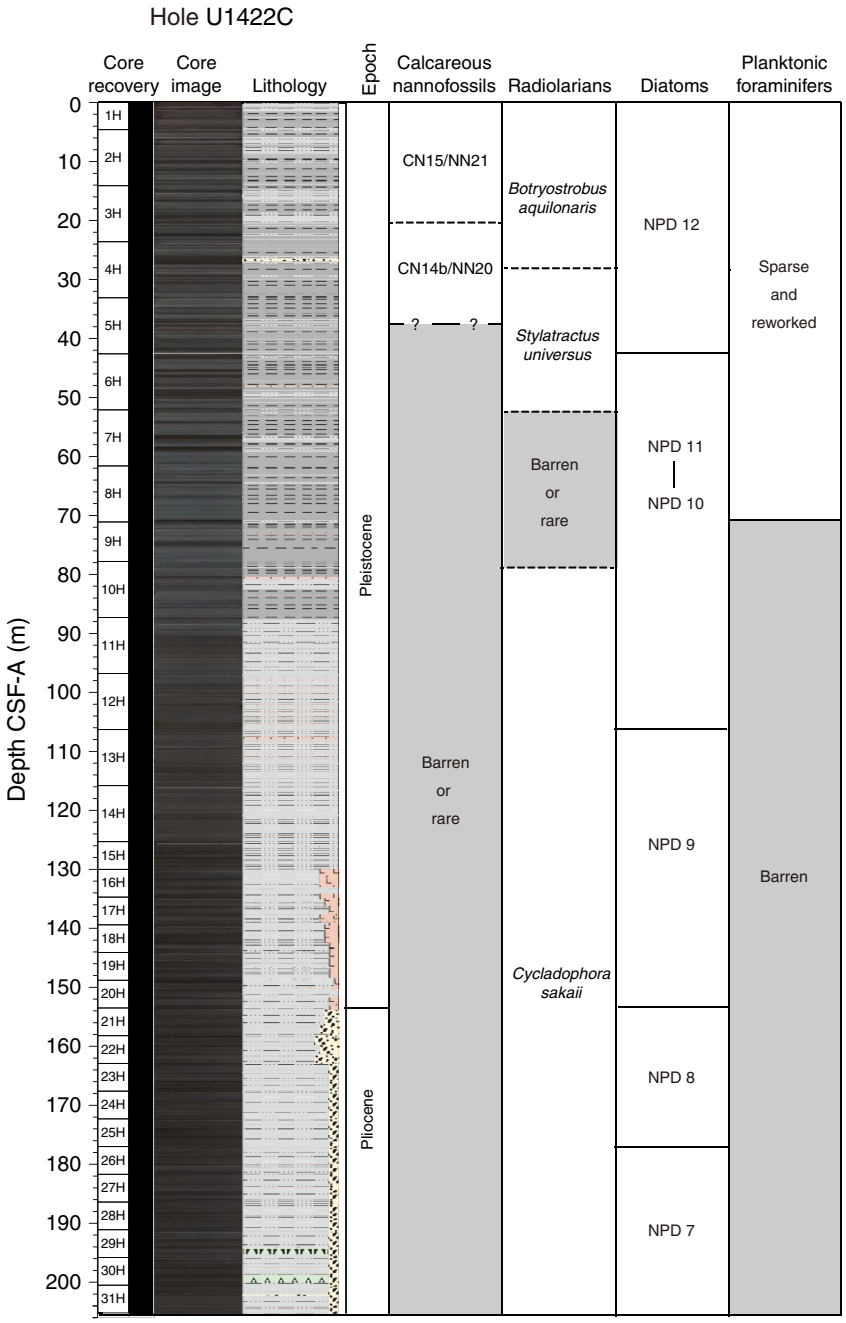

Figure F17. Age-depth profile, Site U1422.

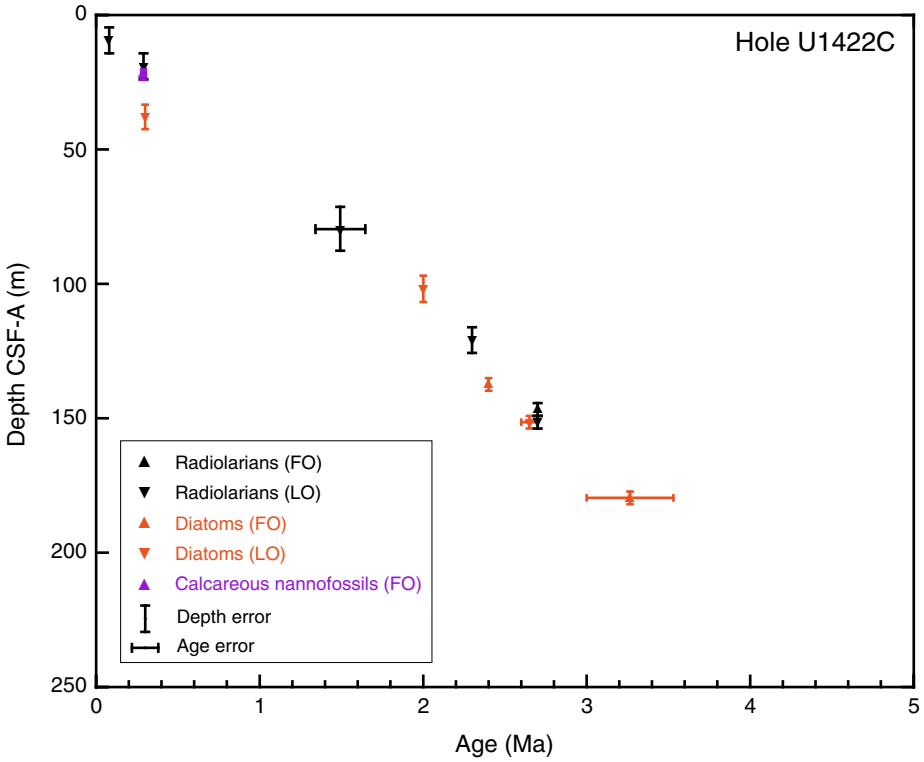

Figure F18. Abundance of siliceous and calcareous microfossils, Site U1422. B = barren, R = rare, F = few, C = common, A = abundant, D = dominant.

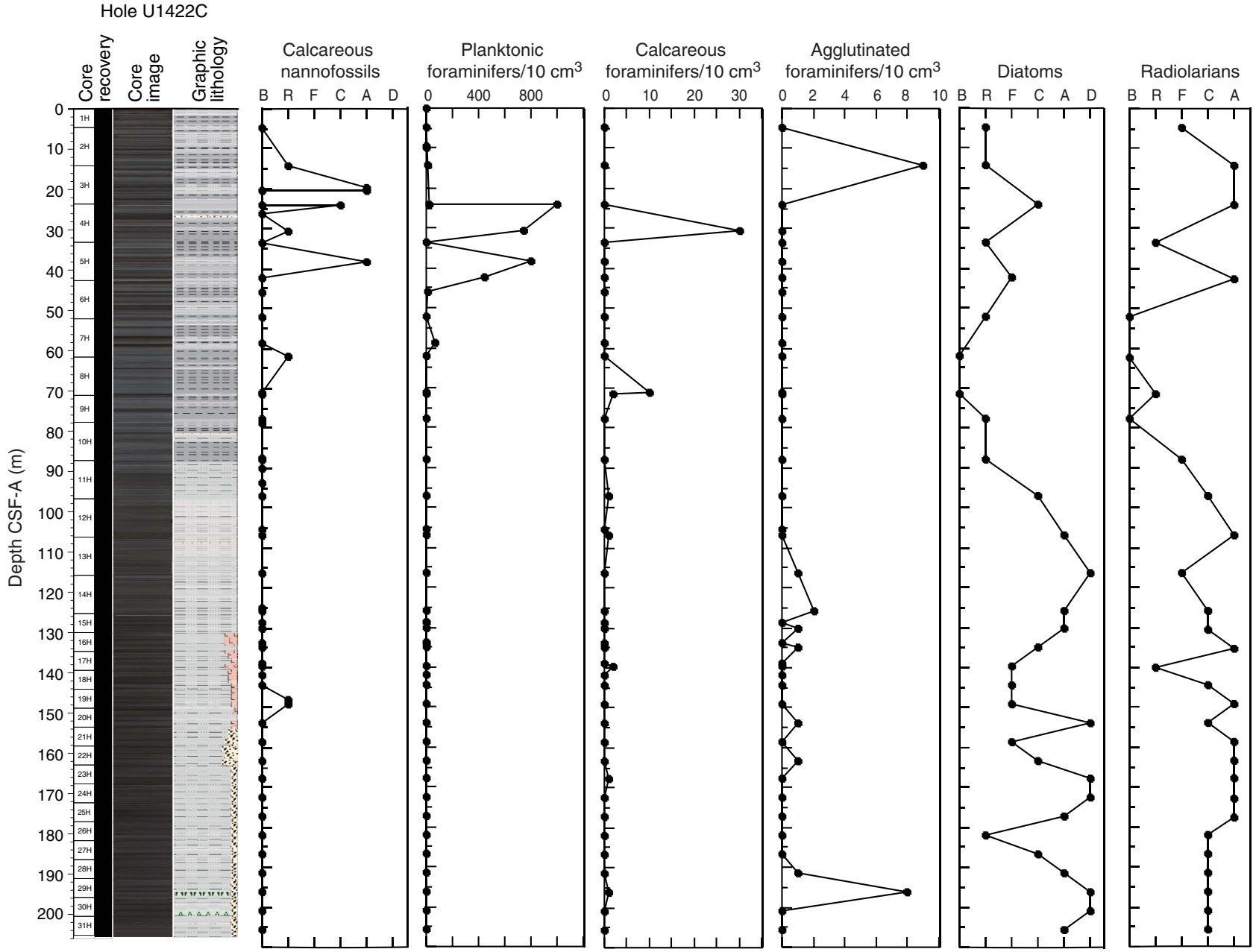

Figure F19. Diatom *Arachnodiscus* spp. (Sample 346-U1422C-31H-CC).

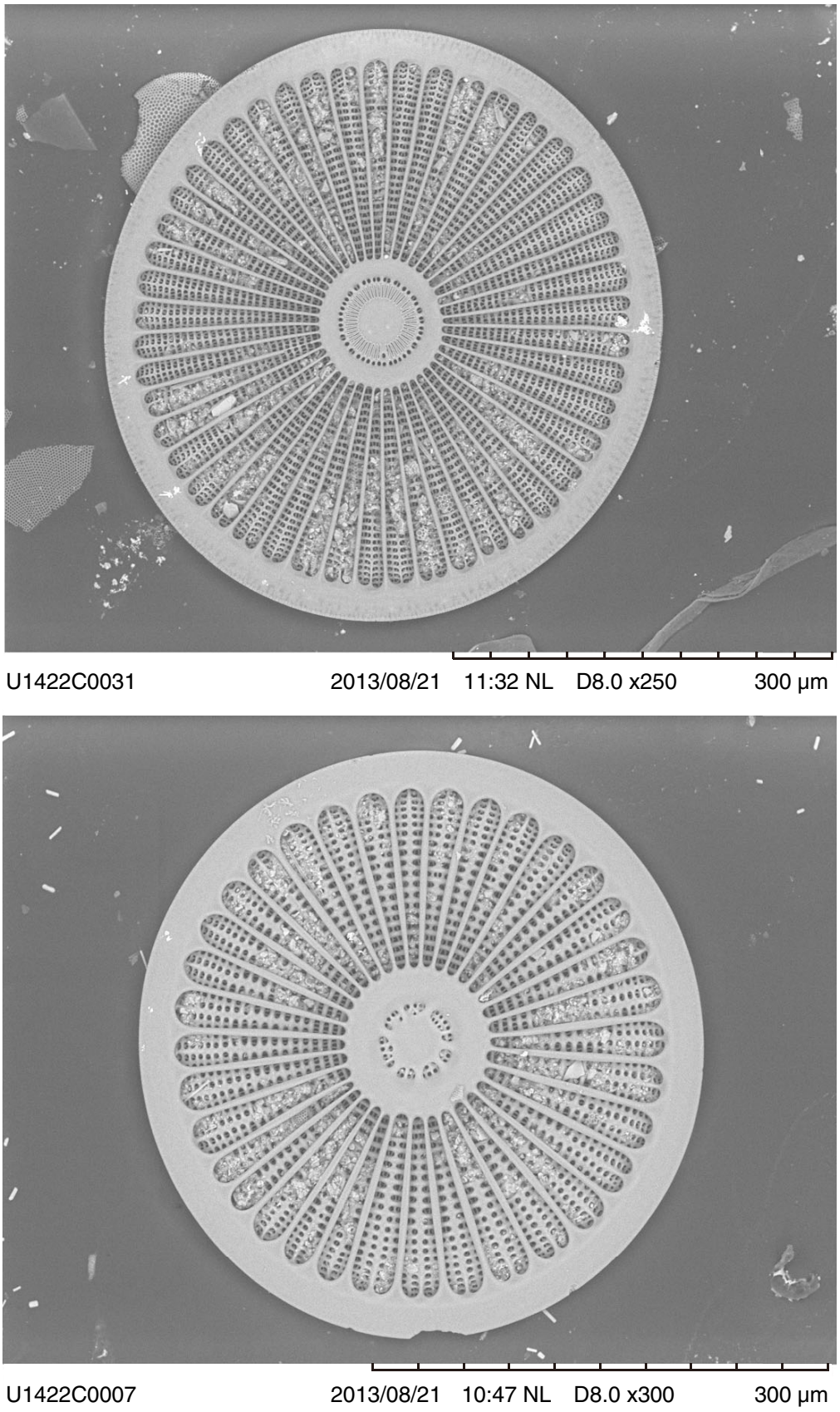

Figure F20. Planktonic foraminifers. Scale bars = 100 µm. **1, 2.** *Neogloboquadrina pachyderma* (Sample 346-U1422C-5H-4, 66–67 cm); (1) sinistral form; (2) dextral form. **3.** *Neogloboquadrina incompta* (sinistral) (Sample 346-U1422C-5H-4, 66–67 cm). **4, 5.** *Neogloboquadrina* sp. (Sample 346-U1422C-5H-4, 66–67 cm). **6, 7.** *Neogloboquadrina asanoi*; (6) Sample 346-U1422C-5H-4, 66–67 cm; (7) Sample 346-U1422C-6H-3, 36–37 cm. **8.** *Neogloboquadrina kaganesis* (Sample 346-U1422C-5H-4, 66–67 cm). **9.** *Globigerina bulloides* (Sample 346-U1422D-3H-6, 115–116 cm). **10, 10a.** *Globigerina umbilicata* (Sample 346-U1422D-3H-6, 115–116 cm).

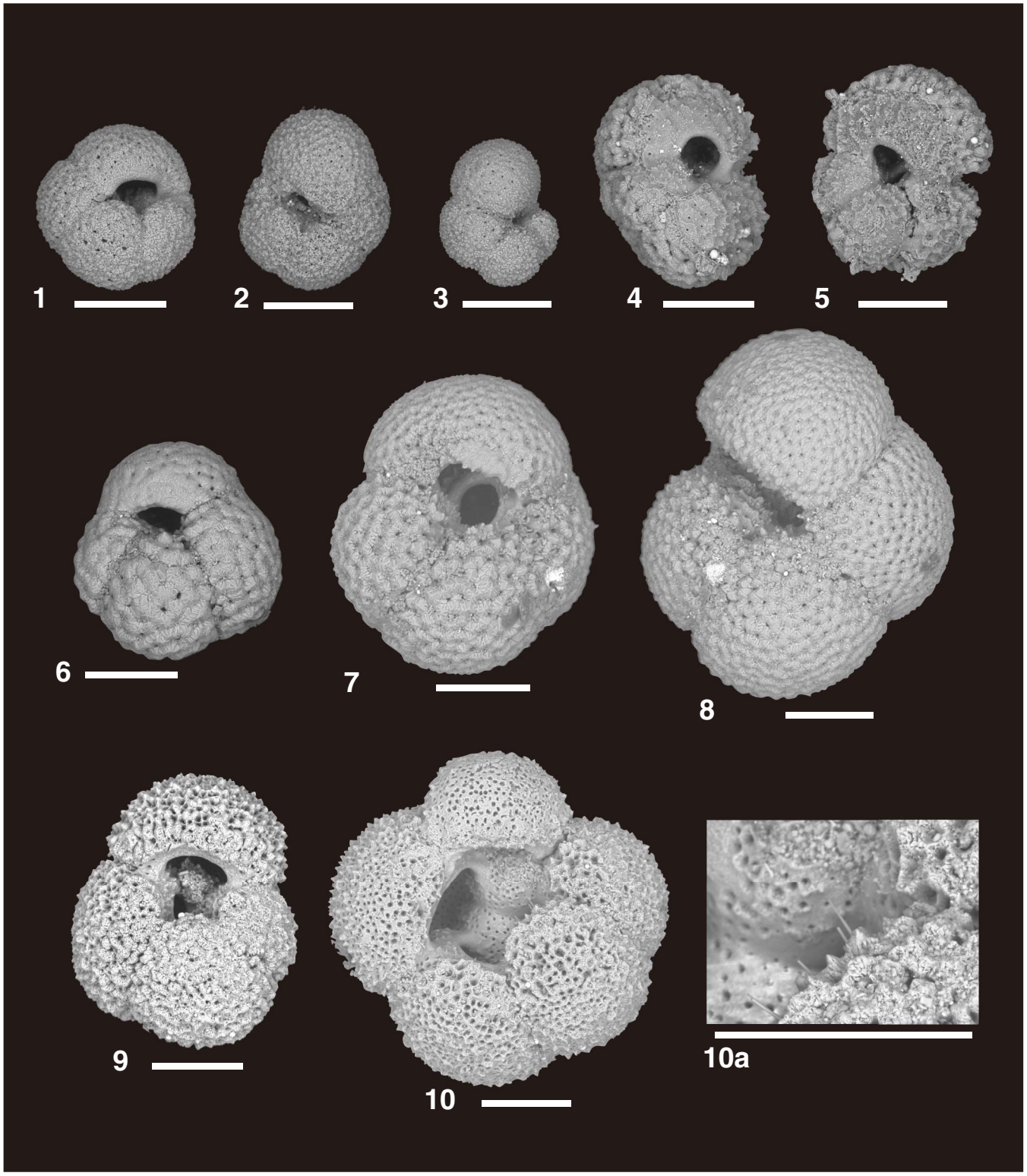

Figure F21. Fish teeth and benthic foraminifers. Scale bars = 10 µm, except figure 15 scale bar = 30 µm. **1.** Fish tooth (Sample 346-U1422C-4H-CC). **2.** *Eggerella bradyi* (Sample 346-U1422C-14H-CC). **3.** *Globobulimina pacifica* (Sample 346-U1422C-23H-CC). **4.** *Globobulimina pupoides* (Sample 346-U1422C-17H-CC). **5.** *Cibicidoides robertsonianus* (Sample 346-U1422C-11H-CC). **6–8.** *Miliammina echigoensis* (Sample 346-U1422C-29H-CC). **9, 10.** *Melonis pompilioides* (Sample 346-U1422C-29H-CC). **11.** Specimen of *Martinotiella* sp. exhibiting intense dissolution (Sample 346-U1422C-2H-CC). **12–15.** *Fursenkoina bradyi*; (12) Sample 346-U1422C-4H-5, 95–96 cm; (13–15) Sample 346-U1422C-8H-CC.

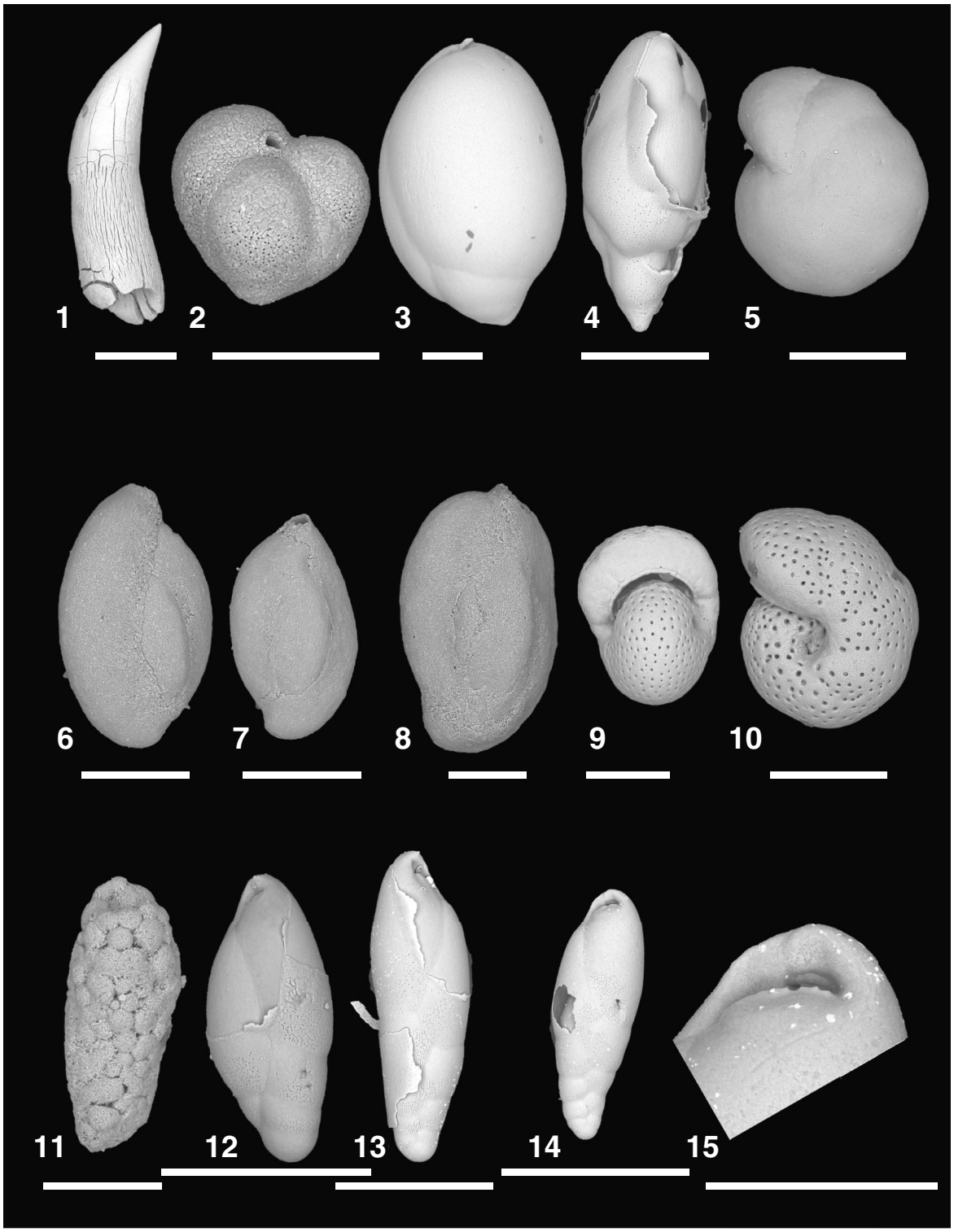

Figure F22. Fragile stained agglutinated foraminifers and fish tooth from Hole U1422D mudline sample. Scale bars = 50 µm, except figure 6 scale bar = 25 µm. **1, 2.** Coarse-grained tubular foraminifer with detail of wall structure. **3, 4.** Coarse-grained tubular foraminifer with detail of wall structure. **5, 6.** Fine-grained tubular foraminifer with detail of wall structure. **7, 8.** Fragment of coarse-grained tubular foraminifer with detail of wall structure. **9, 10.** Branching tubular foraminifer with detail of wall structure. **11.** Fragment of coarse-grained *Saccammina* sp. **12.** Fish tooth plate.

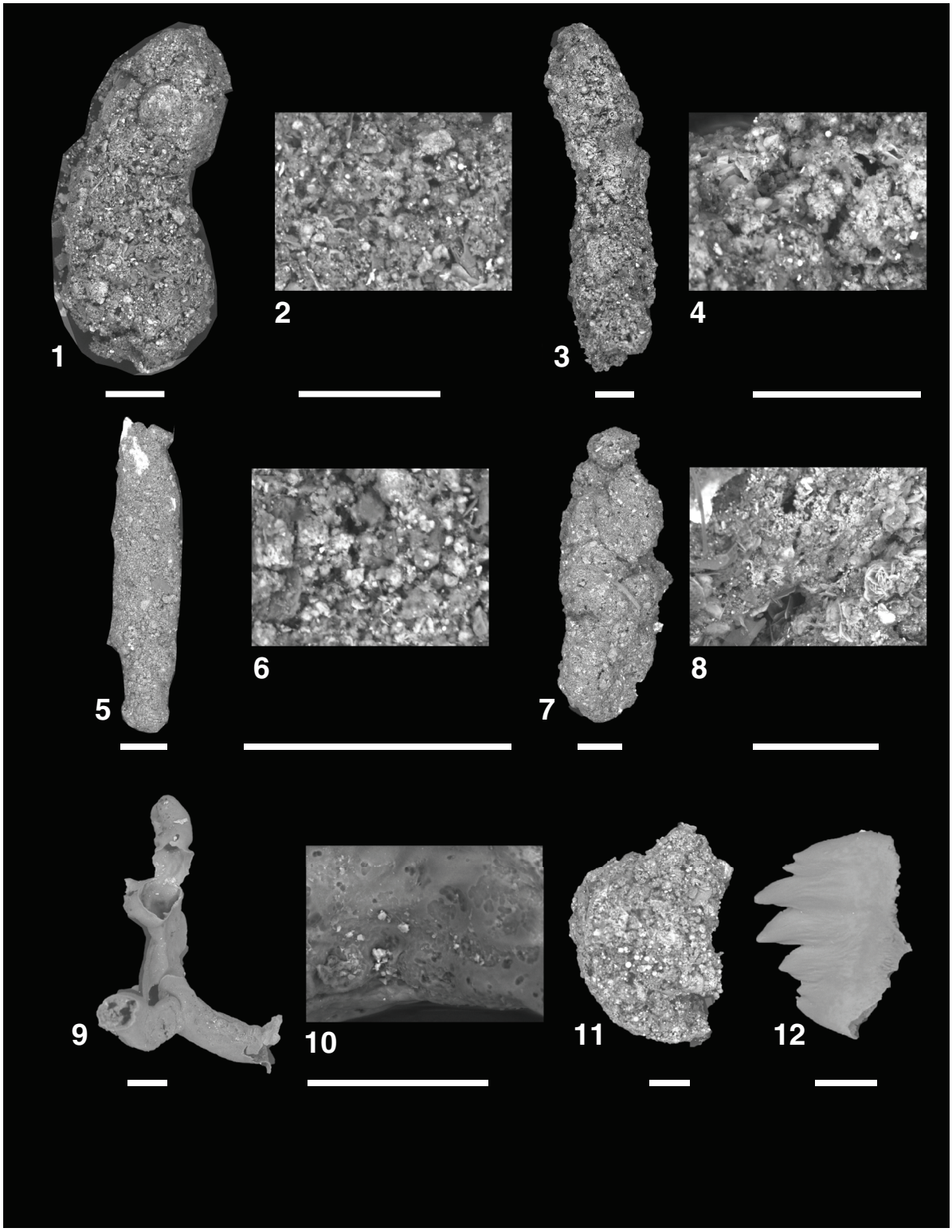

Figure F23. Solid-phase contents of discrete sediment samples, Site U1422. TC = total carbon, TOC = total organic carbon, TN = total nitrogen.

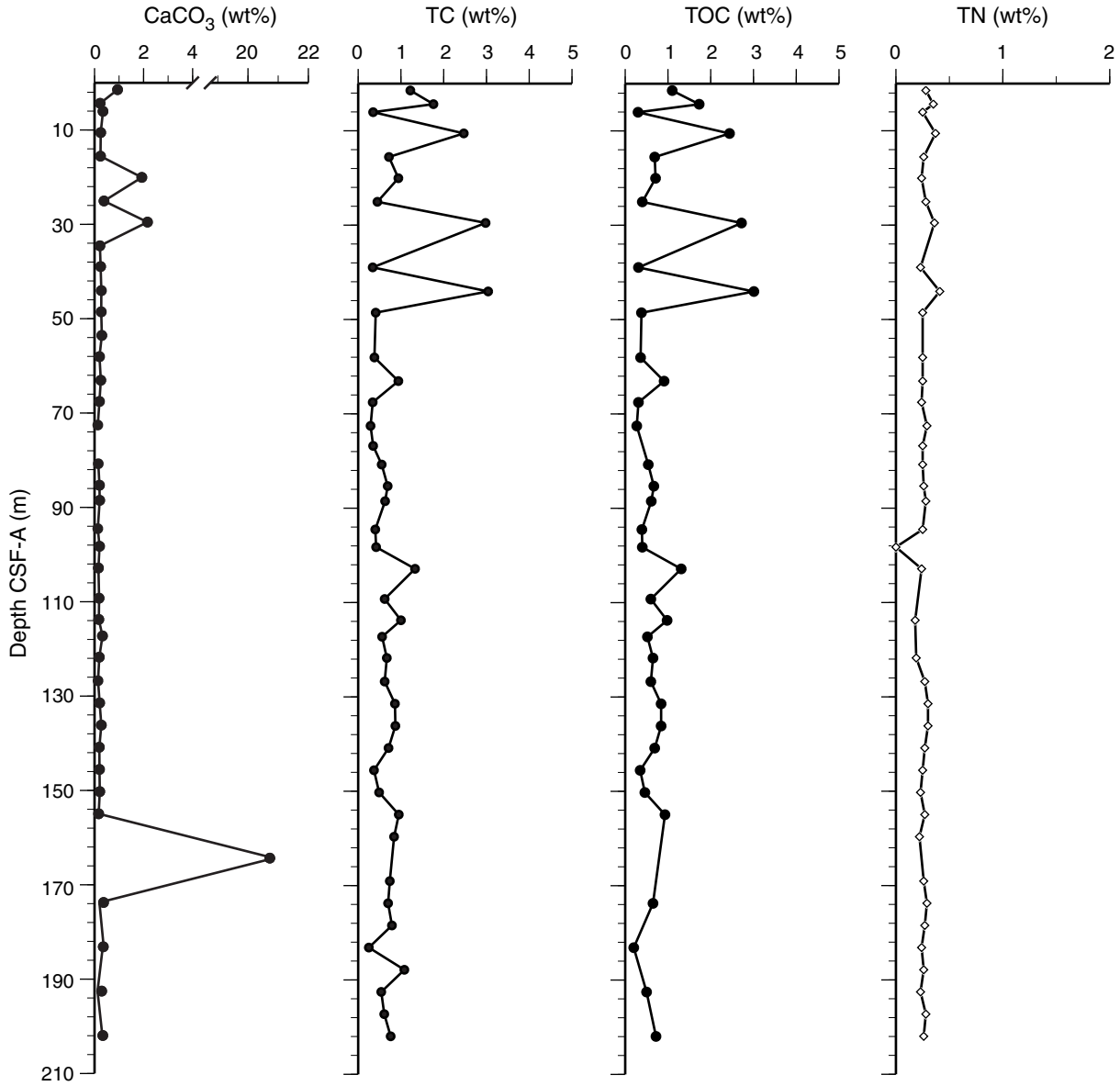

Figure F24. Dissolved iron and manganese profiles, Site U1422. **A.** Full depth of site. **B.** Uppermost 40 m below the seafloor.

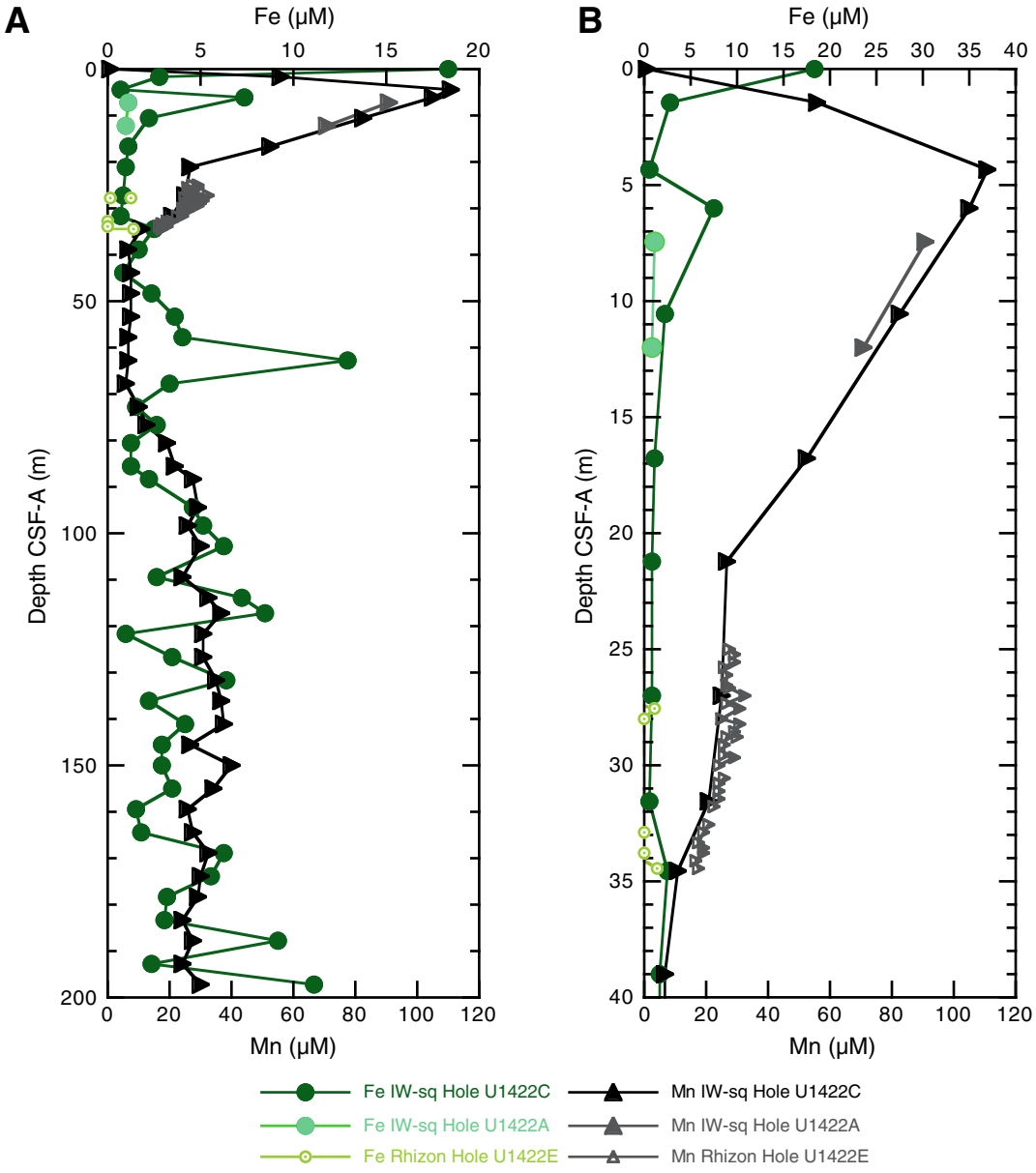

Figure F25. Dissolved alkalinity, ammonium, and phosphate profiles, Site U1422. Note the major kink in alkalinity at 35 m CSF-A.

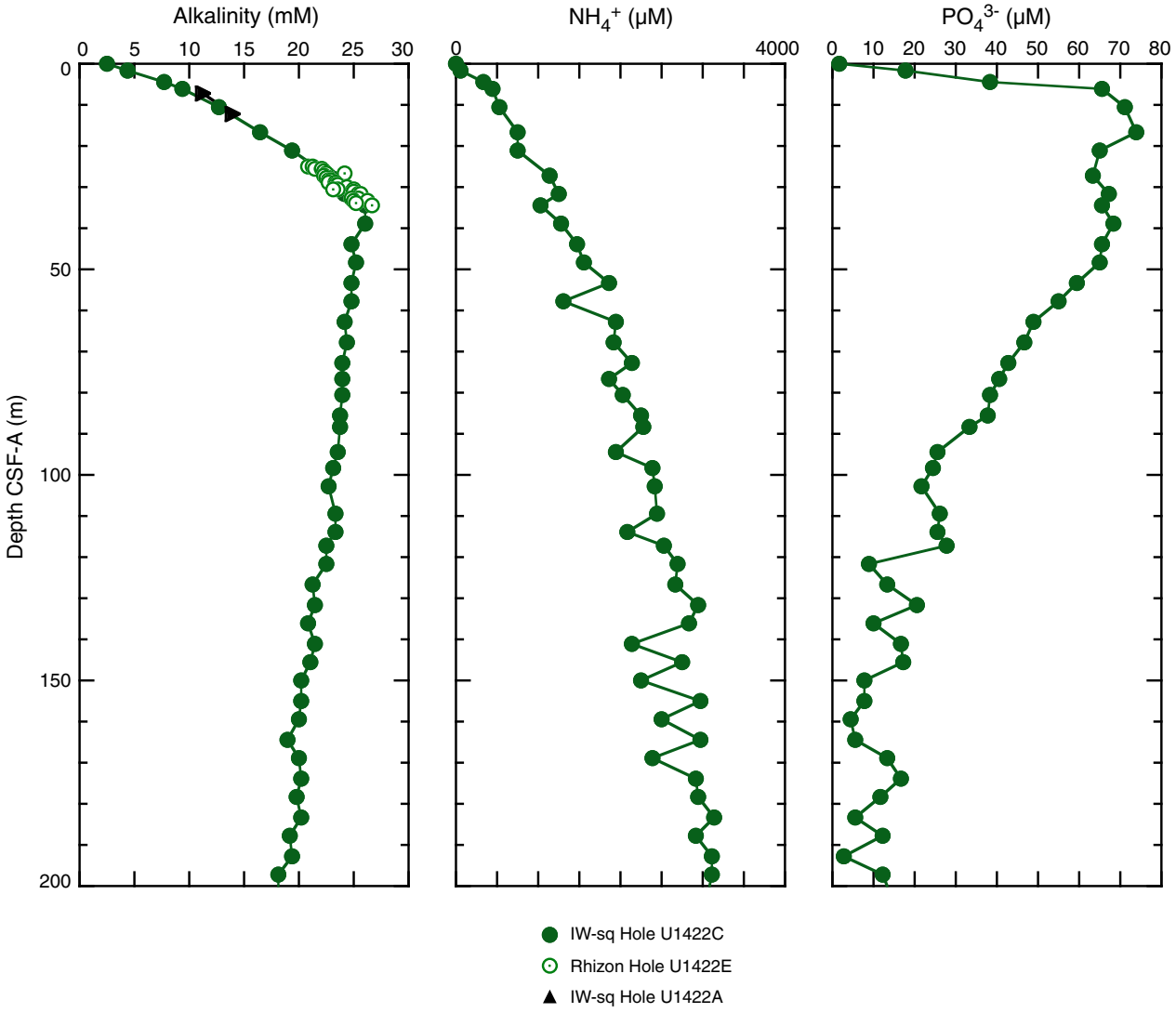

Figure F26. Headspace CH_4 concentrations, Site U1422. Note that values are not meaningful at depths where CH_4 surpasses saturation at 1 atm pressure (~40 m CSF-A).

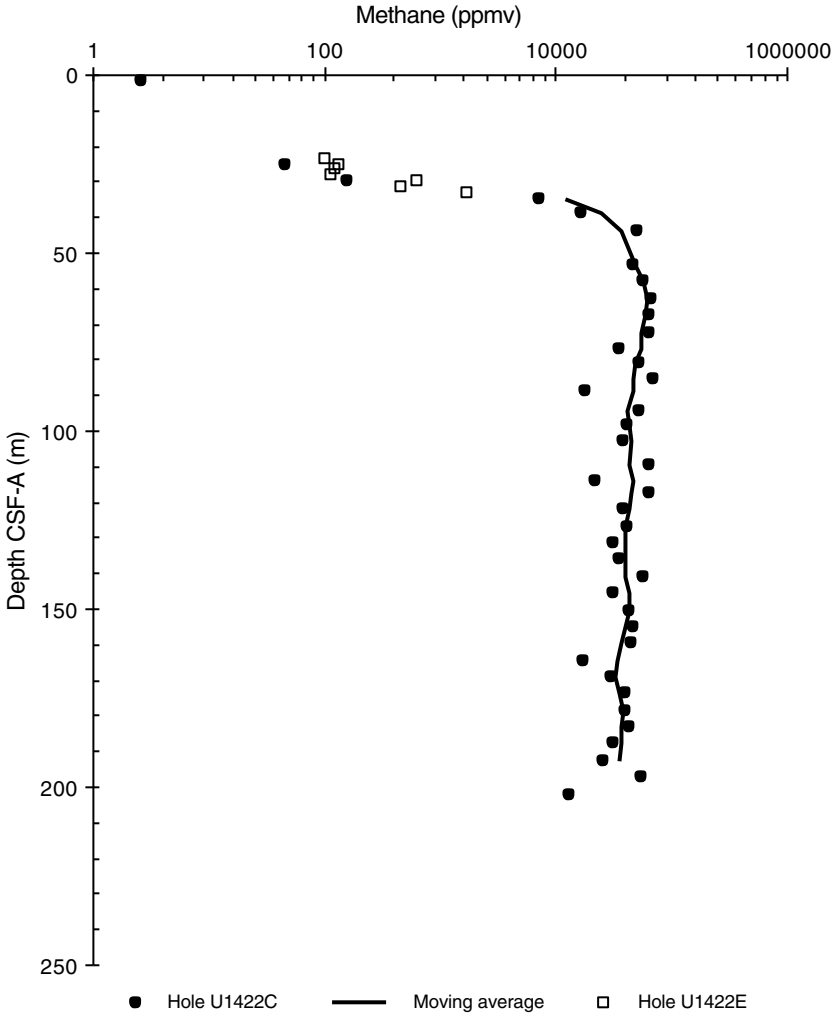

Figure F27. Yellowness and alkalinity versus depth, Site U1422. Symbols represent samples from different holes analyzed in different batches (Tables T11, T14) and demonstrate the reproducibility of the absorbance measurements at 325 nm.

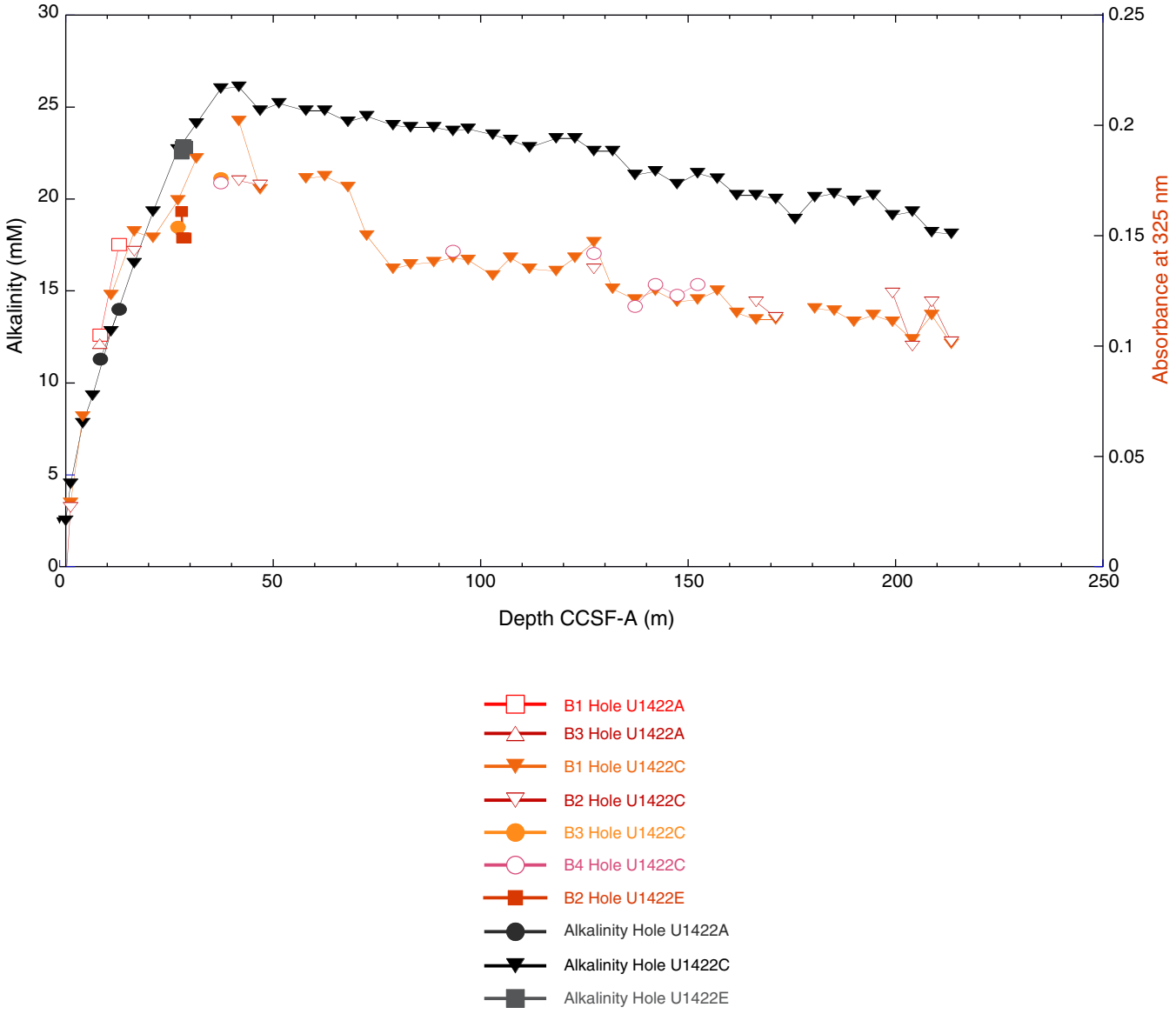

Figure F28. Dissolved sulfate and barium profiles, Site U1422. **A.** Full depth of site. **B.** Depth interval above the SMT at ~35 m CCSF-A. Interstitial water data from Rhizon sampling were collected from a different hole than interstitial water from squeezing and the data showed an offset when plotted on CSF-A. Here, they are plotted on CCSF-A to show the good agreement between the different sampling techniques.

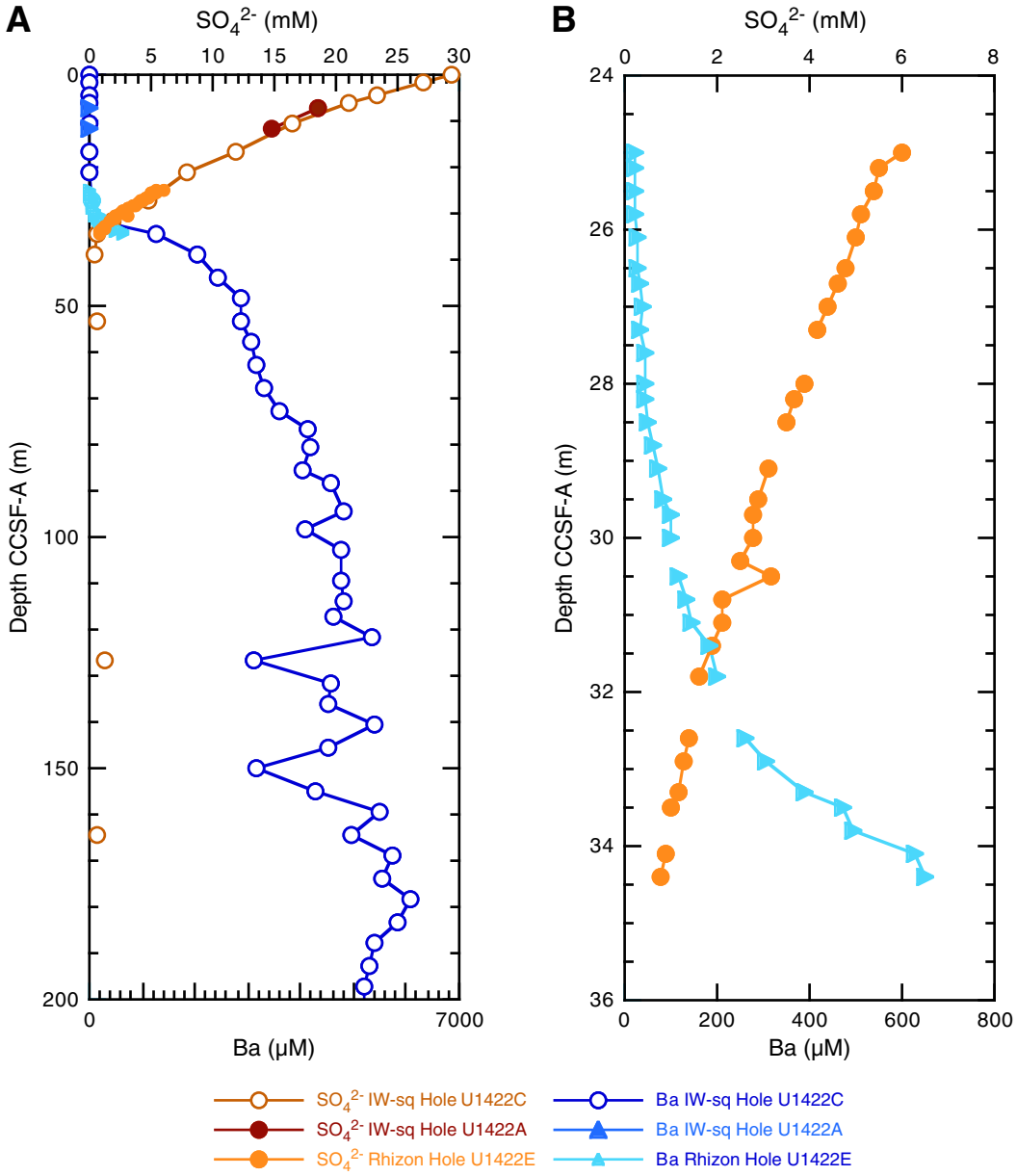

Figure F29. Dissolved calcium, magnesium, and strontium profiles, Site U1422. Note the depth of the sulfate–methane transition (SMT) at ~35 m CSF-A.

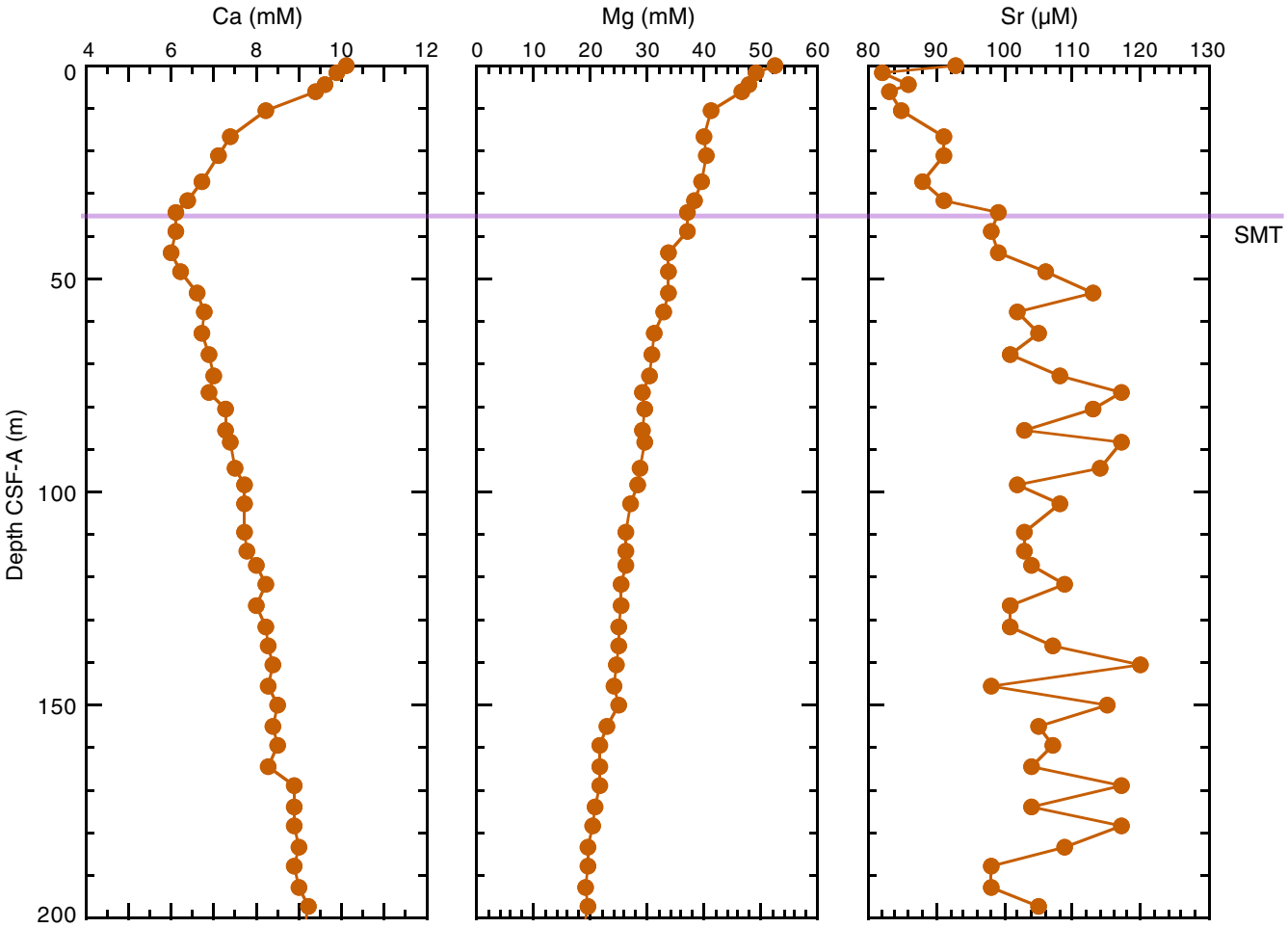

Figure F30. Dissolved lithium and boron profiles, Site U1422.

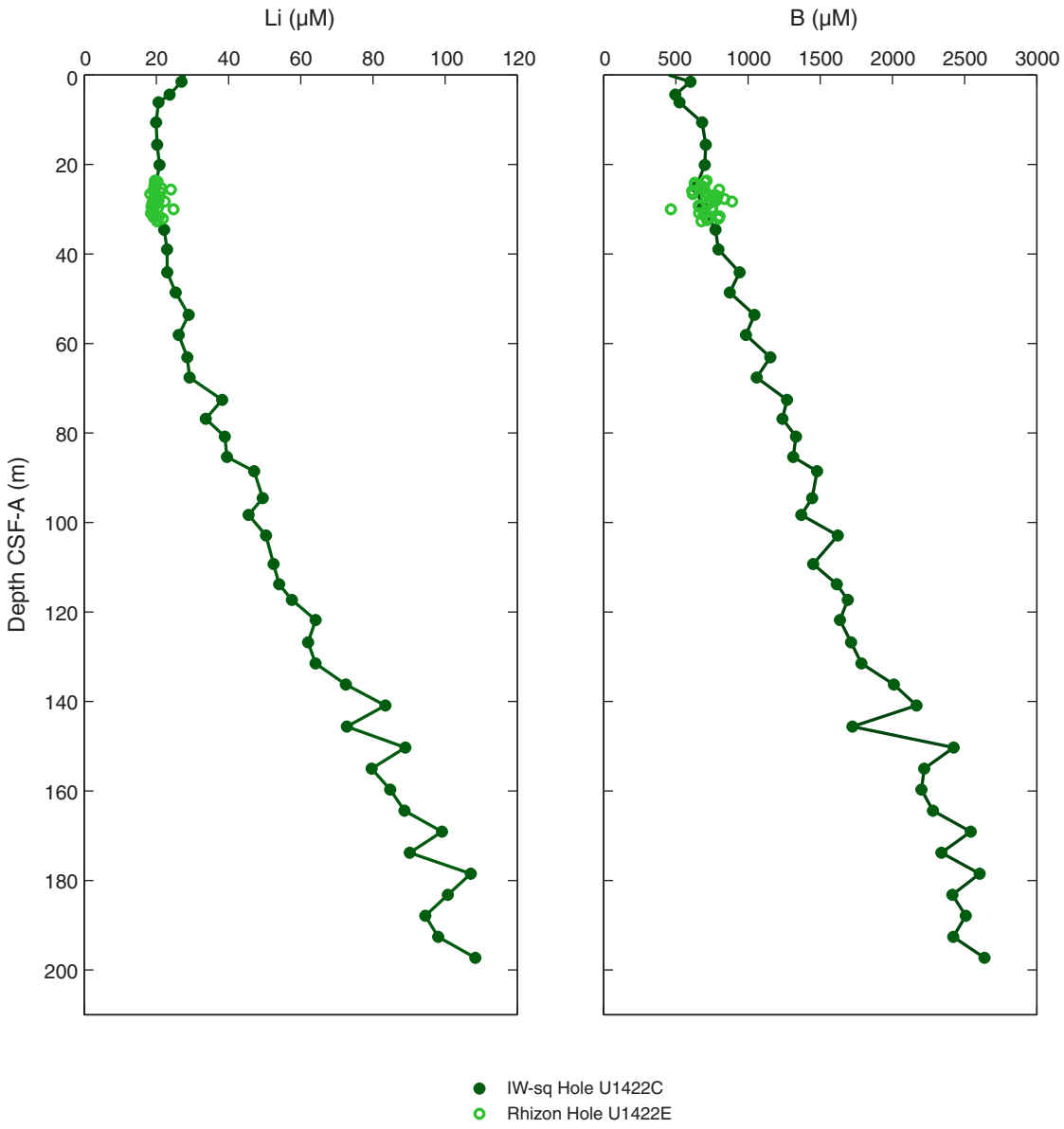

Figure F31. Dissolved silica concentrations at Site U1422 measured from spectrophotometer (spec) and inductively coupled plasma–atomic emission spectroscopy (ICP-AES). Si profiles from the two techniques match fairly well.

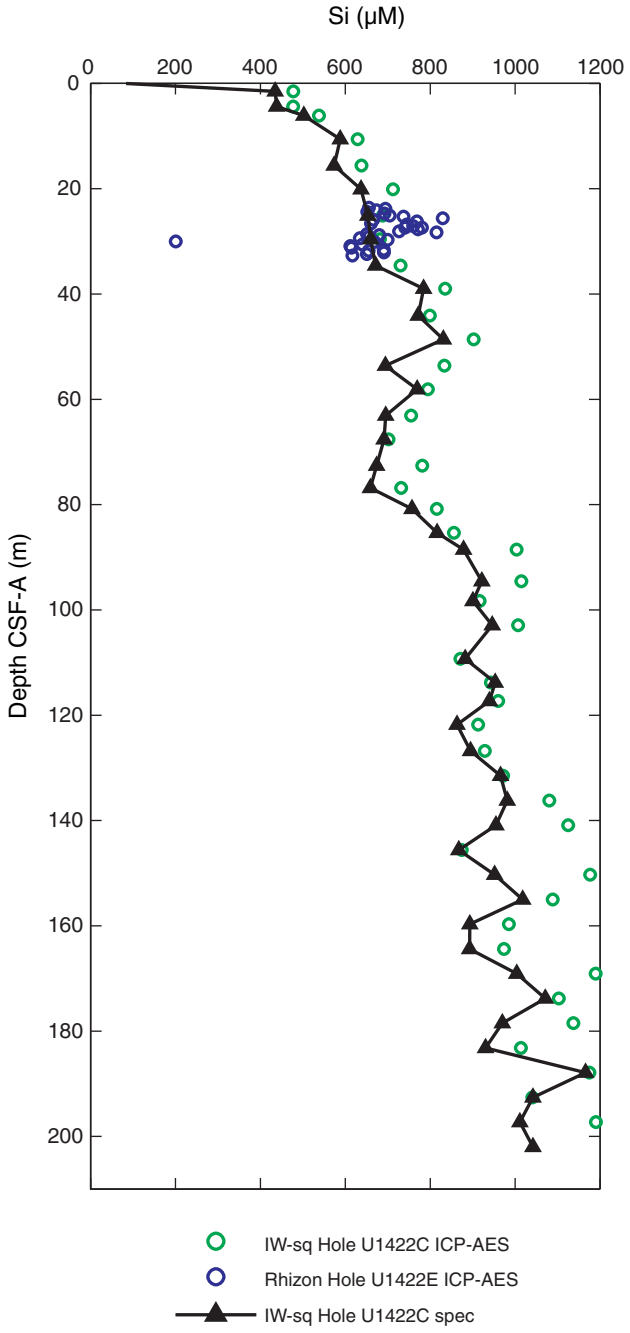

Figure F32. Paleomagnetism after 20 mT AF demagnetization, Site U1422. Chron column: black = normal polarity, white = reversed polarity, gray = zones or polarity boundaries without clear magnetostratigraphic interpretation. Inclination column: thin black dashed lines = expected geocentric axial dipole inclinations at the site latitude during reversed (left) and normal (right) polarities. Declination column: gray dots = measured declination values, green dots = declination values corrected using core orientation data collected by the FlexIT tool. Susceptibility column: SHMSL and WRMSL measured values are shown in magenta and gray dots, respectively. **A.** Hole U1422A. (Continued on next four pages.)

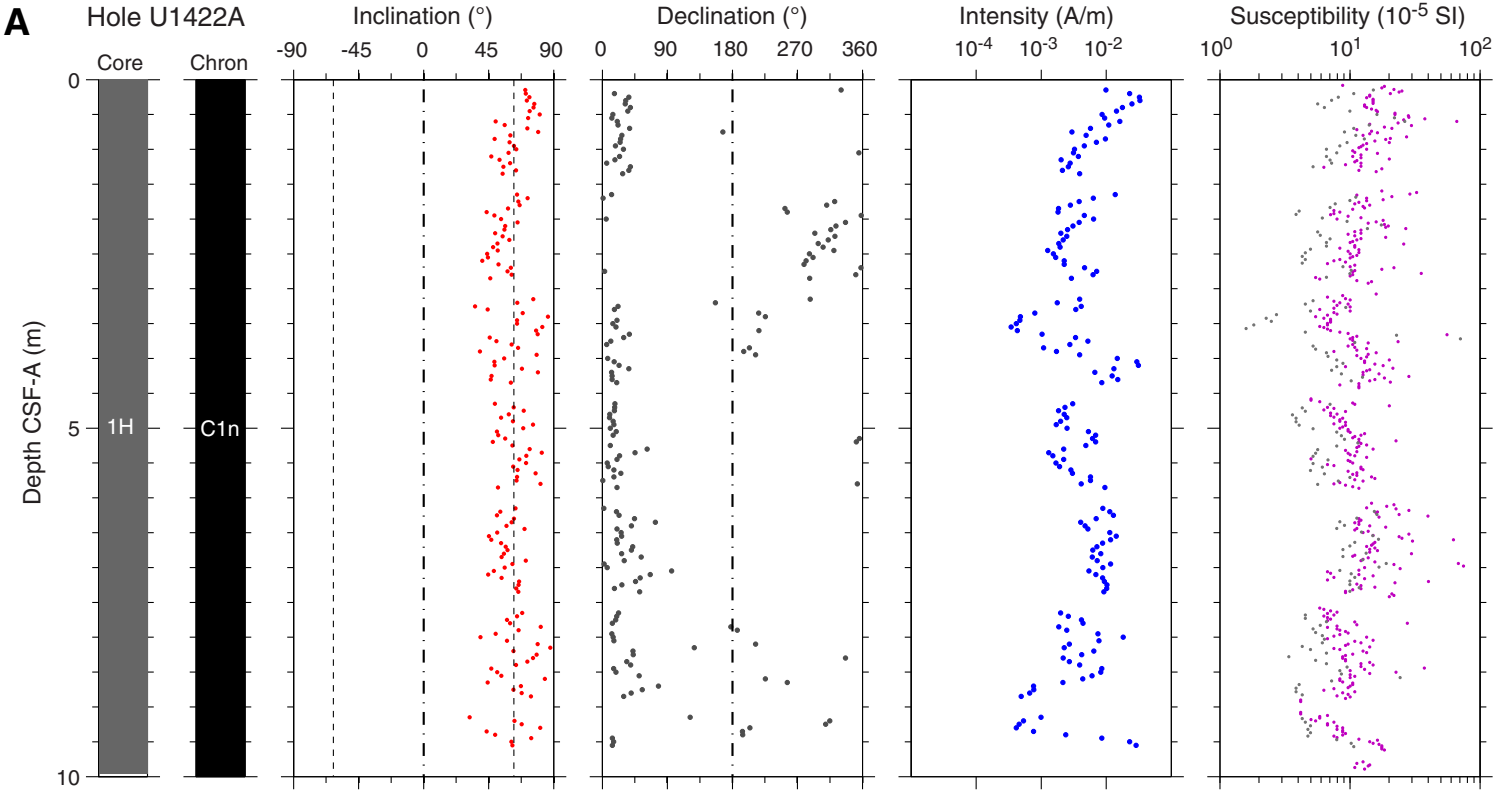

Figure F32 (continued). B. Hole U1422B. (Continued on next page.)

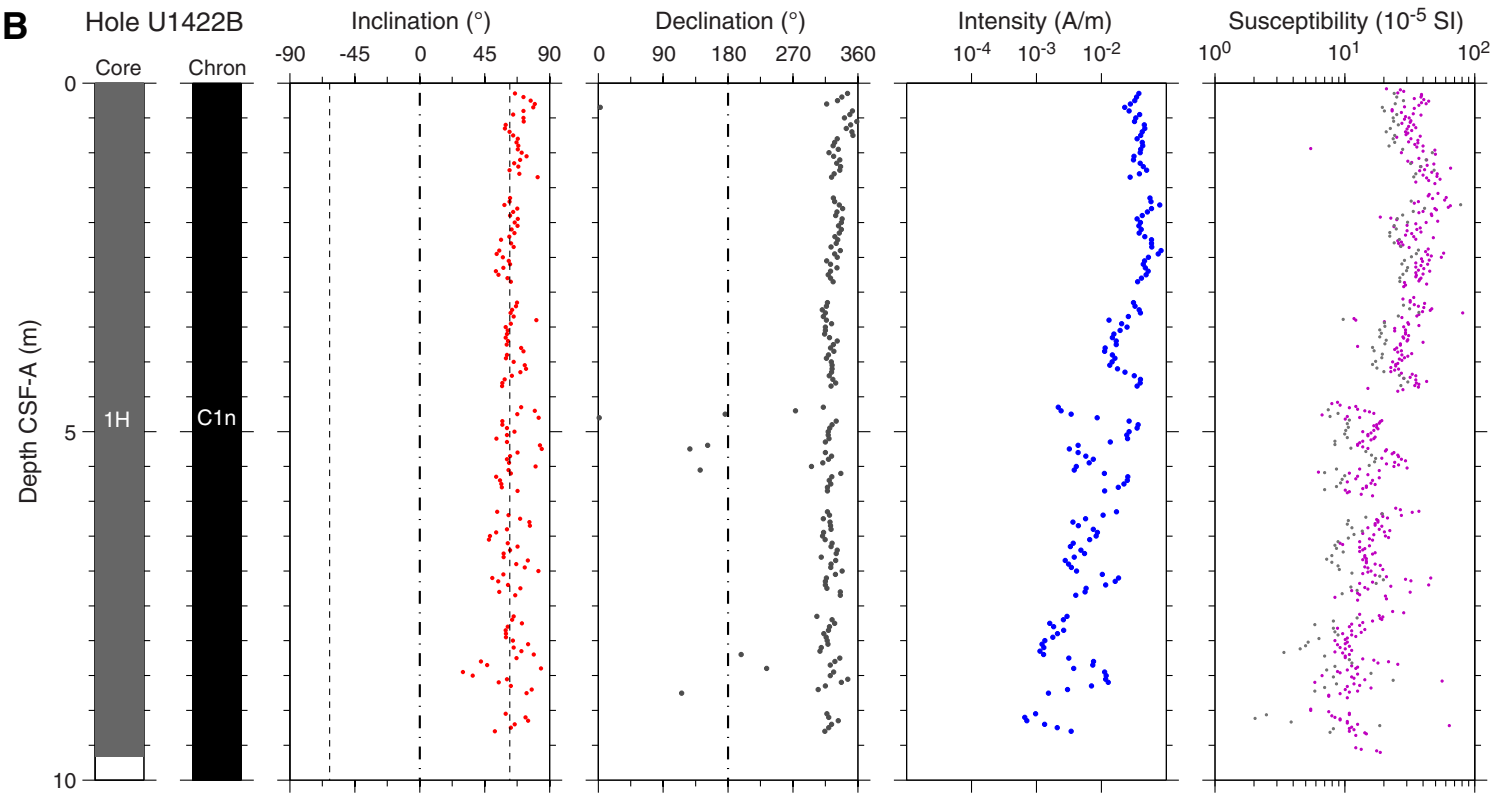

Figure F32 (continued). C. Hole U1422C. Triangles along the left side of inclination column mark depths where discrete paleomagnetic cube samples were collected (orange = discrete samples measured during the expedition). (Continued on next page.)

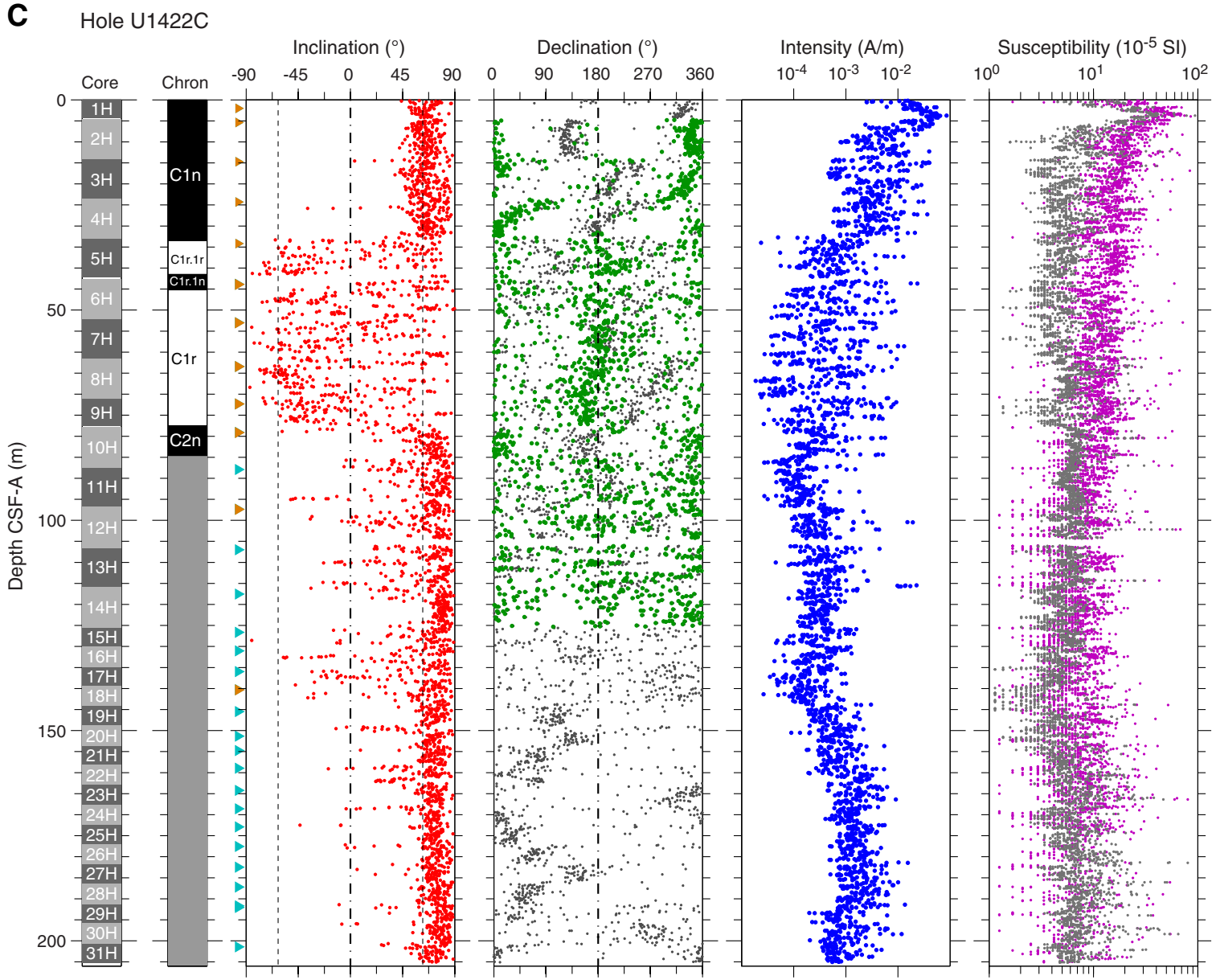

Figure F32 (continued). D. Hole U1422D. (Continued on next page.)

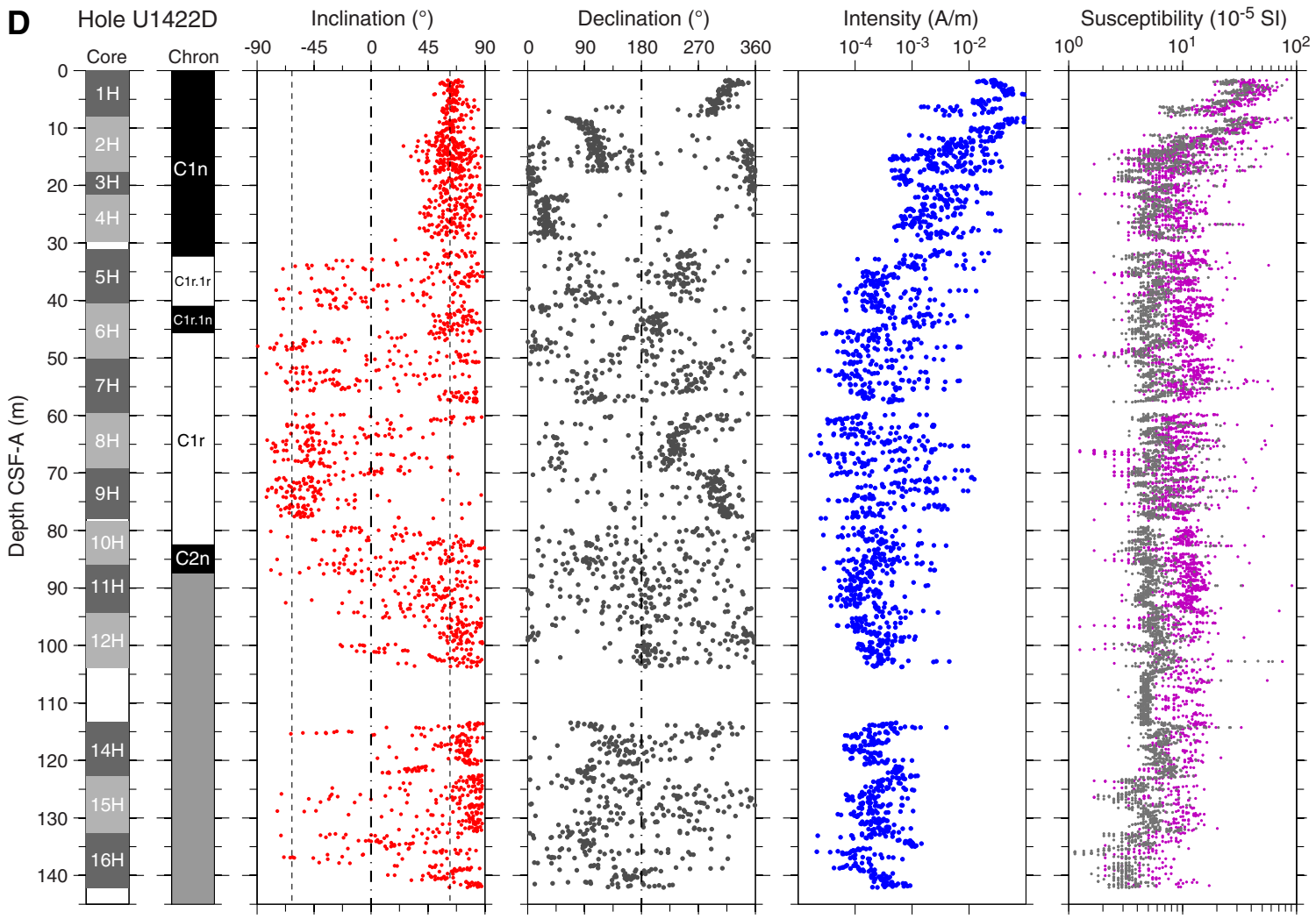

Figure F32 (continued). E. Hole U1422E.

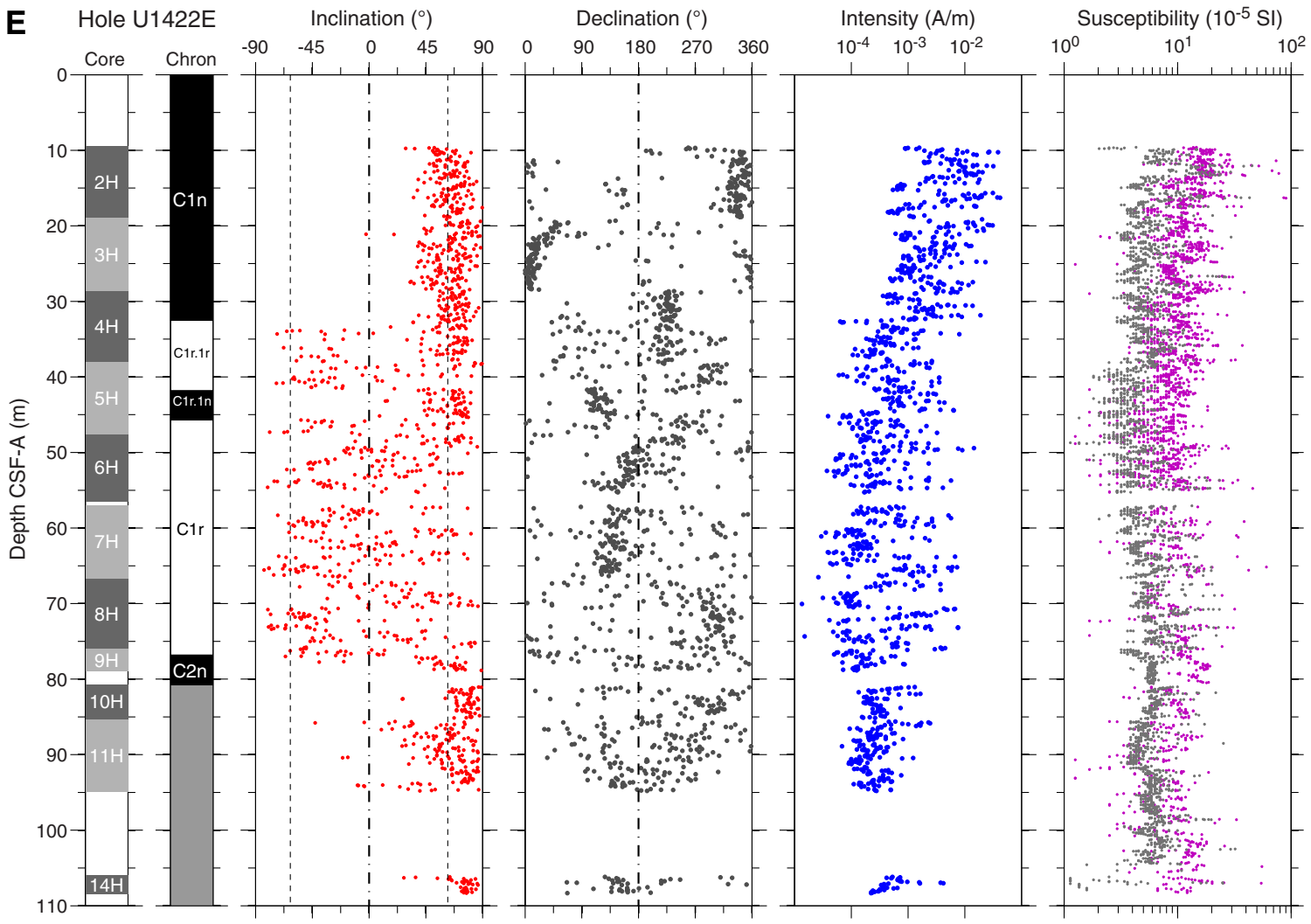

Figure F33. A–H. AF demagnetization results for eight discrete samples, Hole U1422C. For each sample, the left plot shows the intensity variation with progressive demagnetization. The middle and right plots show the NRM vector measured after each demagnetization treatment on an orthogonal projection (Zijderveld) and on an equal area projection, respectively. In the orthogonal projection plot, squares = horizontal projections, circles = vertical projections. In the equal area projection plot, solid circles = projection data with positive inclinations, open circles = projection data with negative inclinations. Note that on the orthogonal projection (Zijderveld) plot, NRM data before demagnetization have been removed to better display the demagnetized data.

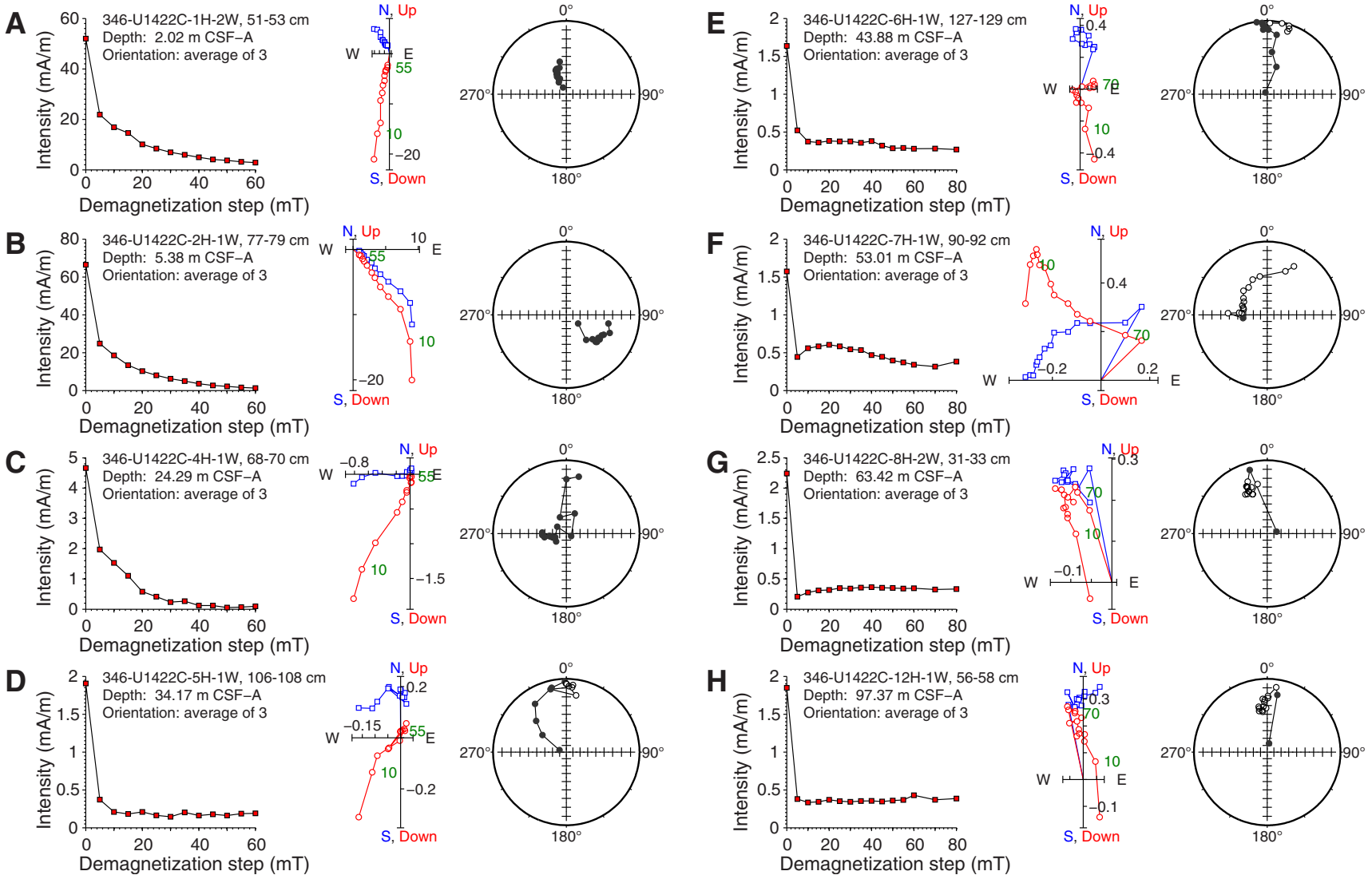

Figure F34. Suite of physical properties measured in Hole U1422C. The first magnetic susceptibility panel shows WRMSL data, whereas the second panel shows WRMSL (black) and point SHMSL (green) data. Gamma ray attenuation (GRA) bulk density is from the WRMSL. *P*-wave velocity shows WRMSL (small dots) and gantry data (solid circles = *x*-axis, open circles = *z*-axis). NGR = natural gamma radiation.

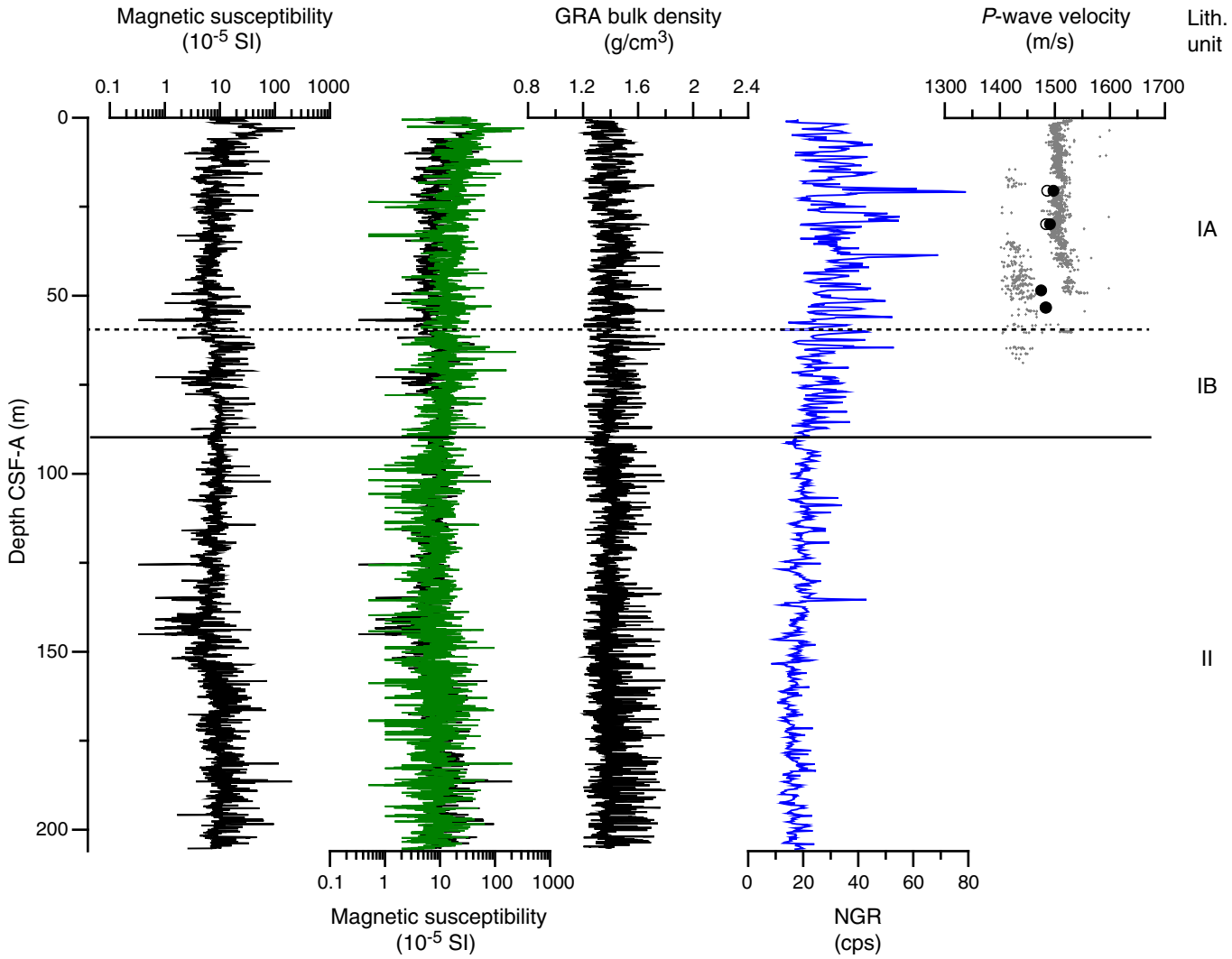

Figure F35. Discrete bulk density, grain density, porosity, water content, and shear strength, Site U1422.

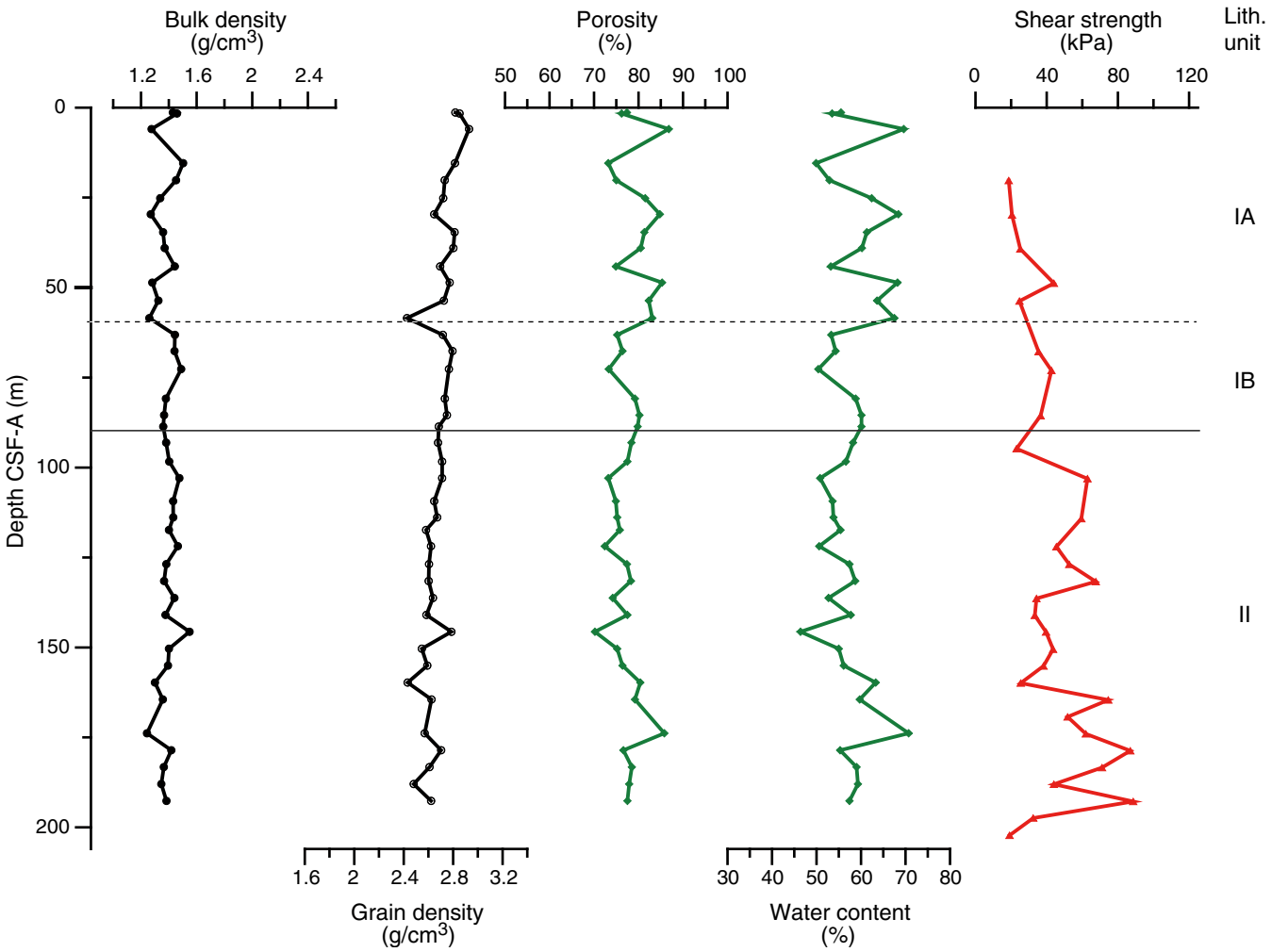

Figure F36. Relationship between lightness (L*) (black) as proxy for lithology, gamma ray attenuation (GRA) density, and natural gamma radiation (NGR), Site U1422. Red dashed lines indicate massive dark organic-rich layers that appear to drive up both GRA bulk density and NGR values. Arrow indicates a contrary example.

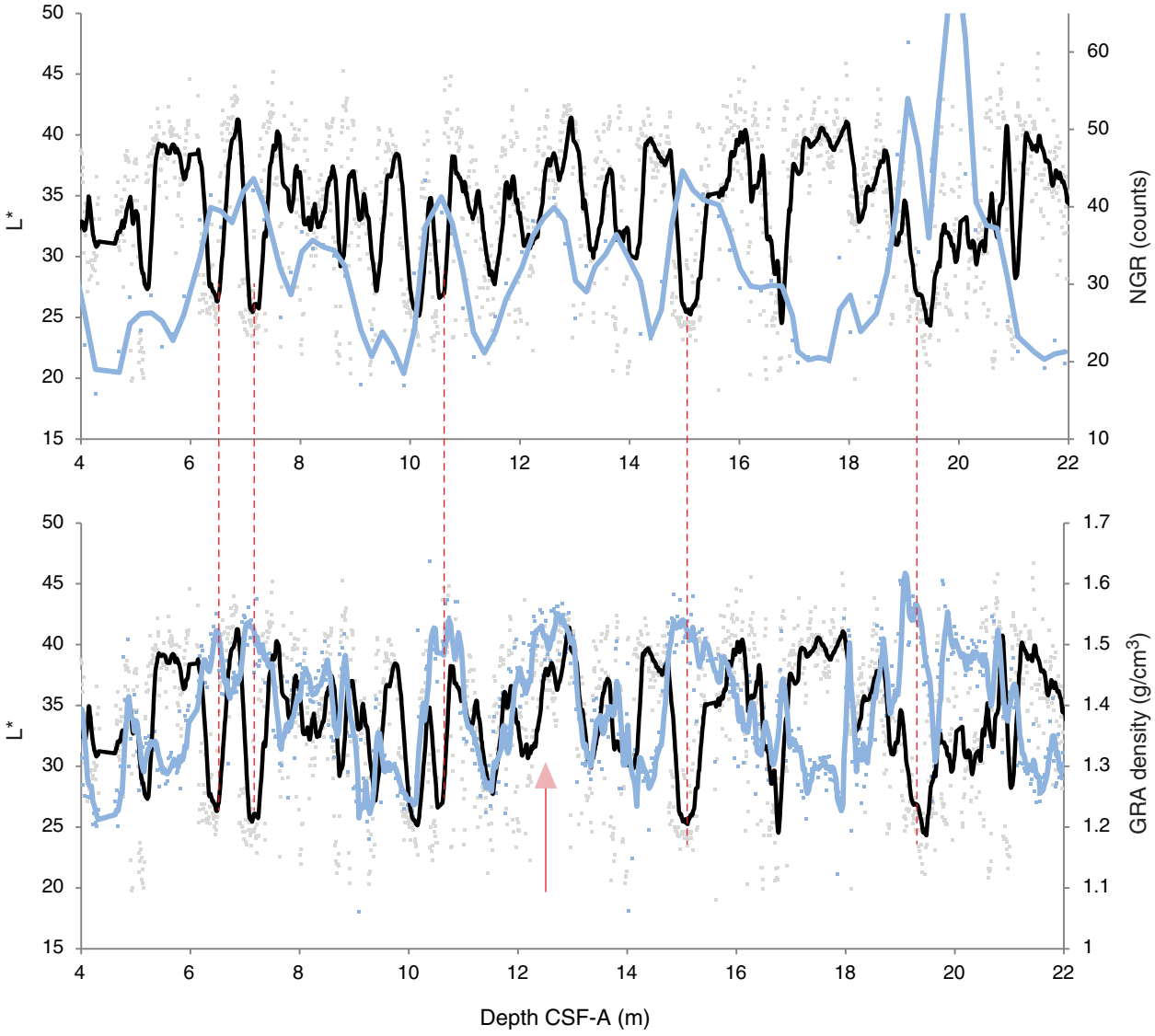

Figure F37. Color reflectance data, Hole U1422C.

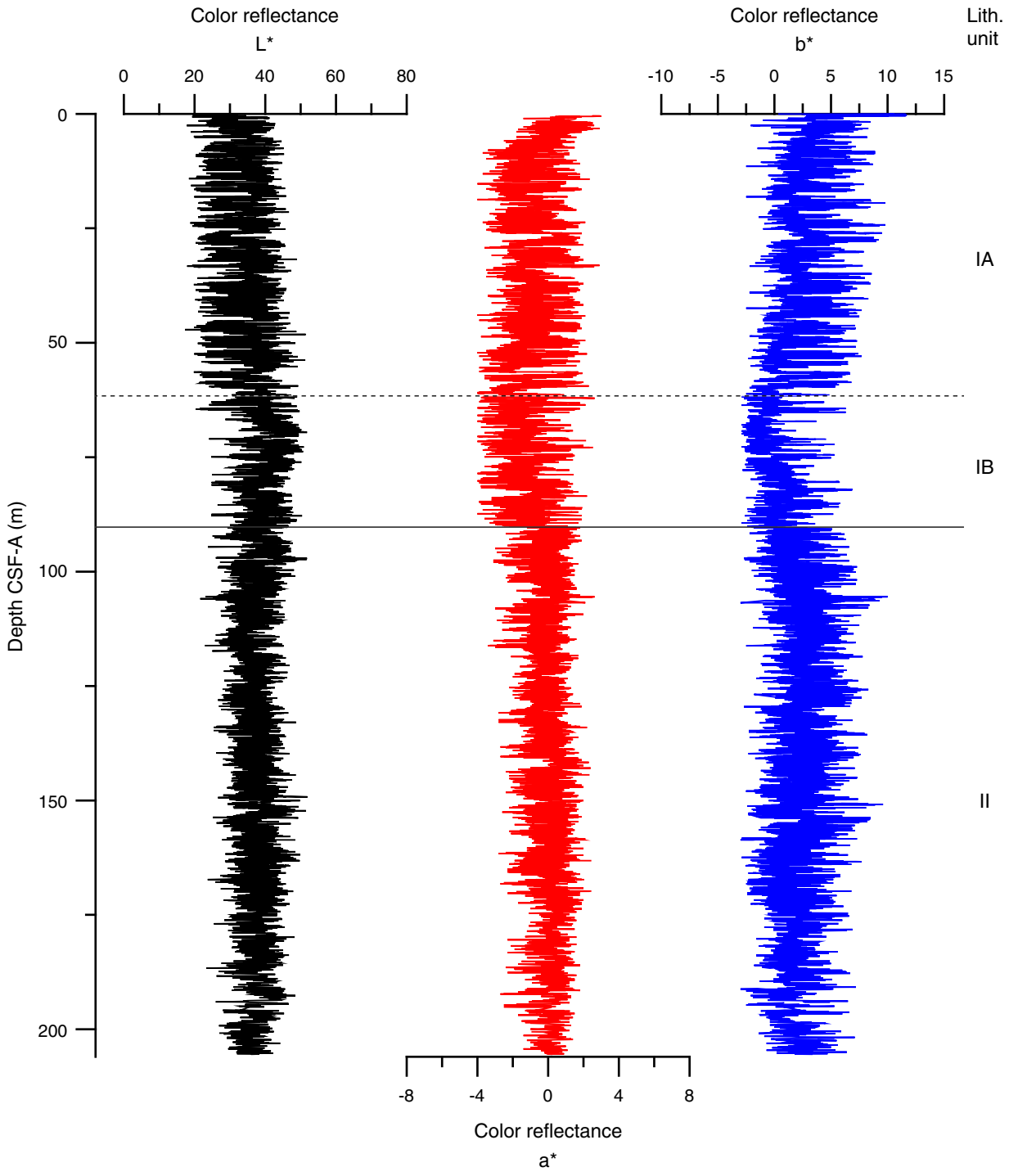

Figure F38. Plots of heat flow calculations, Hole U1422C. **A.** In situ sediment temperatures from advanced piston corer temperature tool (APCT-3) measurements with average values for Cores 346-U1422C-4H, 7H, 10H, and 13H (circles) and linear fit. **B.** In situ thermal conductivity data (squares) with calculated thermal resistance (solid line). **C.** Bullard plot of heat flow calculated from a linear fit of temperature vs. thermal resistance data.

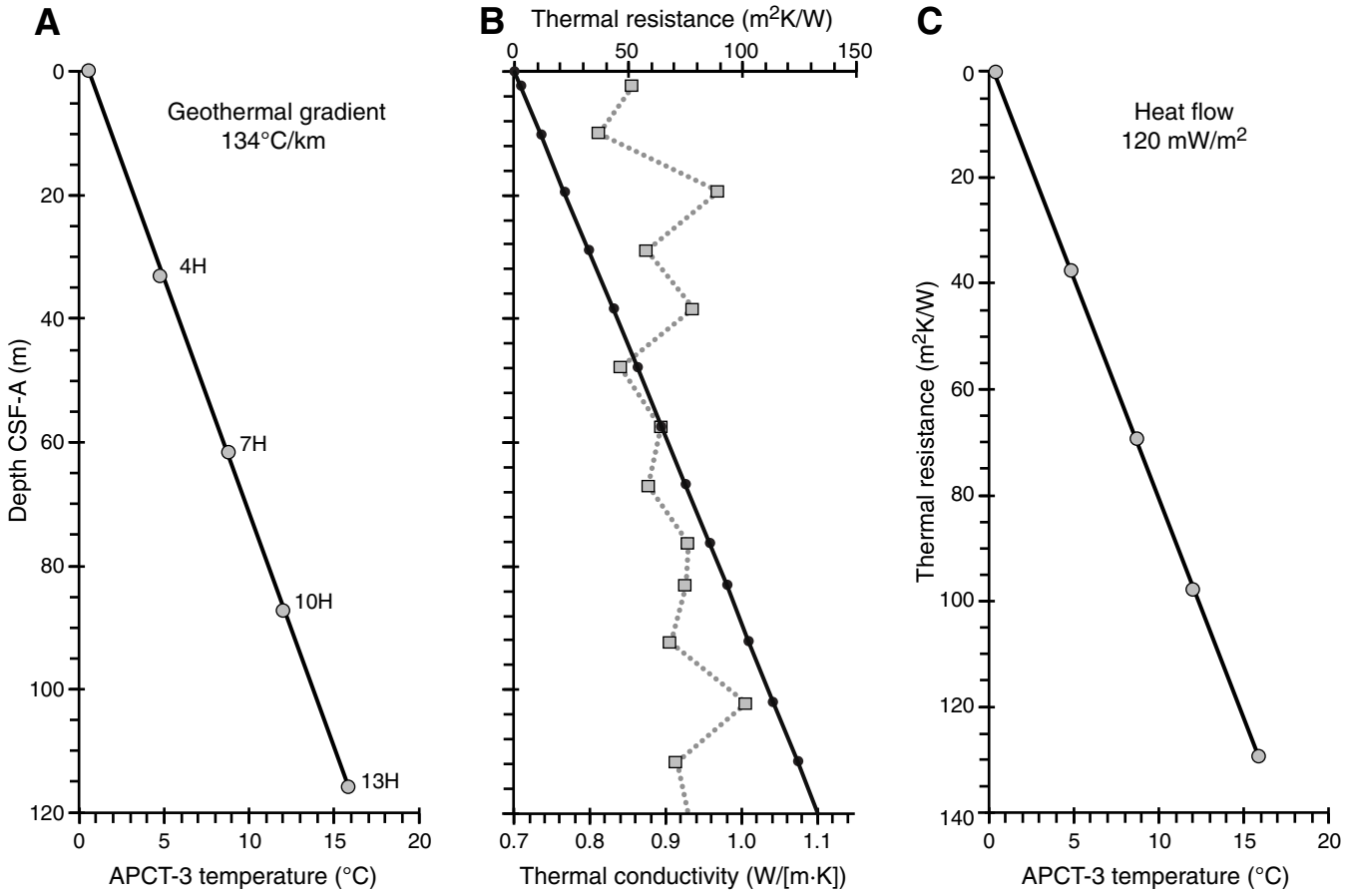

Figure F39. An example of correlation between Holes U1422C and U1422D. B = blue, MS = magnetic susceptibility.

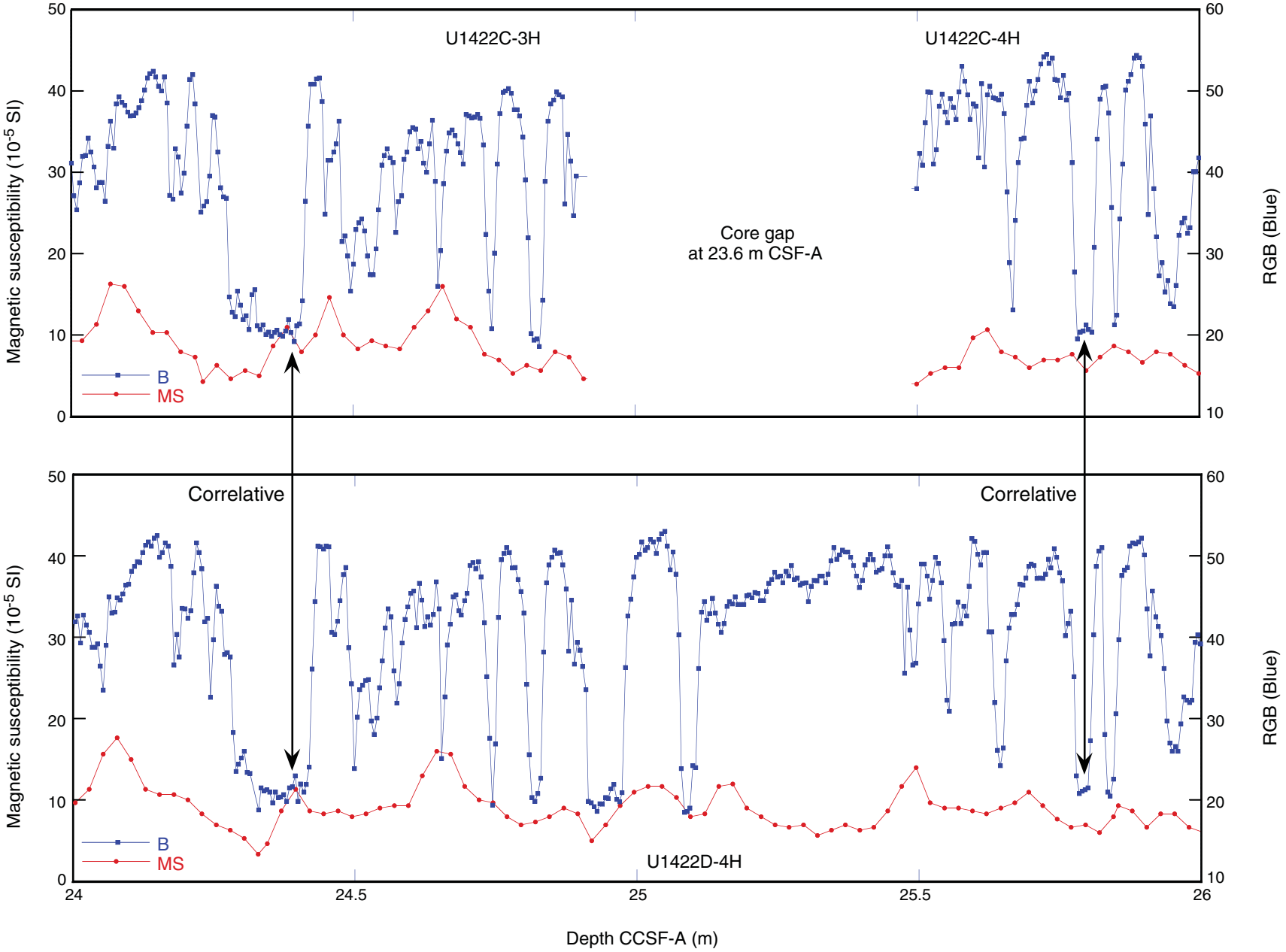

Figure F40. Alignment of all the cores from Holes U1422A (red), U1422B (purple), U1422C (green), U1422D (orange), and U1422E (magenta) illustrated using natural gamma radiation (NGR). Spliced profile (black) is also shown. The CCSF-D depth scale applies only to segments used in the splice.

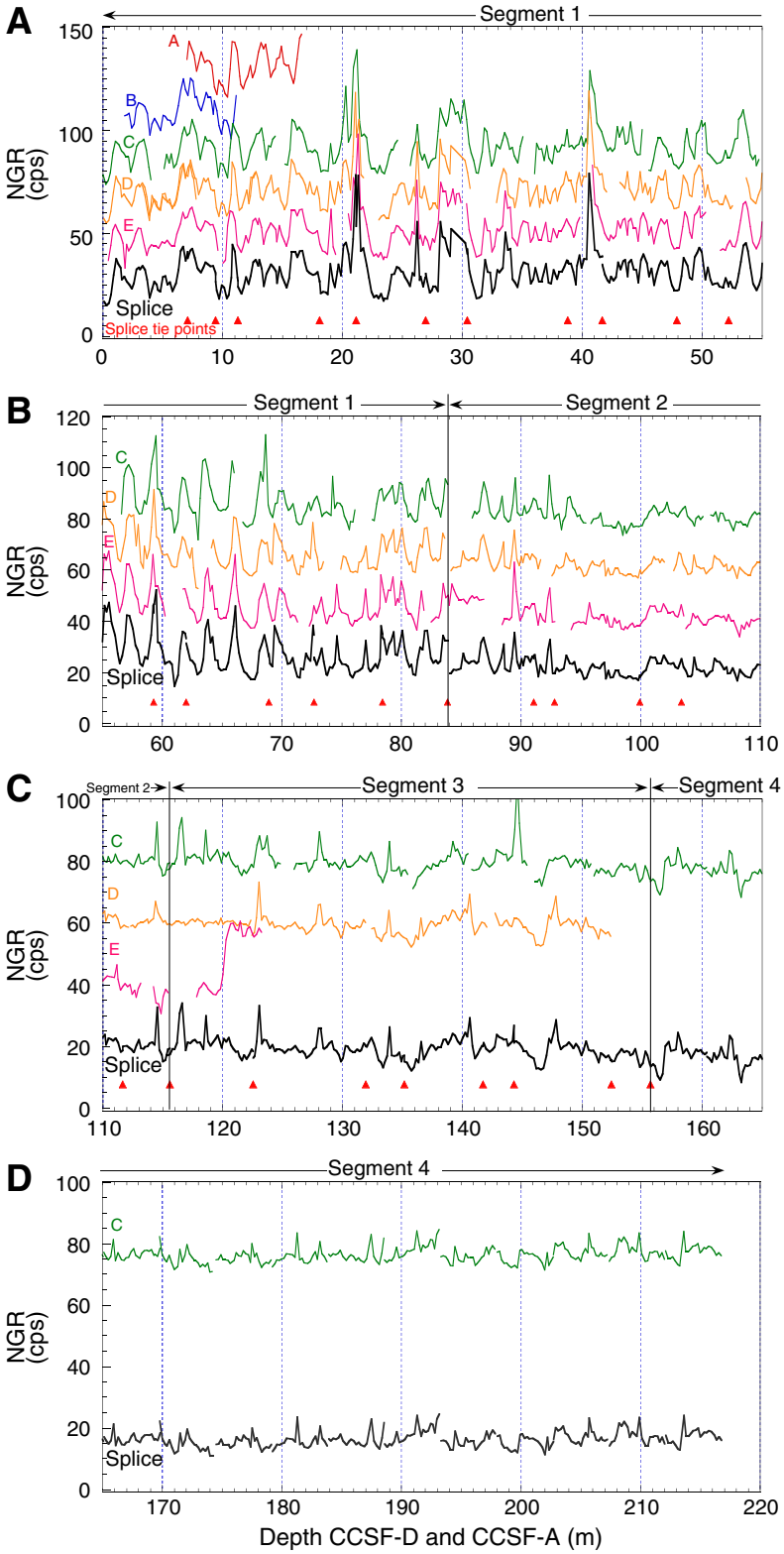

Figure F41. Age model and sedimentation rates, Site U1422. **A.** Synthesis of biostratigraphic and paleomagnetic age control points with most likely depth-age relationship lines to establish a preliminary age model. **B.** Average sedimentation rates between selected tie points for depth-age relationship plotted with gamma ray attenuation (GRA) density.

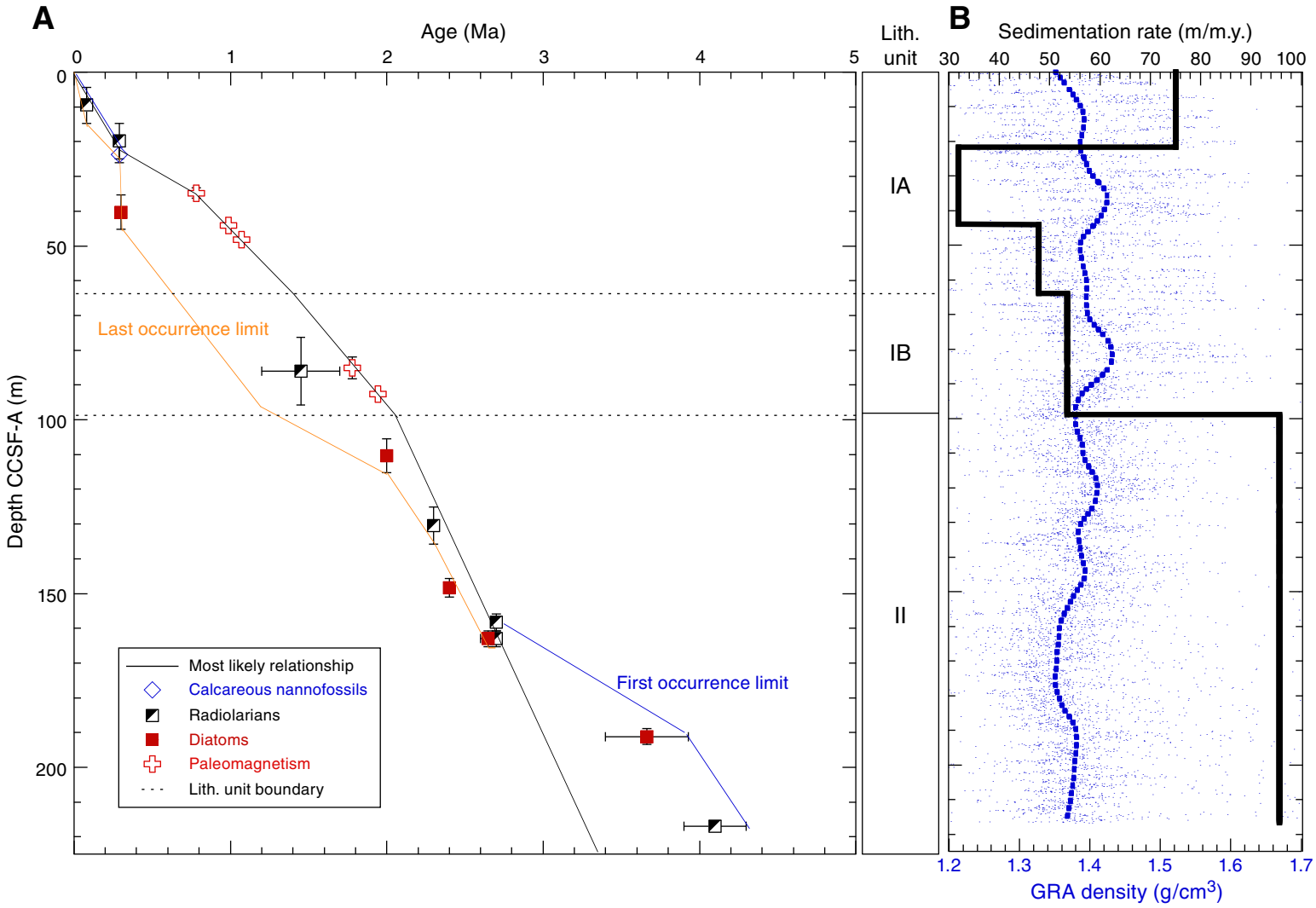

Table T1. Coring summary, Site U1422. (Continued on next two pages.)

Hole U1422A
Latitude: 43°45.9903′N
Longitude: 138°49.9894′E
Water depth (m): NA (missed mudline)
Date started (UTC): 0548 h 17 August 2013
Date finished (UTC): 1845 h 17 August 2013
Time on hole (days): 0.54
Seafloor depth (drill pipe measurement below rig floor, m DRF): Spud core recovered full—no mudline established
Distance between rig floor and sea level (m): NA
Penetration DSF (m): 9.5
Cored interval (m): 9.5
Recovered length (m): 9.96
Recovery (%): 105
Drilled interval (m): NA
Drilled interval: 0
Total cores: 1
APC cores: 1
XCB cores: 0
RCB cores: 0
Other cores: 0

Hole U1422B
Latitude: 43°45.9981′N
Longitude: 138°49.9910′E
Water depth (m): NA (missed mudline)
Date started (UTC): 1845 h 17 August 2013
Date finished (UTC): 2020 h 17 August 2013
Time on hole (days): 0.07
Seafloor depth (drill pipe measurement below rig floor, m DRF): Spud core recovered full—no mudline established
Distance between rig floor and sea level (m): NA
Penetration DSF (m): 9.5
Cored interval (m): 9.5
Recovered length (m): 9.67
Recovery (%): 102
Drilled interval (m): NA
Drilled interval: 0
Total cores: 1
APC cores: 1
XCB cores: 0
RCB cores: 0
Other cores: 0

Hole U1422C
Latitude: 43°45.9816′N
Longitude: 138°49.9897′E
Water depth (m): 3428.91
Date started (UTC): 2020 h 17 August 2013
Date finished (UTC): 1050 h 19 August 2013
Time on hole (days): 1.60
Seafloor depth (drill pipe measurement below rig floor, m DRF): 3440.3
Distance between rig floor and sea level (m): 11.39
Penetration DSF (m): 205.2
Cored interval (m): 205.2
Recovered length (m): 215.78
Recovery (%): 105
Drilled interval (m): NA
Drilled interval: 0
Total cores: 31
APC cores: 31
XCB cores: 0
RCB cores: 0
Other cores: 0

Hole U1422D
Latitude: 43°45.9899′N
Longitude: 138°49.9785′E
Water depth (m): 3428.46
Date started (UTC): 1050 h 19 August 2013
Date finished (UTC): 0335 h 20 August 2013
Time on hole (days): 0.70
Seafloor depth (drill pipe measurement below rig floor, m DRF): 3439.8
Distance between rig floor and sea level (m): 11.34
Penetration DSF (m): 141.8

Table T1 (continued). (Continued on next page.)

Cored interval (m): 141.8
Recovered length (m): 152.83
Recovery (%): 108
Drilled interval (m): NA
Drilled interval: 0
Total cores: 16
APC cores: 16
XCB cores: 0
RCB cores: 0
Other cores: 0

Hole: U1422E
Latitude: 43°45.9896′N
Longitude: 138°50.0003′E
Water depth (m): 3428.66
Date started (UTC): 0335 h 20 August 2013
Date finished (UTC): 0000 h 21 August 2013
Time on hole (days): 0.85
Seafloor depth (drill pipe measurement below rig floor, m DRF): 3440
Distance between rig floor and sea level (m): 11.34
Penetration DSF (m): 111.6
Cored interval (m): 111.6
Recovered length (m): 114.34
Recovery (%): 102
Drilled interval (m): NA
Drilled interval: 0
Total cores: 14
APC cores: 14
XCB cores: 0
RCB cores: 0
Other cores: 0

Site U1422 totals
Number of cores: 63
Penetration (m): 477.6
Cored (m): 477.6
Recovered (m): 502.58 (105.2%)

Core	Date (Aug 2013)	Time (h)	Top depth of cored interval DSF (m)	Bottom depth of cored interval DSF (m)	Interval advanced (m)	Top depth of recovered core CSF (m)	Bottom depth of recovered core CSF (m)	Length of core recovered (m)	Curated length (m)	Recovery (%)
346-U1422A-										
1H	17	1905	0.0	9.5	9.5	0.0	9.96	9.96	9.96	105
346-U1422B-										
1H	17	2045	0.0	9.5	9.5	0.0	9.67	9.67	9.67	102
346-U1422C-										
1H	17	2155	0.0	4.6	4.6	0.0	4.64	4.64	4.64	101
2H	17	2325	4.6	14.1	9.5	4.6	14.31	9.71	9.71	102
3H	18	0025	14.1	23.6	9.5	14.1	24.04	9.94	9.94	105
4H	18	0145	23.6	33.1	9.5	23.6	33.45	9.85	9.85	104
5H	18	0255	33.1	42.6	9.5	33.1	42.51	9.41	9.41	99
6H	18	0400	42.6	52.1	9.5	42.6	52.29	9.69	9.69	102
7H	18	0530	52.1	61.6	9.5	52.1	62.17	10.07	10.07	106
8H	18	0640	61.6	71.1	9.5	61.6	71.43	9.83	9.83	103
9H	18	0745	71.1	77.8	6.7	71.1	77.83	6.73	6.73	100
10H	18	0935	77.8	87.3	9.5	77.8	87.83	10.03	10.03	106
11H	18	1100	87.3	96.8	9.5	87.3	97.05	9.75	9.75	103
12H	18	1235	96.8	106.3	9.5	96.8	106.85	10.05	10.05	106
13H	18	1430	106.3	115.8	9.5	106.3	116.23	9.93	9.93	105
14H	18	1550	115.8	125.3	9.5	115.8	125.75	9.95	9.95	105
15H	18	1725	125.3	130.0	4.7	125.3	130.35	5.05	5.05	107
16H	18	1835	130.0	134.7	4.7	130.0	135.12	5.12	5.12	109
17H	18	1950	134.7	139.4	4.7	134.7	139.82	5.12	5.12	109
18H	18	2105	139.4	144.1	4.7	139.4	144.46	5.06	5.06	108
19H	18	2200	144.1	148.8	4.7	144.1	149.24	5.14	5.14	109
20H	18	2255	148.8	153.5	4.7	148.8	153.87	5.07	5.07	108
21H	19	0005	153.5	158.2	4.7	153.5	158.65	5.15	5.15	110
22H	19	0145	158.2	162.9	4.7	158.2	163.21	5.01	5.01	107
23H	19	0245	162.9	167.6	4.7	162.9	167.89	4.99	4.99	106
24H	19	0340	167.6	172.3	4.7	167.6	172.64	5.04	5.04	107
25H	19	0430	172.3	177.0	4.7	172.3	177.39	5.09	5.09	108

Table T1 (continued).

Core	Date (Aug 2013)	Time (h)	Top depth of cored interval DSF (m)	Bottom depth of cored interval DSF (m)	Interval advanced (m)	Top depth of recovered core CSF (m)	Bottom depth of recovered core CSF (m)	Length of core recovered (m)	Curated length (m)	Recovery (%)
26H	19	0520	177.0	181.7	4.7	177.0	182.03	5.03	5.03	107
27H	19	0610	181.7	186.4	4.7	181.7	186.7	5.00	5.00	106
28H	19	0700	186.4	191.1	4.7	186.4	191.57	5.17	5.17	110
29H	19	0750	191.1	195.8	4.7	191.1	196.06	4.96	4.96	106
30H	19	0845	195.8	200.5	4.7	195.8	200.95	5.15	5.15	110
31H	19	0940	200.5	205.2	4.7	200.5	205.55	5.05	5.05	107
				Total advanced:	205.2		Total recovered:	215.78		
346-U1422D-										
1H	19	1250	0.0	8.1	8.1	0.0	8.14	8.14	8.14	100
2H	19	1330	8.1	12.1	4.0	8.1	17.87	9.77	9.77	244
3H	19	1445	12.1	21.6	9.5	12.1	22.09	9.99	9.99	105
4H	19	1540	21.6	31.1	9.5	21.6	30.05	8.45	8.45	89
5H	19	1635	31.1	40.6	9.5	31.1	40.75	9.65	9.65	102
6H	19	1725	40.6	50.1	9.5	40.6	50.40	9.80	9.80	103
7H	19	1820	50.1	59.6	9.5	50.1	59.84	9.74	9.74	103
8H	19	1905	59.6	69.1	9.5	59.6	69.40	9.80	9.80	103
9H	19	1955	69.1	78.3	9.2	69.1	78.35	9.25	9.25	101
10H	19	2115	78.3	84.8	6.5	78.3	86.13	7.83	7.83	120
11H	19	2205	84.8	94.3	9.5	84.8	94.79	9.99	9.99	105
12H	19	2255	94.3	103.8	9.5	94.3	104.16	9.86	9.86	104
13H	19	2345	103.8	113.3	9.5	103.8	114.21	10.41	10.41	110
14H	20	0055	113.3	122.8	9.5	113.3	123.26	9.96	9.96	105
15H	20	0145	122.8	132.3	9.5	122.8	132.78	9.98	9.98	105
16H	20	0240	132.3	141.8	9.5	132.3	142.51	10.21	10.21	107
				Total advanced:	141.8		Total recovered:	152.83		
346-U1422E-										
1H	20	0440	0.0	9.5	9.5	0.0	9.63	9.63	9.63	101
2H	20	0535	9.5	19.0	9.5	9.5	19.13	9.63	9.63	101
3H	20	0650	19.0	28.5	9.5	19.0	28.80	9.80	9.80	103
4H	20	0740	28.5	38.0	9.5	28.5	38.38	9.88	9.88	104
5H	20	0830	38.0	47.5	9.5	38.0	47.80	9.80	9.80	103
6H	20	0925	47.5	57.0	9.5	47.5	56.73	9.23	9.23	97
7H	20	1015	57.0	66.5	9.5	57.0	66.82	9.82	9.82	103
8H	20	1105	66.5	76.0	9.5	66.5	76.45	9.95	9.95	105
9H	20	1200	76.0	80.7	4.7	76.0	80.87	4.87	4.87	104
10H	20	1250	80.7	85.4	4.7	80.7	85.51	4.81	4.81	102
11H	20	1415	85.4	94.9	9.5	85.4	95.11	9.71	9.71	102
12H	20	1505	94.9	104.4	9.5	94.9	104.82	9.92	9.92	104
13H	20	1610	104.4	106.0	1.6	104.4	106.02	1.62	1.62	101
14H	20	1715	106.0	111.6	5.6	106.0	111.67	5.67	5.67	101
				Total advanced:	111.6		Total recovered:	114.34		

DRF = drilling depth below rig floor, DSF = drilling depth below seafloor, CSF = core depth below seafloor. APC = advanced piston corer, XCB = extended core barrel, RCB = rotary core barrel. H = APC system. NA = not applicable.

Table T2. Visible tephra layers thicker than 0.5 cm in Hole U1422C sediment.

Core, section, interval (cm)	Thickness (cm)	Color	Occurrence
346-U1422C-			
1H-2, 147–150	3.0	Gray	Layered
2H-1, 24.5–25.5	1.0	Gray	Layered
2H-1, 119–120.5	1.5	Gray	Layered
2H-2, 7.5–9	1.5	Gray	Layered
2H-4, 105–107	2.0	Dark gray	Layered
2H-4, 128–131	3.0	Dark gray	Layered
2H-5, 15–16	1.0	Light gray	Layered
2H-7, 12–13.5	1.5	Gray	Layered
2H-7, 55–55.5	0.5	Gray	Layered
3H-5, 58.5–59	0.5	Gray	Layered
3H-5, 88.2–89.2	1.0	Light gray	Layered
3H-6, 17.5–18.5	1.0	Light gray	Layered
3H-6, 127.5–128.5	1.0	Gray	Layered
3H-7, 30–30.6	0.6	Dark gray	Layered
4H-1, 11–12	1.0	Gray	Layered
4H-2, 29–29.5	0.5	Gray	Layered
4H-3, 34.7–35.5	0.8	Light brownish gray	Layered
4H-4, 50.5–52	1.5	Dark brownish gray	Layered
4H-6, 8.5–9.8	1.3	White	Layered
4H-6, 37.5–38	0.5	White	Layered
4H-6, 48.5–49.5	1.0	White	Layered
5H-3, 108–109	1.0	White	Layered
5H-4, 55.5–63.5	8.0	Light gray	Layered
5H-5, 7.8–9.1	1.3	White	Layered
5H-5, 17.5–18.5	1.0	White	Layered
5H-5, 51–52	1.0	White	Blocked
5H-5, 71.7–72	0.8	Dark brownish gray	Layered
5H-5, 89.5–91.5	2.0	White	Layered
5H-5, 95–96	1.0	Light gray	Layered
5H-5, 104.2–105	0.8	Light gray	Layered
5H-5, 123.8–124.5	0.7	Light gray	Layered
5H-6, 102.3–103.1	0.8	Gray	Layered
5H-7, 0–2.5	2.5	White	Layered
6H-1, 38–40	2.0	Light gray	Layered
6H-1, 88.2–90	0.8	White	Layered
6H-1, 103.5–104	0.5	Dark gray	Layered
6H-2, 46.6–47.2	0.6	White	Layered
6H-2, 89–90	1.0	Light gray	Layered
6H-4, 108.5–112	13.5	White	Layered
6H-5, 105–106.5	1.5	Gray	Layered
6H-5, 125.5–126.5	1.5	White	Layered
6H-6, 98–99	1.0	White	Layered
7H-2, 17–18.5	1.5	White	Layered
7H-2, 44–46	2.0	White	Layered
7H-2, 110.5–111.2	0.7	Light gray	Layered
7H-2, 116.8–117.5	0.7	Light gray	Layered
7H-2, 119–119.5	0.5	Light gray	Layered
7H-2, 120.5–121.2	0.7	Light gray	Layered
7H-2, 122–123.2	1.2	Light gray	Layered
7H-2, 124–129	2.5	Light gray	Patched
7H-3, 144–154.5	10.5	Light gray	Layered
7H-5, 6.2–7.7	1.5	White	Layered
7H-5, 134–135	1.0	White	Layered
8H-2, 77–77.5	0.5	White	Layered
8H-2, 116.5–117.5	1.0	Light gray	Layered
8H-4, 62.3–63	0.7	White	Layered
8H-5, 125–126	1.0	White	Layered
9H-1, 72.5–73	0.5	Light gray	Layered
9H-1, 136.2–137.5	1.3	Brownish gray	Layered
9H-2, 27–33.5	6.5	White	Layered
9H-2, 35–36	1.0	Dark gray	Layered
9H-2, 74.5–76.5	2.0	Light gray	Layered
9H-3, 23–24	1.0	Light gray	Layered
9H-3, 25.5–57	31.5	Light gray	Layered
9H-3, 59–70.5	11.5	White	Layered
9H-3, 70.5–79.2	8.7	Dark gray	Layered
9H-3, 93–105	12.0	Gray	Layered
9H-3, 146–149	3.0	Dark brownish gray	Layered
9H-CC, 4.5–5	0.5	Light gray	Layered
10H-1, 40–40.5	0.5	Gray	Layered
10H-2, 98–99.5	1.5	Light gray	Layered
10H-2, 100–126	26.0	Dark gray	Layered
10H-3, 59.5–73	13.5	Light gray	Layered
10H-3, 140–141	1.0	Gray	Layered
10H-4, 16–18	0.7	Gray	Patched
10H-4, 110–116	6.0	White	Layered
10H-5, 46–48	2.0	Gray	Layered
10H-5, 51–60	9.0	Gray	Layered
10H-7, 35–37.5	2.5	Light gray	Layered
13H-1, 114–141	27.0	White	Layered
13H-6, 115–116	1.0	Light gray	Layered
14H-2, 67–78	1.0	White	Patched
18H-2, 25.8–26.5	0.7	White	Layered
18H-3, 34–35	1.0	White	Layered
18H-3, 46–47	1.0	Light gray	Layered
20H-1, 122–125	3.0	Light gray	Layered
26H-2, 134–136.5	2.5	White	Layered
26H-3, 23–23.5	0.5	White	Layered

Table T3. XRD analysis of bulk samples, Site U1422.

Core section, interval (cm)	Top depth CSF-A (m)	Smectite (counts)	Illite (counts)	Kaolinite + chlorite (counts)	Opal-A (counts)	Quartz (counts)	K-feldspar (counts)	Plagioclase (counts)	Calcite (counts)	Halite (counts)	Pyrite (counts)
346-U1422A-											
1H-1, 70.0–71.0	0.7	169	447	303	0	5298	275	784	0	290	0
346-U1422B-											
1H-1, 51.0–52.0	0.51	229	521	401	0	5202	256	2383	0	269	0
346-U1422C-											
1H-2, 50.0–51.0	2	228	427	359	0	5271	203	702	0	287	64
1H-3, 6.5–7.5	3.065	156	338	258	0	4302	219	582	0	268	0
2H-1, 76.0–77.0	5.36	155	225	181	22	4309	220	606	0	336	0
2H-2, 88.0–89.0	6.98	235	576	361	10	4636	186	728	0	185	546
2H-4, 88.0–89.0	9.98	104	94	105	79	2294	213	333	0	637	177
3H-1, 59.0–60.0	14.69	197	380	227	28	4469	200	656	0	270	0
4H-1, 67.0–68.0	24.27	228	509	288	24	4952	209	717	0	257	0
5H-1, 104.0–105.0	34.14	172	366	193	20	4710	193	809	0	234	0
6H-1, 126.0–127.0	43.86	252	390	269	26	5095	200	815	0	256	0
7H-1, 89.0–90.0	52.99	218	576	330	26	5288	248	789	0	190	0
8H-2, 34.0–35.0	63.44	142	365	224	20	4798	250	719	0	181	0
9H-1, 123.0–124.0	72.33	152	232	163	41	3263	147	533	0	218	122
10H-1, 126.0–127.0	79.06	210	334	236	14	4214	215	672	0	209	114
11H-1, 63.0–64.0	87.93	175	253	152	36	3814	198	544	0	303	60
12H-1, 55.0–56.0	97.35	177	327	203	42	4000	0	474	0	229	0
12H-6, 112.0–113.0	105.55	131	126	94	15	1274	0	147	1167	127	67
13H-1, 66.0–67.0	106.96	205	279	214	55	3779	0	650	0	253	61
14H-2, 20.0–21.0	117.5	216	274	235	59	3406	0	533	0	245	0
15H-1, 133.0–134.0	126.63	163	141	116	49	2987	0	866	0	256	88
16H-1, 102.0–103.0	131.02	160	189	177	72	3233	0	504	0	261	50
17H-1, 128.0–129.0	135.98	295	572	417	16	4535	215	612	0	258	0
18H-1, 91.0–92.0	140.31	172	203	116	91	3136	0	399	0	288	80
19H-1, 139.0–140.0	145.49	274	579	343	55	5132	239	795	0	204	0
20H-2, 101.0–102.0	151.31	203	215	165	65	2987	200	474	0	263	90
21H-1, 122.0–123.0	154.72	196	310	213	76	3210	167	491	0	305	76
22H-1, 74.0–75.0	158.94	119	192	162	138	2896	166	364	0	381	68
23H-1, 130.0–131.0	164.2	109	165	135	118	2677	150	410	0	307	64
24H-1, 98.0–99.0	168.58	125	176	115	57	2766	150	424	0	287	116
25H-1, 63.0–64.0	172.93	165	134	168	81	2994	150	424	0	292	60
26H-1, 52.0–53.0	177.52	154	264	206	125	2573	148	420	0	315	80
27H-1, 76.0–77.0	182.46	170	180	128	117	2577	165	450	0	348	84
27H-4, 15.0–16.0	185.97	123	122	92	32	1417	0	467	317	99	67
28H-1, 79.0–80.0	187.19	78	131	101	124	2294	140	389	0	347	85
29H-1, 55.0–56.0	191.65	130	183	148	65	2775	0	496	0	314	71
29H-1, 94.0–95.0	192.04	213	280	172	34	3627	0	592	0	279	48
31H-1, 92.0–93.0	201.42	120	136	112	102	2701	0	325	0	292	92

Table T4. Microfossil bioevents, Site U1422.

Core, section, interval (cm)		Event		Age	Depth CSF-A (m)				Depth CCSF-A (m)				
Top	Bottom	type	Bioevents and epoch boundaries	(Ma)	Top	Bottom	Midpoint	±	Top	Bottom	Midpoint	±	Comments
346-U1422C-	346-U1422C-												
1H-CC	2H-CC	R	LO *Amphimelissa setosa*	0.08	4.59	14.28	9.44	4.85	4.35	14.73	9.54	5.19	
2H-CC	3H-CC	R	LO *Spongodiscus* sp.	0.29	14.28	23.99	19.14	4.86	14.73	25.01	19.87	5.14	
3H-5W, 15–16	4H-1W, 59–60	CN	FO *Emiliania huxleyi*	0.29	20.25	24.19	22.22	1.97	21.27	26.17	23.72	2.45	Barren in between
4H-CC	5H-CC	D	LO *Proboscia curvirostris*	0.31	33.40	42.47	37.94	4.54	35.38	45.30	40.34	4.96	
8H-CC	10H-CC	R	LO *Axoprunum acquilonium*	1.2–1.7	71.38	87.77	79.58	8.20	76.42	95.79	86.11	9.68	Barren in between
11H-CC	12H-CC	D	LO *Neodenticula koizumii*	2.00	97.00	106.80	101.90	4.90	105.48	115.79	110.63	5.16	
13H-CC	14H-CC	R	LO *Cycladophora sakaii*	2.30	116.18	125.70	120.94	4.76	125.17	135.78	130.48	5.31	
16H-CC	17H-CC	D	FO *Neodenticula seminae*	2.40	135.07	139.77	137.42	2.35	145.75	151.03	148.39	2.64	
Pliocene/Pleistocene boundary				2.59									
18H-CC	19H-CC	R	FO *Cycladophora davisiana*	2.70	144.41	149.19	146.80	2.39	155.91	160.69	158.30	2.39	
19H-CC	20H-CC	D	LO *Neodenticula kamtschatica*	2.6–2.7	149.19	153.82	151.51	2.32	160.69	165.32	163.00	2.32	
19H-CC	20H-CC	R	LO *Hexacontium parviakitaensis*	2.70	149.19	153.82	151.51	2.32	160.69	165.32	163.00	2.32	
25H-CC	26H-CC	D	FO *Neodenticula koizumii*	3.40–3.93	177.33	181.97	179.65	2.32	188.83	193.47	191.15	2.32	

R = radiolarian, CN = calcareous nannofossil, D = diatom, LO = last occurrence, FO = first occurrence.

Table T5. Preservation and estimated abundance of calcareous nannofossils, Site U1422. (Continued on next page.)

Core, section, interval (cm)	Top depth CSF-A (m)	Bottom depth CSF-A (m)	Preservation	Abundance	*Braarudosphaera bigelowii*	*Coccolithus pelagicus*	*Emiliania huxleyi*	*Gephyrocapsa caribbeanica*	*Gephyrocapsa muellerae*	*Gephyrocapsa oceanica* s.s.	*Gephyrocapsa* spp. small (<4 µm)	*Pontosphaera* spp.	*Reticulofenestra minutula*	Comments
346-U1422A-														
1H-CC	9.71	9.71		B										
346-U1422B-														
1H-CC	9.62	9.67		B										
346-U1422C-														
1H-CC	4.59	4.64		B										
2H-CC	14.28	14.31	P	R							R			
3H-4, 126–127	19.86	19.87	G	A			A	C			D			
3H-5, 15–16	20.25	20.26	G	A		F	C	C			D			
3H-5, 29–30	20.39	20.40		B										
3H-CC	23.99	24.04		B										
4H-1, 59–60	24.19	24.20	M	C		C				R	D	R		*
4H-2, 99–100	26.09	26.10		B										
4H-5, 95–96	30.53	30.54	P	R	R	R		R			R			
4H-CC	33.40	33.45		B										
5H-4, 66–67	38.16	38.17	G	A	R			C		R	A			
5H-CC	42.47	42.51		B										
6H-3, 36–37	45.96	45.97		B										
6H-CC	52.25	52.29		B										
7H-5, 55–56	58.65	58.66		B										
7H-CC	62.10	62.17	P	R	R									
8H-7, 45–46	71.05	71.06		B										
8H-CC	71.38	71.43		B										
9H-CC	77.78	77.83		B										
10H-1, 100–101	78.80	78.81		B										
10H-CC	87.77	87.83		B										
11H-1, 36–37	87.66	87.67		B										
11H-3, 10–11	90.16	90.17		B										
11H-5, 61–62	93.67	93.68		B										
11H-CC	97.00	97.05		B										
12H-6, 105–106	105.48	105.49		B										
12H-6, 111–112	105.54	105.55		B										
12H-CC	106.80	106.85		B										
13H-CC	116.18	116.23		B										
14H-7, 25–26	125.11	125.12		B										
14H-CC	125.70	125.75		B										
15H-3, 84–85	128.87	128.88		B										
15H-CC	130.30	130.35		B										
16H-3, 80–81	133.81	133.82		B										
16H-CC	135.07	135.12		B										
17H-3, 113–114	138.83	138.80		B										
17H-CC	139.77	139.82		B										
18H-2, 102–103	141.92	141.93		B										
18H-CC	144.41	144.46		B										
19H-3, 107–108	148.17	148.18	P	R							R			
19H-CC	149.19	149.24	M	R							R			
20H-CC	153.82	153.87		B										
21H-CC	158.60	158.65		B										
22H-CC	163.16	163.21		B										
23H-CC	167.84	167.89		B										
24H-CC	172.59	172.64		B										
25H-CC	177.33	177.39		B										
26H-CC	181.97	182.03		B										
27H-CC	186.64	186.70		B										
28H-CC	191.51	191.57		B										
29H-CC	196.00	196.06		B										
30H-CC	200.90	200.95		B										

Table T5 (continued).

Core, section, interval (cm)	Top depth CSF-A (m)	Bottom depth CSF-A (m)	Preservation	Abundance	*Braarudosphaera bigelowii*	*Coccolithus pelagicus*	*Emiliania huxleyi*	*Gephyrocapsa caribbeanica*	*Gephyrocapsa muellerae*	*Gephyrocapsa oceanica* s.s.	*Gephyrocapsa* spp. small (<4 µm)	*Pontosphaera* spp.	*Reticulofenestra minutula*	Comments
31H-CC	205.50	205.55		B										
346-U1422D-														
1H-1, 115–116	1.15	1.16		B										
1H-4, 89–90	5.39	5.40		B										
1H-4, 61–62	5.11	5.12		B										
2H-2, 59–60	10.19	10.20		B										
2H-3, 129–130	12.39	12.40		B										
3H-6, 115–116	20.75	20.76	M	R	R		R				F			
3H-7, 26–27	21.36	21.37	G	A	R	F		R			D			*
4H-1, 98–99	22.58	22.59	P	R	R					R	F			
4H-5, 4–5	27.64	27.65	G	R	F	R								
4H-5, 89–90	28.49	28.50	M	F		R			R	R	R		R	

* = the presence of *Emiliania huxleyi* is not clear. Preservation: G = good, M = moderate, P = poor. Abundance: D = dominant, A = abundant, C = common, F = few, R = rare, B = barren. Shaded intervals = barren.

Table T6. Preservation and estimated abundance of radiolarians, Hole U1422C.

Core, section	Top depth CSF-A (m)	Bottom depth CSF-A (m)	Preservation	Abundance	*Actinomma antarcticum*	*Actinomma boreale*	*Actinomma leptodermum*	*Amphimelissa setosa*	*Axoprunum acquilonium*	*Carpocanarium papillosum*	*Ceratospyris borealis*	*Cornutella profunda*	*Cycladophora cornutoides*	*Cycladophora davisiana*	*Cycladophora sakaii*	*Cyrtopera languncula*	*Dictyocoryne truncatum*	*Hexacontium parviakitaensis*	*Larcopyle polyacantha* group	*Larcopyle pylomaticus*	*Octopyle/Tetrapyle* group	*Peripyramis circumtexta*	*Peripyramis woodringi*	*Phorticium pylonium* group	*Siphocampe arachnea* group	*Sphaeropyle antarctica*	*Sphaeropyle langii*	*Sphaeropyle robusta*	*Spongodiscus* sp.	*Spongopyle osculosa*	*Stichocorys peregrina*	*Stichocorys seriata*	*Stylatractus universus*	*Stylochlamydium venustum*	*Thecosphaera japonica*	*Thecosphaera pseudojaponica*
346-U1422C-																																			
1H-CC	4.59	4.64	M	F		R					P			A					R																
2H-CC	14.28	14.31	G	A		R		P			R			P					A						R										
3H-CC	23.99	24.04	G	A				R			R			P			R		C					R				A		R					
4H-CC	33.40	33.45	M	R			R												R									R							
5H-CC	42.47	42.51	G	A							A			A					C		R							C							
6H-CC	52.25	52.29		B																															
7H-CC	62.10	62.17		B																															
8H-CC	71.38	71.43	P	R							R																								
9H-CC	77.78	77.83		B																															
10H-CC	87.77	87.83	M	F					R														R												
11H-CC	97.00	97.05	G	C			R		C											C	R		C		R				R					C	
12H-CC	106.80	106.85	G	A					F			R		A						R			C		R										
13H-CC	116.18	116.23	G	F		R			R		R			R						R															
14H-CC	125.70	125.75	G	C		R					R	F		F	R					R					F										
15H-CC	130.30	130.35	G	C		F			R		C	F	C	C						C		R				F								C	R
16H-CC	135.07	135.12	G	A	A				R					F	R	R				F		R	C			C			C				F	C	
17H-CC	139.77	139.82	M	R					C	C	R	R		P	R							R												F	C
18H-CC	144.41	144.46	G	C	C									P	R					C														C	
19H-CC	149.19	149.24	G	A					R		C	R			R					F		R			R						R			F	R
20H-CC	153.82	153.87	G	C							C				F			R							F									F	
21H-CC	158.60	158.65	G	A								R			A			F	R	R					R									F	R
22H-CC	163.16	163.21	G	A					R				F		A			R							F				F						
23H-CC	167.84	167.89	G	A					C						A				F	C			P												
24H-CC	172.59	172.64	G	A								R	F		C			F	F	C		P			F					F					
25H-CC	177.33	177.39	G	A									F		A			R	F	F		P			F					F				F	
26H-CC	181.97	182.03	G	C					R				F		C			R	F	R					F										R
27H-CC	186.64	186.70	G	C					R						C	P		F		R					R					R			P	R	
28H-CC	191.51	191.57	G	C					R									F	F	F		P			R									F	R
29H-CC	196.00	196.06	G	C					R						F			F	C	C					F					F				R	
30H-CC	200.90	200.95	G	C								F			F			F		F										R				R	
31H-CC	205.50	205.55	G	C					R			F			C	P		C	F	C					C			F		R					

Preservation: G = good, M = moderate, P = poor. Abundance: A = abundant, C = common, F = few, R = rare, P = present, B = barren. Shaded intervals = barren.

Table T7. Preservation and estimated abundance of diatoms, Hole U1422C.

Core, section	Top depth CSF-A (m)	Bottom depth CSF-A (m)	Preservation	Abundance	*Actinocyclus curvatulus*	*Actinocyclus oculatus*	*Actinoptychus senarius*	*Aulacoseira* spp.	*Azpeitia endoi*	*Azpeitia nodulifera*	*Chaetoceros* spp. and similar spores	*Cocconeis scutellum*	*Coscinodiscus marginatus*	*Coscinodiscus radiatus*	*Denticulopsis dimorpha*	*Neodenticula kamtschatica*	*Neodenticula koizumii*	*Neodenticula seminae*	*Paralia sulcata*	*Proboscia curvirostris*	*Rhizosolenia styliformis*	*Shionodiscus oestrupii*	*Stephanopyxis turris*	*Stephanopyxis* spp.	*Thalassionema nitzschioides*	*Thalassiosira antiqua*	*Thalassiosira eccentrica*	*Thalassiosira gravida*	*Thalassiosira leptopus*	*Thalassiosira manifesta*	*Thalassiosira nidulus*	*Thalassiosira pacifica*
346-U1422C-																																
1H-CC	4.59	4.64	M	R				R												R												
2H-CC	14.28	14.31	M	R	F			C			R							R			F	F			F				C			
3H-CC	23.99	24.04	M	C							A							R					R		R	R						
4H-CC	33.40	33.45	M	R												R									R							
5H-CC	42.47	42.51	M	F		R				R	C			R						A		R	F		R			R				
6H-CC	52.25	52.29	M	R												R																
7H-CC	62.10	62.17		B																												
8H-CC	71.38	71.43		B																					R							
9H-CC	77.78	77.83	M	R			R						F	R											R							
10H-CC	87.77	87.83	M	R	F							R	R			R		R							R							
11H-CC	97.00	97.05	G	C				F			R			R				R	C				R		F	R						
12H-CC	106.80	106.85	G	A	R						R			R		F	A	A						F	R							
13H-CC	116.18	116.23	G	D							C			R		F	A	C				F	R	R	C							
14H-CC	125.70	125.75	G	A	R						F					F	A	C	R						R							
15H-CC	130.30	130.35	G	A							F					F	C	F			R			R	C							
16H-CC	135.07	135.12	G	C							F	F			F		A	C				R			R				R			
17H-CC	139.77	139.82	G	F		R		R			C	F			A		C	R			R	R	R		R					R		
18H-CC	144.41	144.46	G	F	R	R	R					F			R		C	R	R				F	F	R				F			
19H-CC	149.19	149.24	G	F			R	R	F		F				F	R	A								R						R	
20H-CC	153.82	153.87	G	D	R		R			R	F			R	F	A	C					C	R	F			F		F		R	
21H-CC	158.60	158.65	G	F							R			F		C	F		F			R	R	R	R							
22H-CC	163.16	163.21	G	C								R		R		C	A							R	R							R
23H-CC	167.84	167.89	G	D							R			R		A	C					R	R		R		R					F
24H-CC	172.59	172.64	G	D							R	R	F	F		C	C			R		R		F	F				R			
25H-CC	177.33	177.39	G	A							F		C			R	C					R			R							
26H-CC	181.97	182.03	G	R				R			R					F									R					R		
27H-CC	186.64	186.70	G	C			R			R	A	R				A			R		R				R							
28H-CC	191.51	191.57	G	A			R				C	R		R	R	A			C			F		C	R		R				R	
29H-CC	196.00	196.06	G	D				F			C		C			A					F	R		C	C		F					
30H-CC	200.90	200.95	G	D						R	F		C		R	A			R				R		C					R		
31H-CC	205.50	205.55	G	A	F		R				R			R		A			R			R	F		R							

Preservation: G = good, M = moderate. Abundance: D = dominant, A = abundant, C = common, F = few, R = rare, B = barren. Shaded intervals = barren.

Table T8. Presentation and estimated abundance of planktonic foraminifers, Site U1422. (Continued on next page.)

Core, section, interval (cm)	Top depth CSF-A (m)	Bottom depth CSF-A (m)	Preservation	Abundance	% Planktonic foraminifers	*Globigerina bulloides*	*Globigerina umbilicata*	*Globigerina quinqueloba*	*Globigerina* sp.	*Neogloboquadrina incompta*	*Neogloboquadrina* cf. *asanoi*	*Neogloboquadrina dutertrei*	*Neogloboquadrina kagaensis* and *Neogloboquadrina inglei*	*Neogloboquadrina pachyderma* (d)	*Neogloboquadrina pachyderma* (s)	*Neogloboquadrina* sp.	Total number of planktonic foraminifers	Planktonic foraminifers/10 cm^3	Comments
346-U1422A-																			
1H-CC	9.71	9.71	VG	R	100	2									2		4	1	
342-U1422B-																			
1H-CC	9.62	9.67		B													0	0	
346-U1422C-																			
1H-1, mudline	0.00	0.00		B													0	0	
1H-CC	4.59	4.64		B													0	0	
2H-CC	14.28	14.31	P	R	60	10									28		38	13	
3H-CC	23.99	24.04		R	100	3									2		5	17	
4H-1, 58–59	24.18	24.19	M	A	100	22		11						1	66		100	1000	
4H-5, 95–96	30.53	30.54	M	A	100	20	1					15			38		74	740	
4H-CC	33.40	33.45		B													0	0	
5H-4, 66–67	38.16	38.17	M	A	100	1		3	1	6		8	10	2	47	2	80	800	Reworking
5H-CC	42.47	42.51		R	99	10								1	29		40	13	
6H-3, 36–37	45.96	45.97	P	R	100	18	2	1		1	5	1		2	13	1	44	440	Reworking
6H-CC	52.25	52.29	P	B										1			1	0	
7H-5, 55–56	58.65	58.66	P	R	100	1			1								2	67	
7H-CC	62.10	62.17	P	R	100	3			1								4	1	
8H-7, 45–46	71.05	71.06		B													0	0	
8H-CC	71.38	71.43	P	R	50	5											5	2	
9H-CC	77.78	77.83		B													0	0	
10H-CC	87.77	87.83		B													0	0	
11H-CC	97.00	97.05		B													0	0	
12H-6, 105–106	105.48	105.49		B													0	0	
12H-CC	106.80	106.85		R													0	0	
13H-CC	116.18	116.23		B													0	0	
14H-CC	125.70	125.75		B													0	0	
15H-3, 84–85	128.87	128.88		B													0	0	
15H-CC	130.30	130.35		B													0	0	
16H-3, 84–85	133.81	133.82		B													0	0	
16H-CC	135.07	135.12		B													0	0	
17H-CC	139.77	139.82		B													0	0	
18H-2, 102–103	141.92	141.93		B													0	0	
18H-CC	144.41	144.46		B													0	0	
19H-CC	149.19	149.24		B													0	0	
20H-CC	153.82	153.87		B													0	0	
21H-CC	158.60	158.65		B													0	0	
22H-CC	163.16	163.21		B													0	0	
23H-CC	167.84	167.89		B													0	0	
24H-CC	172.59	172.64		B													0	0	
25H-CC	177.33	177.39		B													0	0	
26H-CC	181.97	182.03		B													0	0	
27H-CC	186.64	186.70		B													0	0	
28H-CC	191.51	191.57		B													0	0	
29H-CC	196.00	196.06		B													0	0	
30H-CC	200.90	200.95		B													0	0	
31H-CC	205.50	205.55		B													0	0	
15H-3, 84–85	128.87	128.88		B													0	0	
16H-3, 84–85	133.81	133.82		B													0	0	

Table T8 (continued).

Core, section, interval (cm)	Top depth CSF-A (m)	Bottom depth CSF-A (m)	Preservation	Abundance	% Planktonic foraminifers	*Globigerina bulloides*	*Globigerina umbilicata*	*Globigerina quinqueloba*	*Globigerina* sp.	*Neogloboquadrina incompta*	*Neogloboquadrina* cf. *asanoi*	*Neogloboquadrina dutertrei*	*Neogloboquadrina kagaensis* and *Neogloboquadrina inglei*	*Neogloboquadrina pachyderma* (d)	*Neogloboquadrina pachyderma* (s)	*Neogloboquadrina* sp.	Total number of planktonic foraminifers	Planktonic foraminifers/10 cm^3	Comments
346-U1422D-																			
1H-1, mudline	0.00	0.00		B													0	0	
3H-6, 115–116	20.76	20.76	P	R		70	23		6							1	100	1000	
15H-CC	132.73	133.75		B													0	0	
16H-CC	142.00	142.05		B													0	0	

Numbers of specimens in core catcher samples refer to ~30 cm^3, whereas numbers in core samples refer to 1 cm^3. Preservation: VG = very good, M = moderate, P = poor. Abundance: A = abundant, R = rare, B = barren. Shaded intervals = barren.

Table T9. Benthic foraminifers, Holes U1422A–U1422D.

Core, section, interval (cm)	Top depth CSF-A (m)	Bottom depth CSF-A (m)	Preservation	Agglutinated spp. (indet.)	*Eggerella bradyi*	*Martinottiella* sp.	*Miliammina echigoensis*	*Miliammina* sp.	*Cibicidoides robertsonianus*	*Cibicidoides* sp.	*Fursenkoina bradyi*	*Fursenkoina* sp.	*Globobulimina pacifica*	*Globobulimina pupoides*	*Globobulimina* sp.	*Melonis pompilioides*	*Pleurostomella* sp.	Total	Total foraminifers/10 cm^3	Agglutinated/10 cm^3	Calcareous benthics/10 cm^3
346-U1422A-																					
1H-CC	9.71	9.71																0	0	0	0
346-U1422B-																					
1H-CC	9.62	9.67																0	0	0	0
346-U1422C-																					
1H-1, mudline	0.00	0.00																0	0	0	0
1H-CC	4.59	4.64																0	0	0	0
2H-CC	14.28	14.31	P			28												28	9	9	0
3H-CC	23.99	24.04																0	0	0	0
4H-1, 58–59	24.18	24.19																0	0	0	0
4H-5, 95–96	30.53	30.54	VG								3							3	30	0	30
4H-CC	33.40	33.45																0	0	0	0
5H-4, 66–67	38.16	38.17																0	0	0	0
5H-CC	42.47	42.51	P			1												1	0	0	0
6H-3, 36–37	45.96	45.97																0	0	0	0
6H-CC	52.25	52.29																0	0	0	0
7H-5, 55–56	58.65	58.66																0	0	0	0
7H-CC	62.10	62.17	P														1	1	0	0	0
8H-7, 45–46	71.05	71.06	P								1							1	10	0	10
8H-CC	71.38	71.43	P									4	1	1				6	2	0	2
9H-CC	77.78	77.83																0	0	0	0
10H-CC	87.77	87.83																0	0	0	0
11H-CC	97.00	97.05	M						1	1								2	1	0	1
12H-6, 105–106	105.48	105.49																0	0	0	0
12H-CC	106.80	106.85	M												2			2	1	0	1
13H-CC	116.18	116.23	M	1				1										2	1	1	0
14H-CC	125.70	125.75	G		2	3												5	2	2	0
15H-3, 84–85	128.87	128.88																0	0	0	0
15H-CC	130.30	130.35	G				1	1										2	1	1	0
16H-3, 84–85	133.81	133.82																0	0	0	0
16H-CC	135.07	135.12	M		1		2											3	1	1	0
17H-3, 113–114	138.83	138.84																0	0	0	0
17H-CC	139.77	139.82	P										4	1				5	2	0	2
18H-2, 102–103	141.92	141.93																0	0	0	0
18H-CC	144.41	144.46	G				1											1	0	0	0
19H-CC	149.19	149.24																0	0	0	0
20H-CC	153.82	153.87	M										1					1	0	1	0
21H-CC	158.60	158.65																0	0	0	0
22H-CC	163.16	163.21	M				3											3	1	1	0
23H-CC	167.84	167.89	G						1				1					2	1	0	1
24H-CC	172.59	172.64	P				1											1	0	0	0
25H-CC	177.33	177.39																0	0	0	0
26H-CC	181.97	182.03																0	0	0	0
27H-CC	186.64	186.70																0	0	0	0
28H-CC	191.51	191.57	G				3											3	1	1	0
29H-CC	196.00	196.06	G				23									2		25	8	8	1
30H-CC	200.90	200.95																0	0	0	0
31H-CC	205.50	205.55																0	0	0	0
346-U1422D-																					
1H-1, mudline	0.00	0.00		8																	
3H-6, 115–116	20.75	20.76																0	0	0	0
15H-CC	132.73	133.75																0	0	0	0
16H-CC	142.00	142.05	G				6											6	2	1	1

Numbers of specimens in core catcher samples refer to ~30 cm^3, whereas numbers in core samples refer to 1 cm^3. Preservation: VG = very good, G = good, M = moderate, P = poor. Shaded intervals = barren.

Table T10. Calcium carbonate, total carbon (TC), total organic carbon (TOC), and total nitrogen (TN) contents on interstitial water squeeze cake sediment samples, Site U1422.

Core, section, interval (cm)	Top depth CSF-A (m)	Calcium carbonate (wt%)	TC (wt%)	TOC (wt%)	TN (wt%)
346-U1422C-					
1H-1, 145–150	1.45	0.9	1.22	1.10	0.28
1H-3, 135–140	4.35	0.2	1.76	1.73	0.35
2H-1, 145–150	6.05	0.3	0.35	0.30	0.25
2H-4, 145–150	10.55	0.3	2.47	2.44	0.37
3H-1, 145–150	15.55	0.2	0.72	0.69	0.26
3H-4, 145–150	20.05	1.9	0.94	0.71	0.24
4H-1, 145–150	25.05	0.4	0.45	0.40	0.28
4H-4, 145–150	29.53	2.2	2.98	2.72	0.36
5H-1, 145–150	34.55	0.2			
5H-4, 145–150	38.95	0.2	0.34	0.31	0.23
6H-1, 145–150	44.05	0.3	3.04	3.01	0.41
6H-4, 145–150	48.55	0.3	0.41	0.38	0.25
7H-1, 145–150	53.55	0.3			
7H-4, 145–150	58.05	0.2	0.38	0.36	0.25
8H-1, 145–150	63.05	0.3	0.94	0.91	0.25
8H-4, 145–150	67.55	0.2	0.34	0.31	0.24
9H-1, 145–150	72.55	0.1	0.29	0.27	0.29
9H-4, 115–120	76.79		0.35		0.25
10H-2, 145–150	80.75	0.2	0.55	0.54	0.25
10H-5, 145–150	85.31	0.2	0.69	0.67	0.26
11H-1, 121–126	88.51	0.2	0.63	0.61	0.28
11H-5, 145–150	94.51	0.1	0.40	0.39	0.25
12H-1, 145–150	98.25	0.2	0.42	0.40	0.00
12H-4, 145–150	102.85	0.2	1.33	1.31	0.24
13H-2, 145–150	109.25	0.2	0.62	0.60	
13H-5, 145–150	113.76	0.2	1.00	0.98	0.18
14H-1, 145–150	117.25	0.3	0.56	0.52	
14H-4, 145–150	121.75	0.2	0.67	0.65	0.19
15H-1, 145–150	126.75	0.1	0.62	0.60	0.27
16H-1, 145–150	131.45	0.2	0.86	0.84	0.30
17H-1, 145–150	136.15	0.3	0.87	0.84	0.30
18H-1, 144–149	140.84	0.2	0.71	0.69	0.27
19H-1, 145–150	145.55	0.2	0.37	0.35	0.25
20H-1, 145–150	150.25	0.2	0.49	0.46	0.23
21H-1, 145–150	154.95	0.2	0.95	0.93	0.27
22H-1, 145–150	159.65		0.84		0.22
23H-1, 145–150	164.35	20.7			
24H-1, 145–150	169.05		0.74		0.26
25H-1, 145–150	173.75	0.4	0.70	0.65	0.29
26H-1, 145–150	178.45		0.79		0.27
27H-1, 144–149	183.14	0.4	0.25	0.20	0.24
28H-1, 145–150	187.85		1.08		0.26
29H-1, 144–149	192.54	0.3	0.54	0.50	0.23
30H-1, 145–150	197.25		0.61		0.28
31H-1, 145–150	201.95	0.3	0.76	0.72	0.26

Blank cells = no data obtained.

Table T11. Interstitial water geochemistry, Site U1422. This table is available in an **oversized format.**

Table T12. Headspace (HS) gas concentrations, Site U1422.

Core, section, interval (cm)	Top depth CSF-A (m)	Sample type	Sediment volume (cm^3)	CH_4 (ppmv) measured	Ethane (ppmv) measured	CH_4 (ppmv) normalized	Ethane (ppmv) normalized	C_1/C_2
346-U1422C-								
1H-2, 0–5	1.50	HS	5.0	2.56	0.00	2.56	0.00	
2H-2, 0–5	6.10	HS	3.0	0.00	0.00	0.00	0.00	
2H-5, 0–5	10.60	HS	4.5	0.00	0.00	0.00	0.00	
3H-2, 0–5	15.60	HS	4.0	0.00	0.00	0.00	0.00	
3H-5, 0–5	20.10	HS	3.5	0.00	0.00	0.00	0.00	
4H-2, 0–5	25.10	HS	3.5	18.13	0.00	25.90	0.00	
4H-5, 0–5	29.58	HS	3.0	51.31	0.00	85.52	0.00	
5H-2, 0–5	34.60	HS	4.0	3,597.11	2.90	4,496.39	3.63	1,240.38
5H-5, 0–5	39.00	HS	4.0	8,359.44	5.94	10,449.30	7.43	1,407.31
6H-2, 0–5	44.10	HS	3.0	16,659.40	2.02	27,765.67	3.37	8,247.23
7H-2, 0–5	53.60	HS	3.2	16,560.17	1.73	25,875.27	2.70	9,572.35
7H-5, 0–5	58.10	HS	3.4	21,863.42	2.13	32,152.09	3.13	10,264.52
8H-2, 0–5	63.10	HS	3.2	23,808.44	3.07	37,200.69	4.80	7,755.19
8H-5, 0–5	67.60	HS	3.2	22,860.43	2.17	35,719.42	3.39	10,534.76
9H-2, 0–5	72.60	HS	3.4	24,206.85	2.41	35,598.31	3.54	10,044.34
9H-5, 0–5	76.84	HS	3.4	13,725.17	8.26	20,184.07	12.15	1,661.64
10H-3, 0–5	80.80	HS	3.4	20,217.20	2.12	29,731.18	3.12	9,536.42
10H-6, 0–5	85.39	HS	3.4	26,407.72	1.68	38,834.88	2.47	15,718.88
11H-2, 0–5	88.56	HS	3.5	7,277.57	4.16	10,396.53	5.94	1,749.42
11H-6, 0–5	94.56	HS	3.6	21,860.65	2.17	30,362.01	3.01	10,074.03
12H-2, 0–5	98.30	HS	3.4	15,729.57	9.22	23,131.72	13.56	1,706.03
12H-5, 0–5	102.90	HS	3.2	13,485.31	7.94	21,070.80	12.41	1,698.40
13H-3, 0–5	109.30	HS	3.2	22,499.11	2.16	35,154.86	3.38	10,416.25
13H-6, 0–5	113.81	HS	3.2	7,884.72	4.93	12,319.88	7.70	1,599.33
14H-2, 0–5	117.30	HS	4.0	32,208.68	2.03	40,260.85	2.54	15,866.34
14H-5, 0–5	121.82	HS	3.1	13,140.15	0.00	21,193.79	0.00	
15H-2, 0–5	126.80	HS	4.0	20,847.99	1.87	26,059.99	2.34	11,148.66
16H-2, 0–5	131.50	HS	3.0	10,620.82	6.08	17,701.37	10.13	1,746.85
17H-2, 0–5	136.20	HS	3.2	12,738.84	7.25	19,904.44	11.33	1,757.08
18H-2, 0–5	140.90	HS	4.0	28,137.87	1.72	35,172.34	2.15	16,359.23
19H-2, 0–5	145.60	HS	3.0	10,353.29	0.00	17,255.48	0.00	
20H-2, 0–5	150.30	HS	3.2	15,496.32	8.49	24,213.00	13.27	1,825.24
21H-2, 0–5	155.00	HS	3.0	15,753.39	9.11	26,255.65	15.18	1,729.24
22H-2, 0–5	159.70	HS	3.0	14,861.76	0.00	24,769.60	0.00	
23H-2, 0–5	164.40	HS	3.2	6,268.71	3.34	9,794.86	5.22	1,876.86
24H-2, 0–5	169.10	HS	2.6	8,832.01	5.53	16,984.63	10.63	1,597.11
25H-2, 0–5	173.80	HS	3.6	16,660.35	1.40	23,139.38	1.94	11,900.25
26H-2, 0–5	178.50	HS	2.8	12,284.53	7.05	21,936.66	12.59	1,742.49
27H-2, 0–5	183.19	HS	3.0	14,163.24	0.00	23,605.40	0.00	
28H-2, 0–5	187.90	HS	3.4	12,007.58	0.00	17,658.21	0.00	
29H-2, 0–5	192.59	HS	3.4	10,044.69	0.00	14,771.60	0.00	
30H-2, 0–5	197.30	HS	3.2	19,212.29	0.00	30,019.20	0.00	
31H-2, 0–5	202.00	HS	3.0	4,337.86	2.53	7,229.77	4.22	1,714.57
346-U1422E-								
3H-4, 0–5	23.50	HS	3.0	33.38	0.00	55.63	0.00	
3H-5, 0–5	25.00	HS	3.2	47.73	0.00	74.58	0.00	
3H-6, 0–5	26.50	HS	3.0	40.70	0.00	67.83	0.00	
3H-7, 0–5	28.00	HS	3.2	41.07	0.00	64.17	0.00	
4H-1, 145–150	29.95	HS	3.0	214.23	0.00	357.05	0.00	
4H-2, 145–151	31.45	HS	3.0	151.90	0.00	253.17	0.00	
4H-3, 145–152	32.95	HS	2.8	535.07	0.00	955.48	0.00	

Table T13. Vacutainer (VAC) gas concentrations, Site U1422.

Core, section	Top depth CSF-A (m)	Sample type	CH_4 (ppmv) GC3 measured	Ethane (ppmv) GC3 measured	C_1/C_2 GC3	Propane (ppmv) GC3 measured
346-U1422C-						
15H-2	127.68	VAC	855,675.06	56.84	15,054.10	
17H-4	139.05	VAC	905,772.58			
28H-2	189.07	VAC	931,566.86			
29H-3	195.06	VAC	931,392.90			0.46
30H-2	198.53	VAC	919,854.10			
31H-4	205.25	VAC	924,570.14			
346-U1422D-						
13H-1	104.14	VAC	890,317.21	64.48	13,807.65	

GC3 = gas analyzer (C_1–C_3).

Table T14. Absorbance at distinct wavelengths (yellowness) for interstitial water samples at Site U1422.

Core, section, interval (cm)	Top depth CSF-A (m)	Sample	Absorbance 325 nm				Absorbance 227 nm		
			B1	B2	B3	B4	B2	B3	B4
346-U1422A-									
1H-1, 145–150	1.45	IW-Sq	0.105		0.101			0.527	
1H-4, 145–150	5.95	IW-Sq	0.146						
346-U1422C-									
1H-1, 0	0	ML		–0.007			0.058		
1H-1, 145–150	1.45	IW-Sq	0.029	0.027			0.209		
1H-3, 135-140	4.35	IW-Sq	0.068						
2H-1, 145–150	6.05	IW-Sq							
2H-4, 145–150	10.55	IW-Sq	0.123						
3H-1, 145–150	15.55	IW-Sq	0.152	0.143			0.941		
3H-4, 145–150	20.05	IW-Sq	0.149						
4H-1, 145–150	25.05	IW-Sq	0.166	0.152	0.154		1.922	1.878	
4H-4, 145–150	29.53	IW-Sq	0.185						
5H-1, 145–150	34.55	IW-Sq			0.176	0.174		2.343	2.366
5H-4, 145–150	38.95	IW-Sq	0.202	0.175			2.105		
6H-1, 145–150	44.05	IW-Sq	0.171	0.173			1.383		
7H-1, 145–150	53.55	IW-Sq	0.176						
7H-4, 145–150	58.05	IW-Sq	0.177						
8H-1, 145–150	63.05	IW-Sq	0.172						
8H-4, 145–150	67.55	IW-Sq	0.150						
9H-1, 145–150	72.55	IW-Sq	0.135						
9H-4, 115–120	76.79	IW-Sq	0.137						
10H-2, 145–150	80.75	IW-Sq	0.138						
10H-5, 145–150	85.31	IW-Sq	0.140			0.143			1.293
11H-1, 121–126	88.51	IW-Sq	0.139						
11H-5, 145–150	94.51	IW-Sq	0.132						
12H-1, 145–150	98.25	IW-Sq	0.140						
12H-4, 145–150	102.85	IW-Sq	0.135						
13H-2, 145–150	109.25	IW-Sq	0.134						
13H-5, 145–150	113.76	IW-Sq	0.140						
14H-1, 145–150	117.25	IW-Sq	0.147	0.135		0.142	1.500		1.476
14H-4, 145–150	121.75	IW-Sq	0.126						
15H-1, 145–150	126.75	IW-Sq	0.121			0.118			1.409
16H-1, 145–150	131.45	IW-Sq	0.125			0.128			1.441
17H-1, 145–150	136.15	IW-Sq	0.120			0.123			1.433
18H-1, 144–149	140.84	IW-Sq	0.121			0.128			1.483
19H-1, 145–150	145.55	IW-Sq	0.125						
20H-1, 145–150	150.25	IW-Sq	0.115						
21H-1, 145–150	154.95	IW-Sq	0.112	0.120			1.457		
22H-1, 145–150	159.65	IW-Sq	0.112	0.113			1.533		
24H-1, 145–150	169.05	IW-Sq	0.117						
25H-1, 145–150	173.75	IW-Sq	0.116						
26H-1, 145–150	178.45	IW-Sq	0.111						
27H-1, 144–149	183.14	IW-Sq	0.114						
28H-1, 145–150	187.85	IW-Sq	0.111	0.124			1.610		
29H-1, 144–149	192.54	IW-Sq	0.103	0.100			1.663		
30H-1, 145–150	197.25	IW-Sq	0.114	0.120			1.638		
31H-1, 145–150	201.95	IW-Sq	0.101	0.102			1.618		
346-U1422E-									
3H-6, 10	26.60	IW-Rh		0.161			2.012		
3H-6, 30	26.80	IW-Rh		0.149			3.053		
3H-6, 60	27.10	IW-Rh		0.149			3.313		
3H-6, 90	27.40	IW-Rh		0.149			2.444		

IW-Sq = interstitial water from whole-round squeezing, ML = mudline, IW-Rh = interstitial water from Rhizons. Samples were examined in four batches over 23 days to evaluate precision in absorbance measurements in regards to time and dilution. Batch 1 (B1) comprised samples diluted 2:1 with deionized water on Day 1. Batch 2 (B2) comprised samples diluted 2:1 with deionized water on Day 2. Batch 3 (B3) comprised undiluted samples on Day 4. Batch 4 (B4) comprised undiluted samples on Day 23. Measured absorbance values for B1 and B2 have been multiplied by 3.

Table T15. FlexIT tool core orientation data, Hole U1422C.

Core	Orientation angle (°)	Orientation standard (°)
346-U1422C-		
2H	215.32	3.14
3H	128.55	1.98
4H	190.67	0.98
5H	89.11	1.65
6H	293.56	0.91
7H	345.80	1.17
8H	241.89	1.86
9H	281.21	1.91
10H	204.87	0.73
11H	140.34	0.51
12H	265.31	2.23
13H	312.74	1.71
14H	357.58	0.82

Table T16. Core disturbance intervals, Site U1422. (Continued on next three pages.)

Core, section interval (cm)	Comments on disturbance	Drilling disturbance intensity
346-U1422C-		
1H-1, 0–18	Soupy	Moderate to high
1H-2, 101–105	Void	
2H-3, 13.5–14.5	Void	
2H-6, 104–106	Void	
2H-CC, 0–26		Moderate
3H-CC, 0–5		Moderate
4H-3, 57.5–58	Void	
4H-3, 79–85	Deformed	
4H-CC, 0–34		Moderate to high
5H-1, 0–16		Moderate to high
5H-1, 107–109	Disturbance	
5H-4, 65–67	Along-core gravel/sand contamination	Slight
6H-1, 0–43		High
6H-2, 20–25	Disturbance	
6H-2, 48–50	Disturbance	
6H-3, 136–139	Disturbance	
6H-3, 145–150	Disturbance	
6H-CC, 0–13		Slight
7H-1, 0–30	Microfault	High
7H-2, 121–131	Disturbance	
7H-3, 15–24	Disturbance	
7H-4, 103–112	Molted	
7H-5, 100–117	Tilted	
7H-CC, 0–35		High
9H-CC, 0–24		Moderate to high
10H-3, 0–4		Moderate
10H-3, 56–73	Disturbance	
11H-2, 73–87		High
11H-3, 36–39		Moderate
11H-3, 139–142	Tilted	
12H-4, 32–35		Slight
12H-6, 0–150	Suck in	
13H-1, 0–15		Slight
13H-1, 142–150	Soupy	Slight
14H-1, 0–5	Disturbance	
14H-5, 124–124.5	Crack	Destroyed
14H-6, 85–87	Microfault	
15H-1, 0–26		Slight
15H-2, 0–3		Slight
15H-CC, 0–25		Severe
16H-1, 0–3		Slight
16H-CC, 0–26		Slight
17H-1, 0–15		Slight
17H-1, 122–125	Crack	Moderate to high
17H-CC, 10–13		Slight
18H-2, 38–38.5	Crack	Slight
18H-2, 107–109	Crack	Slight
18H-2, 147–148	Crack	Severe
18H-3, 44–48	Tilted	
18H-3, 54–59	Deformed	
18H-CC, 0–27		Slight
19H-1, 0–17		Moderate
19H-1, 97.5–98	Crack	Moderate
19H-2, 0–3		Moderate
19H-4, 25–25.3	Crack	Moderate to high
20H-1, 0–24		Moderate
20H-3, 26–26.5	Crack	Moderate
20H-3, 63–63.5	Crack	Moderate
20H-CC, 0–25		Moderate
21H-1, 0–15		High
21H-1, 3–4	Fall-in	Destroyed
22H-1, 0–5	Fall-in	Destroyed
22H-1, 0–21		Moderate
23H-1, 0–18		Moderate
23H-1, 16–17	Crack	High
23H-1, 89–95	Microfault	
23H-2, 128–131	Microfault	
23H-3, 46–49	Microfault	

Table T16 (continued). (Continued on next page.)

Core, section interval (cm)	Comments on disturbance	Drilling disturbance intensity
24H-1, 0–38		Moderate
24H-2, 0–4		Slight
25H-1, 0–3		Moderate
25H-4, 39–42	Crack	Moderate
26H-1, 10–15	Clasts near top, minor disturbance	Slight
26H-CC, 0–30		Moderate
27H-CC, 10–21		Moderate
28H-CC, 16–24		Moderate to high
29H-CC, 0–25	Void	Moderate
30H-CC, 18–22		Moderate
31H-4, 46–47	Crack	Slight
346-U1422D-		
1H-1, 0–150	Soupy	
1H-2, 118–120	Soupy	Moderate
1H-4, 0–35	Crack	Slight
1H-6, 44–45	Washed	
2H-2, 0–10	Disturbance	
2H-2, 16–18		Slight
2H-3, 25–29	Soupy	Moderate
2H-5, 79–84	Tilted	
2H-6, 24–29	Microfault	
2H-6, 38–42	Microfault	
2H-6, 115–119	Tilted	
2H-6, 141–143	Slump	
3H-1, 0–16	Mousselike	High
3H-1, 47–67	Microfault	
3H-1, 93–104	Microfault	
3H-1, 129–139	Microfault	
3H-3, 116–134	Slightly flow-in	
3H-5, 89–96	Deformed	
3H-7, 42–48	Microfault	
3H-CC, 14–27		Moderate
4H-1, 0–25		Slight to moderate
4H-4, 4–9	Disturbance	
4H-4, 47–56	Washed	Severe
4H-5, 0–2	Disturbance	
4H-5, 109–112.5	Deformed	
4H-6, 40–43	Tilted	
4H-7, 0–8		Moderate
4H-CC, 0–33		Moderate
5H-1, 1–16	Disturbance	
5H-1, 30–46	Microfault	
5H-3, 70–73	Washed	Destroyed
5H-3, 87–91	Microfault	
5H-4, 0–3		Slight
5H-6, 139–144	Deformed	
6H-1, 97–105	Washed	Moderate to high
6H-3, 104–113	Microfault	
6H-3, 139–144	Microfault	
6H-6, 89–97	Microfault	
6H-7, 70–95		Moderate to high
6H-CC, 0–25		Moderate
7H-6, 128–150	Suck in	Severe
7H-7, 0–111	Suck in	Severe
7H-8, 0–59	Suck in	Severe
7H-CC, 0–22	Suck in	Severe
8H-1, 39–44	Tilted	
8H-1, 141–145		Moderate
8H-6, 107–110	Nodule and tilted	
9H-2, 41–47	Microfault	
9H-4, 1–10	Ash patches distributed	
9H-4, 134–144	Tilted	
10H-1, 0–107	Slurry	Severe
10H-2, 66–80	Tilted	
10H-4, 0–10	Suck in	
10H-4, 79–115	Disturbance	
10H-CC, 0–20		Moderate
11H-1, 0–22		Moderate
11H-2, 0–3	Microfault	

Table T16 (continued). (Continued on next page.)

Core, section interval (cm)	Comments on disturbance	Drilling disturbance intensity
11H-2, 90–92	Microfault	
11H-3, 36–63	Disturbance	
11H-4, 128–130	Disturbance	
12H-1, 0–50	Disturbance	
12H-1, 107–113	Deformed	
12H-1, 136–144	Deformed	
12H-2, 123–130	Deformed	
12H-5, 100–110	Deformed	
13H	Suck in	Severe
14H-4, 105–122	Disturbance	
14H-CC, 0–18		Moderate to high
15H-7, 98–107		Slight
15H-CC, 0–20		Moderate
16H-1, 21–29	Microfault	
16H-1, 100–104	Microfault	
16H-4, 61–115	Nodule and deformed	
16H-5, 39–46	Microfault	
16H-6, 30–42	Deformed	
16H-CC, 0–26		Moderate
346-U1422E-		
1H-1, 0–150	Suck in	High
1H-2, 0–150	Suck in	High
1H-3, 0–150	Suck in	High
1H-4, 0–150	Suck in	High
1H-5, 0–150	Suck in	High
1H-6, 0–122	Suck in	High
1H-7, 0–68	Suck in	High
1H-CC, 0–23	Suck in	High
2H-1, 0–10	Disturbance	
2H-1, 61–64	Washed	
2H-1, 114–126	Microfault	
2H-1, 138–142	Microfault	
2H-2, 130–138	Microfault	
2H-CC, 0–12		Slight
3H-1, 17–28	Microfault	
3H-1, 33–35	Microfault	
3H-1, 41–45	Microfault	
3H-3, 121–124	Microfault	
3H-CC, 6–16	Suck in	Moderate
4H-1, 70–74	Microfault	
4H-2, 26–30	Washed	High
4H-6, 145–150	Microfault	
5H-1, 98–105	Washed	Destroyed
5H-1, 120–127		
5H-2, 5–9	Ash layer and tilted	
5H-2, 68–73	Washed	Destroyed
5H-3, 25–30	Deformed	
5H-3, 137–139	Deformed	
5H-4, 115–122	Deformed	
5H-5, 5–13	Microfault	
5H-CC, 0–22		Severe
6H-1, 0–4		Moderate
6H-3, 121–123	Disturbance	
6H-6, 30–150	Suck in	Destroyed
7H-1, 0–2		Slight
7H-2, 32–44	Soupy	Severe
7H-2, 91–98	Microfault	
7H-3, 145–150	Deformed	
8H-1, 0–60		Moderate
8H-2, 26–56	Deformed	
8H-2, 76–80	Deformed	
8H-4, 15–18	Microfault	
8H-5, 0–12	Deformed	
8H-6, 15–18	Microfault	
8H-5, 21–26	Nodule	
8H-5, 97–100	Deformed	
8H-5, 18–32	Thick ash	
9H-2, 0–20	Suck in	Destroyed
9H-2, 20–150		

Table T16 (continued).

Core, section interval (cm)	Comments on disturbance	Drilling disturbance intensity
9H-3, 0–102		
9H-4, 0–68		
10H-1, 0–30		Slight
10H-2, 69–80	Disturbance and tilted	
11H-1, 0–19		High
11H-1, 84–90	Ash layer and tilted	
11H-5, 11–21	Tilted	
11H-5, 57–61	Deformed	
11H-5, 123–128	Deformed	
11H-7, 0–8	Tilted	
12H	Suck in	Severe
13H		Severe
14H-1, 0–17	Disturbance	
14H-3, 0–140	Suck in	Destroyed
14H-4, 0–95	Suck in	Destroyed
14H-5, 0–86	Suck in	Destroyed

Table T17. NRM inclination, declination, and intensity data after 20 mT peak field AF demagnetization, Site U1422.

Core, section, interval (cm)	Depth CSF-A (m)	Inclination (°)	Declination (°)	FlexIT-corrected declination (°)	Intensity (A/m)
346-U1422A-					
1H-1	0				
1H-1, 5	0.05				
1H-1, 10	0.10				
1H-1, 15	0.15	70.3	330.6		0.009922
1H-1, 20	0.20	70.8	16.7		0.022891
1H-1, 25	0.25	73.2	36.4		0.032504
1H-1, 30	0.30	71.5	32.2		0.032932
1H-1, 35	0.35	76.6	31.7		0.024827
1H-1, 40	0.40	76	39		0.017713
1H-1, 45	0.45	73.3	35.3		0.014446
1H-1, 50	0.50	80.3	14.6		0.008651
1H-1, 55	0.55	72.3	13.3		0.009474
1H-1, 60	0.60	49.8	20.6		0.01628
1H-1, 65	0.65	56.2	21.8		0.010959
1H-1, 70	0.70	71.9	37.8		0.005725
1H-1, 75	0.75	79.3	166.7		0.002958
1H-1, 80	0.80	60.1	27.2		0.00492
1H-1, 85	0.85	49.1	25.5		0.009772
1H-1, 90	0.90	59.5	24.6		0.007036
1H-1, 95	0.95	62.4	18.3		0.004601
1H-1, 100	1.00	64.1	29.1		0.003264
1H-1, 105	1.05	58.7	355.2		0.003129
1H-1, 110	1.10	46.9	23.9		0.003723
1H-1, 115	1.15	52.4	17.2		0.002029
1H-1, 120	1.20	59.9	5.7		0.002778
1H-1, 125	1.25	55.2	39.1		0.002628
1H-1, 130	1.30	63.9	36.8		0.002121
1H-1, 135	1.35	54.8	28.4		0.003919
1H-1, 140	1.40				
1H-1, 145	1.45				
1H-1, 150	1.50				
1H-2	1.50				
1H-2, 5	1.55				
1H-2, 10	1.60				
1H-2, 15	1.65	64.7	12.7		0.013778
1H-2, 20	1.70	72	1.2		0.006336
1H-2, 25	1.75	65.6	321.5		0.003826
1H-2, 30	1.80	66.5	310.6		0.002805
1H-2, 35	1.85	58.4	252.7		0.00184
1H-2, 40	1.90	43.7	255.9		0.001821
1H-2, 45	1.95	49	358.3		0.004596
1H-2, 50	2.00	53.5	5.1		0.006392
1H-2, 55	2.05	65	336.7		0.003822
1H-2, 60	2.10	56.5	323.6		0.003097
1H-2, 65	2.15	55.9	316.2		0.002553
1H-2, 70	2.20	49.5	294.2		0.00202
1H-2, 75	2.25	54.6	321.7		0.002468
1H-2, 80	2.30	59.2	312.7		0.002175
1H-2, 85	2.35	51.2	298.8		0.001872
1H-2, 90	2.40	48.1	305.6		0.001965
1H-2, 95	2.45	51.3	320.2		0.00127
1H-2, 100	2.50	44	286.7		0.001545
1H-2, 105	2.55	44.5	291.5		0.001681
1H-2, 110	2.60	40.6	282.1		0.002257
1H-2, 115	2.65	51.8	279		0.002267
1H-2, 120	2.70	60.5	357.8		0.004633
1H-2, 125	2.75	58	3.1		0.007131
1H-2, 130	2.80	60.8	350.8		0.006277
1H-2, 135	2.85	46	286.9		0.002914
1H-2, 140	2.90				

Blank cells indicate depth levels where data were either not available (i.e., FlexIT-corrected declination data for nonoriented cores) or removed because of disturbance, voids, or measurement edge effects. Only a portion of this table appears here. The complete table is available in **ASCII.**

Table T18. Polarity boundaries, Site U1422.

Core, section, interval (cm)		Chron boundary	Age (Ma)	Depth CSF-A (m)				Depth CCSF-D (m)			
Top	Bottom			Top	Bottom	Midpoint	±	Top	Bottom	Midpoint	±
346-U1422C-	346-U1422C-										
4H-7, ~10	5H-1, ~120	(B) C1n (Brunhes/Matuyama)	0.781	32.67	34.33	**33.50**	0.83	35.50	37.16	**36.33**	0.83
5H-6, ~70	5H-7, ~10	(T) C1r.1n (Jaramillo)	0.988	41.20	41.80	41.50	0.30	44.03	44.63	44.33	0.30
6H-1, ~80	6H-3, ~147	(B) C1r.1n (Jaramillo)	1.072	43.40	47.00	45.20	1.80	43.40	47.00	45.20	1.80
9H-4, ~60	10H-1, ~95	(T) C2n (Olduvai)	1.778	76.23	78.77	**77.50**	1.27	76.23	78.77	**77.50**	1.27
10H-5, ~15	10H-5, ~135	(B) C2n (Olduvai)	1.945	84.00	85.20	84.60	0.60	84.00	85.20	84.60	0.60
346-U1422D-	346-U1422D-										
5H-1, ~5	5H-3, ~15	(B) C1n (Brunhes/Matuyama)	0.781	31.15	33.45	**32.30**	1.15	32.82	35.12	**33.97**	1.15
5H-7, ~70	6H-1, ~40	(T) C1r.1n (Jaramillo)	0.988	40.00	42.00	41.00	1.00	42.47	44.47	43.47	1.00
6H-3, ~110	6H-4, ~70	(B) C1r.1n (Jaramillo)	1.072	44.30	46.90	45.60	1.30	46.77	49.37	48.07	1.30
9H-6, ~130	10H-2, ~10	(T) C2n (Olduvai)	1.778	77.90	79.90	78.90	1.00	83.65	85.65	84.65	1.00
346-U1422E-	346-U1422E-										
4H-2, ~150	4H-4, ~50	(B) C1n (Brunhes/Matuyama)	0.781	31.50	33.50	**32.50**	1.00	33.29	35.29	**34.29**	1.00
5H-3, ~50	5H-3, ~110	(T) C1r.1n (Jaramillo)	0.988	41.50	42.10	**41.80**	0.30	44.29	44.89	**44.59**	0.30
5H-5, ~100	5H-6, ~90	(B) C1r.1n (Jaramillo)	1.072	45.00	46.40	45.70	0.70	47.79	49.19	48.49	0.70
9H-1, ~10	9H-1, ~150	(T) C2n (Olduvai)	1.778	76.10	77.50	**76.80**	0.70	83.65	85.65	84.65	0.70

B = bottom, T = top. Bold = boundaries that are relatively well defined.

Table T19. Results from APCT-3 temperature profiles, Site U1422.

Core	Minimum temperature at mudline (°C)	Average temperature at mudline (°C)	Depth CSF-A (m)	In situ temperature (°C)	Thermal resistance (m^2K/W)
346-U1422C-					
4H	0.22	0.34	33.1	4.80	37.57
7H	0.22	0.35	61.6	8.79	69.51
10H	0.23	0.37	87.3	12.07	97.99
13H	0.23	0.34	115.8	15.86	129.25
Average:	0.23	0.35			

In situ temperatures were determined using TP-Fit software by Martin Heesemann. Thermal resistance was calculated from thermal conductivity data (see **"Physical properties"**) corrected for in situ conditions (see **"Downhole measurements"** in the "Methods" chapter [Tada et al., 2015b]).

Table T20. Vertical offsets applied to cores in order to align a specific feature in adjacent cores, Site U1422.

Segment	Hole, core	Vertical offset (m)	Top depth CSF-A (m)	Bottom depth CSF-A (m)	Top depth CCSF-A (m)	Curated bottom depth CCSF-A (m)	Core	Vertical offset (m)	Top depth CSF-A (m)	Bottom depth CSF-A (m)	Top depth CCSF-A (m)	Curated bottom depth CCSF-A (m)	Core	Vertical offset (m)	Top depth CSF-A (m)	Bottom depth CSF-A (m)	Top depth CCSF-A (m)	Curated bottom depth CCSF-A (m)
	346-						346-U1422D-						346-U1422E-					
	U1422A-1H	6.92	0.0	9.5	6.92	16.88												
	U1422B-1H	1.73	0.0	9.5	1.73	11.40												
	346-U1422C-																	
	1H	–0.25	0.0	4.6	–0.25	4.39	**1H**	**0.00**	**0.0**	**8.1**	**0.00**	**8.14**	**1H**	**0.38**	**0.0**	**9.5**	**0.4**	**10.01**
	2H	0.44	4.6	14.1	5.04	14.75	**2H**	**–4.88**	**8.1**	**12.1**	**3.22**	**12.99**	**2H**	**0.44**	**9.5**	**19.0**	**9.9**	**19.57**
1	3H	1.01	14.1	23.6	15.11	25.05	**3H**	**–0.02**	**12.1**	**21.6**	**12.08**	**22.07**	**3H**	**1.41**	**19.0**	**28.5**	**20.4**	**30.21**
	4H	1.98	23.6	33.1	25.58	35.43	**4H**	**1.36**	**21.6**	**31.1**	**22.96**	**31.41**	**4H**	**1.79**	**28.5**	**38.0**	**30.3**	**40.17**
	5H	2.83	33.1	42.6	35.93	45.34	**5H**	**1.67**	**31.1**	**40.6**	**32.77**	**42.42**	**5H**	**2.79**	**38.0**	**47.5**	**40.8**	**50.59**
	6H	2.85	42.6	52.1	45.45	55.14	**6H**	**2.47**	**40.6**	**50.1**	**43.07**	**52.87**	**6H**	**3.94**	**47.5**	**57.0**	**51.4**	**60.67**
	7H	**4.39**	**52.1**	**61.6**	**56.49**	**66.56**	7H	3.49	50.1	59.6	53.59	63.33	**7H**	**4.61**	**57.0**	**66.5**	**61.6**	**71.43**
	8H	5.04	61.6	71.1	66.64	76.47	**8H**	**4.39**	**59.6**	**69.1**	**63.99**	**73.79**	**8H**	**5.70**	**66.5**	**76.0**	**72.2**	**82.15**
	9H	6.35	71.1	77.8	77.45	84.18	**9H**	**5.75**	**69.1**	**78.3**	**74.85**	**84.10**	9H	6.40	76.0	80.7	82.4	87.27
	10H	8.02	77.8	87.3	85.82	95.85	**10H**	**5.75**	**78.3**	**84.8**	**84.05**	**91.88**	**10H**	**7.63**	**80.7**	**85.4**	**88.3**	**93.14**
	11H	8.48	87.3	96.8	95.78	105.53	**11H**	**7.67**	**84.8**	**94.3**	**92.47**	**102.46**	**11H**	**8.72**	**85.4**	**94.9**	**94.1**	**103.83**
2	**12H**	**8.99**	**96.8**	**106.3**	**105.79**	**115.84**	**12H**	**8.38**	**94.3**	**103.8**	**102.68**	**112.54**	12H	8.78	94.9	104.4	103.7	113.60
													13H	9.76	104.4	106.0	114.2	115.78
	13H	**8.99**	**106.3**	**115.8**	**115.29**	**125.22**	13H	8.43	103.8	113.3	112.23	122.64	14H	11.73	106.0	111.6	117.7	123.40
	14H	**10.08**	**115.8**	**125.3**	**125.88**	**135.83**	**14H**	**9.05**	**113.3**	**122.8**	**122.35**	**132.31**						
3	15H	10.49	125.3	130.0	135.79	140.84	**15H**	**9.57**	**122.8**	**132.3**	**132.37**	**142.35**						
	16H	**10.68**	**130.0**	**134.7**	**140.68**	**145.80**	**16H**	**10.32**	**132.3**	**141.8**	**142.62**	**152.83**						
	17H	11.26	134.7	139.4	145.96	151.08												
	18H	**11.50**	**139.4**	**144.1**	**150.90**	**155.96**												
	19H	11.50	144.1	148.8	155.60	160.74												
	20H	11.50	148.8	153.5	160.30	165.37												
	21H	11.50	153.5	158.2	165.00	170.15												
	22H	11.50	158.2	162.9	169.70	174.71												
	23H	11.50	162.9	167.6	174.40	179.39												
	24H	11.50	167.6	172.3	179.10	184.14												
4	25H	11.50	172.3	177.0	183.80	188.89												
	26H	11.50	177.0	181.7	188.50	193.53												
	27H	11.50	181.7	186.4	193.20	198.20												
	28H	11.50	186.4	191.1	197.90	203.07												
	29H	11.50	191.1	195.8	202.60	207.56												
	30H	11.50	195.8	200.5	207.30	212.45												
	31H	11.50	200.5	205.2	212.00	217.05												

Bold = cores used for splice.

Table T21. Splice intervals, Site U1422.

Segment	Hole, core, section	Depth from top of section (cm)	Depth CSF-A (m)	Depth CCSF-D (m)	Hole, core, section	Depth from top of section (cm)	Depth CSF-A (m)	Depth CCSF-D (m)
	346-				346-			
1	U1422D-1H-1	0.00	0.00	0.00	U1422D-1H-5	107.64	7.08	7.08
	U1422E-1H-5	69.84	6.70	7.08	U1422E-1H-7	31.72	9.04	9.42
	U1422D-2H-5	19.88	14.30	9.42	U1422D-2H-6	54.02	16.14	11.26
	U1422E-2H-1	131.31	10.81	11.26	U1422E-2H-6	63.64	17.64	18.08
	U1422D-3H-5	0.18	18.10	18.08	U1422D-3H-7	4.36	21.14	21.12
	U1422E-3H-1	70.88	19.71	21.12	U1422E-3H-5	51.20	25.51	26.93
	U1422D-4H-3	96.97	25.57	26.93	U1422D-4H-6	26.72	29.07	30.42
	U1422E-4H-1	13.21	28.63	30.42	U1422E-4H-6	101.06	37.01	38.80
	U1422D-5H-5	84.59	37.14	38.80	U1422D-5H-7	71.03	40.00	41.67
	U1422E-5H-1	87.59	38.88	41.67	U1422E-5H-5	109.22	45.09	47.88
	U1422D-6H-4	71.11	45.41	47.88	U1422D-6H-7	56.08	49.76	52.23
	U1422E-6H-1	78.93	48.29	52.23	U1422E-6H-6	34.33	55.34	59.29
	U1422C-7H-2	129.15	54.89	59.29	U1422C-7H-4	98.72	57.59	61.98
	U1422E-7H-1	36.74	57.37	61.98	U1422E-7H-5	127.51	64.28	68.89
	U1422D-8H-4	39.64	64.50	68.89	U1422D-8H-6	117.29	68.27	72.67
	U1422E-8H-1	46.21	66.96	72.67	U1422E-8H-5	20.83	72.71	78.41
	U1422D-9H-3	56.24	72.66	78.41	U1422D-9H-6	148.50	78.09	83.83
2	U1422D-10H-1	0.01	78.30	84.05	U1422D-10H-5	101.85	85.32	91.07
	U1422E-10H-2	123.45	83.43	91.07	U1422E-10H-4	48.36	85.18	92.82
	U1422D-11H-1	34.89	85.15	92.82	U1422D-11H-5	143.71	92.26	99.93
	U1422E-11H-4	130.40	91.20	99.93	U1422E-11H-7	29.57	94.70	103.42
	U1422D-12H-1	73.62	95.04	103.42	U1422D-12H-6	148.14	103.28	111.66
	U1422C-12H-4	127.06	102.67	111.66	U1422C-12H-7	69.00	106.62	115.61
3	U1422C-13H-1	0.01	106.30	115.29	U1422C-13H-5	122.93	113.54	122.53
	U1422D-14H-1	18.04	113.48	122.53	U1422D-14H-7	49.94	122.91	131.96
	U1422C-14H-5	5.65	121.88	131.96	U1422C-14H-7	21.98	125.08	135.16
	U1422D-15H-2	136.47	125.59	135.16	U1422D-15H-7	76.04	132.14	141.71
	U1422C-16H-1	103.21	131.03	141.71	U1422C-16H-3	62.05	133.63	144.31
	U1422D-16H-2	27.70	133.99	144.31	U1422D-16H-7	116.89	142.12	152.44
	U1422C-18H-2	4.19	140.94	152.44	U1422C-18H-4	73.50	144.19	155.68

Table T22. Constrained tie points for depth-age relationship, Site U1422.

Selected ties for depth-age lines	Event type	Bioevents and epoch boundaries	Depth CCSF-A (m)	Depth range (±)	Age (Ma)	Age range (±)	Sedimentation rate (m/m.y.)
Top			*0.00*		*0.000*		
	R	LO *Amphimelissa setosa*	9.5	5.2	0.080	0.0	75.1
	R	LO *Spongodiscus* sp.	19.9	5.1	0.290	0.0	
Biostrat			*21.79*		*0.290*		
	CN	FO *Emiliania huxleyi*	23.7	2.5	0.290	0.0	32.0
	PM	Bottom of C1n (Brunhes/Matuyama)	34.9	1.5	0.781	0.0	
	D	LO *Proboscia curvirostris*	40.3	5.0	0.300	0.0	
Paleomag	PM	Top of C1r.1n (Jaramillo)	*44.1*	0.5	*0.988*	0.0	
	PM	Bottom of C1r.1n (Jaramillo)	48.2	0.3	1.072	0.0	47.9
Unit IA/IB			*63.97*		*1.402*		
	PM	Top of C2n (Olduvai)	85.1	3.1	1.778	0.0	53.6
	R	LO *Axoprunum acquilonium*	86.1	9.7	1.450	0.3	
Unit IB/II			*99.0*		*2.056*		
	PM	Bottom of C2n (Olduvai)	92.6	0.0	1.945	0.0	95.7
	D	LO *Neodenticula koizumii*	110.4	4.9	2.000	0.0	
	R	LO *Cycladophora sakaii*	130.5	5.3	2.300	0.0	
	D	FO *Neodenticula seminae*	148.4	2.6	2.400	0.0	
	R	FO *Cycladophora davisiana*	158.3	2.4	2.700	0.0	
Biostrat			*160.62*		*2.700*		
	D	LO *Neodenticula kamtschatica*	163.0	2.3	2.650	0.1	(95.7)
	R	LO *Hexacontium parviakitaensis*	163.0	2.3	2.700	0.0	
	D	FO *Neodenticula koizumii*	191.2	2.3	3.665	0.3	
	R	LO *Hexacontium parviakitaensis*	217.0	0.0	4.100	0.2	

R = radiolarian, CN = calcareous nannofossil, D = diatom, PM = paleomagnetism. LO = last occurrence, FO = first occurrence.